Dynamics Adjustment of Mesoscale Convective Lower-Stratospheric Outflows

by
Scott A. Hausman

Department of Atmospheric Science
Colorado State University
Fort Collins, Colorado

Research supported by the National Science Foundation under Grant ATM-9118966 and ATM-9115485. Salary and tuition were paid by the United States Air Force under the Air Force Institute of Technology Graduate Program.

Colorado State University

Department of Atmospheric Science

Paper No. 578

DYNAMIC ADJUSTMENT OF MESOSCALE CONVECTIVE LOWER–STRATOSPHERIC OUTFLOWS

by

Scott A. Hausman

Department of Atmospheric Science
Colorado State University
Fort Collins, CO 80523

Summer 1995

Atmospheric Science Paper No. 578

ABSTRACT

DYNAMIC ADJUSTMENT OF MESOSCALE CONVECTIVE LOWER-STRATOSPHERIC OUTFLOWS

Recent observational studies of upper–tropospheric and lower–stratospheric winds atop mesoscale convective systems show the development of anticyclonic outflow. We propose that the anticyclone formation can be partially explained by the gradient adjustment that follows the nearly instantaneous vertical redistribution of mass by the convection. With the convection idealized by an impulsive, diabatic mass transfer from the lower troposphere to a layer near the tropopause, the adjustment process is examined using an invertibility principle developed from the quasi–static primitive equations for axisymmetric, inviscid, adiabatic flow on an f–plane in potential radius and entropy coordinates. The invertibility principle is solved as a single, nonlinear, elliptic problem. Solutions show the development of an anticyclone aloft with cold and warm temperature anomalies above and below, respectively. Sensitivity studies indicate that the anticyclone strength is greatest for lower–stratospheric injections at high latitudes including the effects of cloud–top cooling. As the magnitude of the anticyclone increases, the inertial stability of the system is reduced, resulting in a decreased partitioning of the initial available potential energy to the balanced state of the system.

Scott A. Hausman
Department of Atmospheric Science
Colorado State University
Fort Collins, Colorado 80523
Summer 1995

ACKNOWLEDGEMENTS

Clearly a work of this magnitude is not accomplished by the author alone but with the helpful support of many friends and colleagues. In an expression of my appreciation, I would like to acknowledge those individuals that have made an outstanding contribution to this work.

Most importantly, I would like to thank my advisor, Dr. Wayne Schubert, for all of his encouragement and guidance over the past two years. Similarly, I thank the other members of my committee, Dr. William Cotton and Dr. David Krueger, for their expertise and invaluable comments. My thanks are also extended to Dr. Scott Fulton for developing the model used in this study; and to Paul Ciesielski, Rick Taft, and Gail Cordova for their expert support, accessibility, and friendship. This work could not have been completed in such a short time without their help.

Finally, I would like to thank my wife, Marianne, and daughters, Christina and Allison, for their sacrifice, patience, and moral support during these challenging two years.

This research was funded by the National Science Foundation under grants ATM–9118966 and ATM–9115485. Salary and tuition were paid by the United States Air Force under the Air Force Institute of Technology Graduate Program.

DEDICATION

To the glory of God.

CONTENTS

1 Introduction 1
1.1 Observational Evidence 1
1.2 Numerical Evidence 2
1.3 Overview 4

2 Review 5
2.1 Introduction 5
2.2 Examining the Wind Anomalies 5
2.3 Examining the Temperature Anomalies 10
2.4 Explaining the Anomalies 12
2.5 Understanding Gradient Adjustment 16
2.6 Revealing the Effects of Entrainment and Radiation 20
2.6.1 Cooling by Entrainment 20
2.6.2 Cooling by Radiation 22

3 Model 24
3.1 Introduction 24
3.2 Thinking in Terms of PV 25
3.2.1 PV Definition 25
3.2.2 Impermeability Theorems 27
3.2.3 Invertibility Requirements 28
3.3 Formulating the Problem of Moist Convection using PV Anomalies 30
3.3.1 Basic State and Governing Equations 30
3.3.2 Perturbation 33
3.4 Extracting the Balanced State from the PV Distribution 35
3.4.1 Gradient Balance Condition 35
3.4.2 Gradient Balance Condition with Potential Radius Coordinate 37
3.5 Analyzing the Balanced Fields 41
3.5.1 Energetics 41
3.5.2 Mass Removed 42
3.6 Applying the Appropriate Numerics 43

4 Results 45
4.1 Introduction 45
4.2 Developing the Control Simulation 45
4.2.1 Initial Conditions 45
4.2.2 Balanced State 48
4.2.3 Comparison to Observations 55
4.3 Comparing the Control to Sensitivity Simulations 57

4.3.1 Forcing Changes 57
4.3.2 Static Stability Changes 60
4.3.3 Latitude Changes 66
4.4 Considering the Effects of Entrainment and Radiation 71

5 Summary and Conclusions **75**
5.1 Summary 75
5.2 Conclusions 75
5.3 Future Research 77

References **79**

LIST OF FIGURES

2.1 200 mb observed wind field at 1200 UTC on (a) 7 May 1978 and (b) 27 June 1979. The shaded area represents the cirrus cloud tops with temperature $\leq -52°$C. A full wind barb is 5 ms^{-1} while a flag is 25 ms^{-1} (From Fritsch and Maddox, 1981a). 7
2.2 Same as Fig. 2.1 except for the 200 mb 12 hour LFM forecast wind field (From Fritsch and Maddox, 1981a). 8
2.3 Same as Fig. 2.1 except for the vector difference of the 200 mb observed and 12 hour LFM forecast wind fields (From Fritsch and Maddox, 1981a). . . . 9
2.4 Mesohigh perturbation isotachs (dashed, 5 ms^{-1} contour interval) and streamlines (solid) obtained using a 1500 km bandpass filter on the 1200 UTC 200 mb observed wind field from the 7 May 1978 case. The shaded area represents the cirrus cloud tops with temperature $\leq -52°$C (From Fritsch and Maddox, 1981a). 10
2.5 MCC (a) horizontal divergence, (b) vertical velocity (ω), and (c) vertical component of relative vorticity profiles for the MCC–12 h, initial, mature, and dissipation stages (From Cotton, et al., 1989). 11
2.6 Temperature analysis at (a) 150 and (b) 300 mb for 1200 UTC on 7 May 1978. Shading indicates (a) $-52°$C or colder cloud tops, and (b) temperatures warmer than $-34°$C (From Fritsch and Maddox, 1981a). 13
2.7 1200 UTC, 26 April 1991 soundings from Lake Charles, LA (LCH); Slidell, LA (SIL); and Jackson, MS (JAN) (From Bosart and Nielsen, 1993). 14
2.8 Contours of temperature (right) and velocity (left) from an analytic model of a homogeneous intrusion of fluid into a rotating, continuously stratified environment. The contour interval on both sides is 0.1 nondimensional units. The velocities scale as NH (From Gill, 1981). 18
2.9 Results from an axisymmetric, Lagrangian parcel model. Fields shown are the (a) initial element configuration with shaded area being the positively buoyant elements (2.1K increase in θ with each element), (b) final element configuration with lens and "eye" wall structure, (c) parcel displacement field, and (d) the balanced tangential velocity (1 ms^{-1} contour interval). Initially, elements in the same horizontal plane have the same potential temperature while elements in the same vertical column have the same angular momentum (From Shutts et al., 1988). 19
2.10 Theoretical mechanism for stratospheric anvil formation and its associated temperature distribution (From Danielsen, 1982). 21

3.1 (a) Atmosphere perturbed by a mass source "+" with (b) the resulting balanced state. (c) Atmosphere perturbed by a mass sink "-" with (d) the resulting balanced state. The arrows indicate the direction of gravity wave propagation while the circle with a dot in the center denotes flow out of the paper and the circle with an "x" in the center denotes flow into the paper. . 26
3.2 Generation of "+" and "-" PV anomalies by moist convection. Horizontal lines represent isentropic surfaces. 29
3.3 Basic state (a) temperature $\bar{T}(s)$ and (b) pseudodensity $\bar{\sigma}(s)$ profiles. δs_{TR} is the specific entropy difference over which the tropopause discontinuity is smoothed. 31
3.4 The (a) horizontal $F(r)$ and (b) vertical G(s) structure functions for a hypothetical MCS. 34

4.1 Control simulation initial (a) $\bar{\sigma}(s)$ and (b) $G(s)$ profiles. 48
4.2 Control simulation, hydrostatic pressure anomaly (10 mb contour interval). . . 49
4.3 Control simulation, basic state (dashed) and perturbation (solid) temperature profiles. 49
4.4 Control simulation initial σ^* field in (a) isobaric and (b) isentropic coordinates (70 kgKm^{-3} contour interval). Notice the change in the perturbation depth between (a) and (b). 50
4.5 Same as Fig. 4.4 except that the fields are for the adjusted state. It appears that the perturbation forces the tropopause downward along its base and produces an additional inversion along its top. Notice that the sloping "eye" wall structure on the outer edge of the surface σ^* anomaly is similar to that obtained by Shutts et al. (1988). 50
4.6 Control simulation adjusted state including the (a) tangential velocity v (1 ms^{-1} contour interval) and potential temperature θ fields (10 K contour interval), and the (b) basic state (dashed) and adjusted (solid) temperature profiles. . 51
4.7 Control simulation (a) buoyancy frequency N (0.005 s^{-1} contour interval) following the adjustment including the (b) inner (solid) and outer (dashed) boundary profiles. Notice the sharp peaks in N above and below the perturbation. 52
4.8 Control simulation isentropic relative vorticity ζ following the adjustment (5.0×10^{-6} s^{-1} contour interval). 52
4.9 Control simulation aspect ratio λ'/H' (contour interval is 50). 53
4.10 Control simulation potential radius R following the adjustment (100 km contour interval). Contours represent surfaces of constant angular momentum. Notice that the upper displacements are much greater than those at the surface. 53
4.11 Relationship between the perturbation amplitude $\hat{\sigma}$ and the percentage of mass removed from a cylinder of radius $2r_2$, bounded by the surface and s_1. The blackened data points indicate the values used in the control simulation. . . 58
4.12 Variation of the (a) velocity extremes and the (b) radial displacements needed to produce the velocity extremes in relation to the forcing. The blackened data points are the same as in Fig. 4.11. 59
4.13 Relationship between the energetics and the forcing including the (a) integrated APE$_0$, APE, and KE; and the (b) percentage of APE$_0$ partitioned to the balanced APE and KE. The blackened data points are the same as in Fig. 4.11. 59

4.14 Variation of the (a) velocity extremes and the (b) percentage of APE$_0$ partitioned to the balanced APE and KE as a function of the perturbation radius r_2. The blackened data points are the same as in Fig. 4.11. 60
4.15 Same as Fig. 4.6 except that the 50 mb perturbation is located immediately beneath the tropopause. 62
4.16 Same as Fig. 4.7 except that the 50 mb perturbation is located immediately beneath the tropopause. 63
4.17 Same as Fig. 4.8 except that the 50 mb perturbation is located immediately beneath the tropopause. 63
4.18 Same as Fig. 4.9 except that the 50 mb perturbation is located immediately beneath the tropopause. 64
4.19 Same as Fig. 4.10 except that the 50 mb perturbation is located immediately beneath the tropopause. 64
4.20 Variation of the (a) minimum velocity and the (b) percentage of APE$_0$ partitioned to the balanced APE and KE as a function of the perturbation's vertical placement. The blackened data points are the same as in Fig. 4.11. 65
4.21 Variation of the (a) minimum velocity and the (b) percentage of APE$_0$ partitioned to the balanced APE and KE as a function of the average stratospheric static stability N. The blackened data points are the same as in Fig. 4.11. 65
4.22 Same as Fig. 4.6 except that the perturbation has been moved south to 10°N. . 67
4.23 Same as Fig. 4.7 except that the perturbation has been moved south to 10°N. . 68
4.24 Same as Fig. 4.8 except that the perturbation has been moved south to 10°N. . 68
4.25 Same as Fig. 4.9 except that the perturbation has been moved south to 10°N (contour interval is 500). 69
4.26 Same as Fig. 4.10 except that the perturbation has been moved south to 10°N. 69
4.27 Variation of the (a) velocity extremes and the (b) percentage of APE$_0$ partitioned to the balanced APE and KE as a function of the latitude. The curves do not extend to the equator due to the limitations of the f-plane approximation. Note that APE$_0$ is not a function of latitude, but has a constant value 1.23×10^{17}J. The blackened data points are the same as in Fig. 4.11. 70
4.28 Profile of $G(s)$ including an additional mass sink along the top of the outflow. . 71
4.29 Same as Fig. 4.6 except that a mass sink immediately above the injection has been introduced to simulate the effects of entrainment and radiational cooling. 72
4.30 Variation of the cold pool temperature as the magnitude of the cloud-top mass sink ϵ is increased. The blackened data point are the same as in Fig. 4.11. . 73

LIST OF TABLES

4.1 Control settings of the (a) basic state and (b) perturbation parameters. The values of entropy $s = c_p \ln(\theta/\theta_0)$, have been nondimensionalized by $s_T = c_p \ln(\theta_T/\theta_0)$. To further clarify the meaning of these values, equivalent pressure level have been included. 46

Chapter 1

INTRODUCTION

Upon witnessing the immensity of a mesoscale convective system (MCS) and observing the vastness of its cirrus anvil, we immediately wonder what influence such intense disturbances have on the flow aloft. Ultimately, we must question what errors the disturbances introduce into our model forecasts, since most large–scale numerical weather prediction (NWP) models do not resolve mesoscale convective fluxes of mass and momentum. Emphasizing this point, Maddox (1980a) explains that mesoscale convective complexes (MCC) in particular are "not explicitly predicted by operational numerical models even though they are shown to be organized in a distinctly nonrandom mode on scales that cannot be considered subgrid." This statement certainly applies not only to MCCs, but to squall lines and other forms of MCS as well. Lilly (1975) illustrates the point, stating that mesoscale convection has "a degree of organization which is clearly nonrandom but also largely unresolvable from conventional data processed in conventional operational ways. After its organization the convective storm array develops very high–energy density and one may suspect that . . . the large–scale environment loses control and the *tail wags the dog* (emphasis added)." No longer does the synoptic–scale environment independently modulate the convection but is itself modified. The degree of modification has been determined through detailed analysis of satellite imagery and atmospheric soundings.

1.1 Observational Evidence

Close examination of satellite loops and upper–air data indicates that mass injected into the upper–troposphere and lower–stratosphere by convection causes systematic variations in the flow. By computing the displacement of cirrus cloud elements atop a tornado–producing thunderstorm, Ninomiya (1971a, b) showed that the upper–tropospheric flow evolves into a difluent jet with maximum winds on the poleward side of the convection. Maddox et al. (1981) and Wetzel et al. (1983) verified that the jet streak is produced by the MCS and not by baroclinicity in the synoptic–scale flow. Using streamline analysis, Fankhauser (1974), Johnson et al. (1990), and Biggerstaff and Houze (1991) found that the outflow of mature squall lines is also strongly difluent. Even more impressive is the intense divergence observed in the outflow of mature MCCs (Fritsch and Maddox, 1981a, hereafter FM; Maddox et al., 1981; Wetzel et al., 1983; Cotton et al., 1989; and Tripoli and Cotton, 1989a, b). FM suggest that the observed divergence "strongly resembles the circulation which would result if a long–lived, meso–α scale, high–pressure perturbation were superimposed upon a mean westerly flow." In fact, earlier studies had revealed a positive geopotential anomaly atop the convection (Fankhauser, 1974). Further objective analysis conducted by FM show that a large anticyclonic lens develops in the upper–tropospheric flow.

Examining the upper air temperature data, FM discovered that the anticyclone is baroclinically driven by a pool of warm air beneath the anticyclone and a stronger cold pool above. The temperature perturbations were collocated with a layer of moisture above 600 mb indicating the presence of deep penetrative convection. Similar thermal features to those identified by FM were also observed by Bosart and Nielsen (1993, hereafter BN) in their analysis of soundings from a Gulf Coast convective cluster. They found that the lapse rate within the outflow layer is nearly adiabatic and that the wet bulb potential temperature is identical to that at the surface. Furthermore, reduced wind speeds in this layer indicate the presence of low momentum air advected from lower levels. BN suggest that the sounding penetrated undilute air from an updraft that had ascended from the planetary boundary layer.

1.2 Numerical Evidence

Numerical simulations of mesoscale convection consistently produce the kinematic and thermodynamic features discussed above (Fritsch and Maddox, 1981b; Fritsch and Brown, 1982; Tripoli and Cotton, 1989a, b; Zhang and Gao, 1989; Schubert et al., 1989;

Chen, 1990; Hertenstein and Schubert, 1991; Zhang, 1992; Davis and Weisman, 1994; Olsson, 1994; Jiang and Raymond, 1995). Results from these simulations indicate that the positive pressure anomaly is generated hydrostatically by a pool of cold air which forms atop the convection (Fritsch and Maddox, 1981b). Four possible sources of this cold air have been identified: 1) adiabatic cooling of the overshooting updraft, 2) adiabatic cooling of ascending air produced by mesoscale heating, 3) the downward heat flux produced by cloud–top entrainment, and 4) cloud–top radiative cooling. The resulting imbalance produced by the pressure anomaly leads to geostrophic adjustment and the development of the observed mesoscale anticyclone. Since the duration and scope of the adjustment are large in relation to the inertial time scale and the Rossby radius of deformation, respectively, Cotton et al. (1989, hereafter CLMT) has shown that MCSs represent inertially stable systems that are in approximate geostrophic balance. This realization has led to the development of balanced models to both forecast the balanced flow (Schubert et al, 1989; Raymond and Jiang, 1990; Hertenstein and Schubert, 1991; Jiang and Raymond, 1995) and to diagnose the balanced flow from primitive equation simulations (Davis and Weisman, 1994; Olsson, 1994).

Many numerical studies of MCCs (Fritsch and Chappell, 1980; Fritsch and Maddox, 1981b; and Fritsch and Brown, 1982; Zang and Fritsch, 1986) and squall lines (Schubert et al., 1989; Hertenstein and Schubert, 1991) have been developed using prescribed heating profiles to simulate the mesoscale convection; however, heating is not the only method available to parameterize diabatic effects. Convective motions generated by the heating lead to the diabatic transport of mass. As a result, diabatic effects may also be parameterized using the transfer of mass across isentropic surfaces. One of the first to use this method was Raymond (1983) in his study of wave–CISK. Shutts has also used it extensively in the study of deep penetrative convection (Shutts, 1987; Shutts et al., 1988; Shutts, 1994; Shutts and Gray, 1994).

1.3 Overview

The objective of this study is to show, using a balanced model, that the observed anticyclone and accompanying temperature perturbations can be partially explained by the almost instantaneous injection of undilute lower–tropospheric air into the outflow of mesoscale convection followed by gradient adjustment. In addition, the moderating effects of cloud–top cooling will be considered. The model is developed using the axisymmetric, quasi–static primitive equations for inviscid, adiabatic flow on an f–plane. Previous efforts to study the adjustment problem analytically have concentrated primarily on the linearized Boussinesq (Gill et al., 1979; Shutts, 1987; McDonald, 1990; McDonald, 1992) or anelastic systems (Shutts, 1994; Shutts and Gray, 1994). This work is more general in that the fluid is continuously stratified, and nonlinear effects are maintained through the application of gradient balance and the inclusion of advection. In order to obtain an invertibility principle similar to the classic Rossby (1938) adjustment problem, isentropic and potential radius coordinates (Schubert and Hack, 1983) are used to eliminate the advective processes, making them implicit in the coordinate transformation. Before discussing the model in more detail (Chapter 3), we will review the literature relevant to the development and interpretation of the model and its results (Chapter 2). A control simulation is then developed and compared to the observations of FM and BN followed by a series of sensitivity studies designed to examine the variability of the mesohigh to changes in the forcing, static stability, latitude, and cloud–top cooling (Chapter 4). In the conclusion, we will consider the systematic impact that these mesoscale anticyclonic perturbations have on our large–scale NWP model forecasts and speculate on future research needs (Chapter 5).

Chapter 2

REVIEW

2.1 Introduction

In the introduction, the impact of sustained deep penetrative convection within MCSs on the kinematic and thermodynamic structure of the upper–troposphere and lower–stratosphere was discussed. Specifically, an anticyclonic circulation forms with cold and warm temperature anomalies above and below, respectively. Several mechanisms have been suggested as the cause of this structure. This chapter will provide additional detail to the observational and numerical studies discussed in Chapter 1 (Sections 2.2 and 2.3) followed by a summary of the suggested formation mechanisms (Section 2.4). In addition, material relevant to the gradient adjustment problem (Section 2.5), and the modifying effects of entrainment and radiation (Section 2.6) will also be reviewed.

2.2 Examining the Wind Anomalies

FM hoped to extract the anticyclonic circulation from the observed wind field by subtracting a numerically forecasted flow excluding the effects of deep convection. Since the LFM's[1] convective parameterization is an adjustment scheme (not including the vertical fluxes of mass, moisture, and momentum by the convection), the influence of mesoscale convection on the forecast wind fields should be absent. Thus, by taking the vector difference of the 200 mb observed and 12 hour LFM forecast winds for the same time should yield the anomalous upper tropospheric flow caused by the convection. Notice that this method also provides a measure of model error caused by the weaknesses in the convective parameterization scheme. FM applied this technique to two large MCCs that formed over the Midwest United States on 7 May 1978 (Figs. 2.1a–2.3a) and 27 June 1979 (Figs. 2.1b–2.3b).

---

[1] The Limited-area Fine-mesh Model(LFM) is a finite difference, primitive equation model developed by the National Meteorological Center (NMC). It is no longer used by NMC to produce national forecasts.

FM's objective analysis reveals a region of strongly divergent, anticyclonic outflow with an average magnitude of approximately 15–20 ms^{-1} (Fig. 2.3a and b). Similar anticyclonic circulations of 5–10 ms^{-1} have been observed in the outflow of tropical cloud clusters (Leary, 1979). In both cases considered by FM, the jet was intensified on the poleward side of the convection and weakened to the south with the strongest wind anomalies located downwind of the convection. Taking the vector difference of mesoscale model simulations including and excluding the effects of convection, Maddox et al. (1981) demonstrated that the jet streak is produced by the mesoscale convection and not by the large–scale baroclinicity of the polar jet. According to Wetzel et al. (1983), the shallow depth of the jet streak also distinguishes it from the much deeper polar jet. FM further analyzed the 7 May 1978 case using a scale separation technique developed by Maddox (1980b).

In this method, a low-pass filter first smoothes the data fields followed by a 1500 km bandpass filter which removes the mesoscale modes. The recovered fields represent the mesoscale and macroscale components of the flow. Fig. 2.4 beautifully illustrates the anticyclonic outflow with maximum speeds of 20 ms^{-1} to the northwest and northeast of the convection. Later observational studies have continued to increase our understanding of these features.

Maddox (1983) and CLMT used a composite analysis technique to construct profiles of mean divergence, vertical velocity ω, and relative vorticity for various stages in the evolution of MCCs. The profiles obtained by CLMT are shown in Fig. 2.5. During the life cycle of the storm, the level of maximum vertical velocity climbs from 650 to 350 mb and the magnitude increases by about 25%. The increased ascent of mass impinging on the tropopause intensifies divergence (and ultimately the anticyclonic vorticity) by approximately 2/3. Notice the strong surface convergence and surface cyclonic flow. Most of the initial convergence occurs in a layer below 700 mb with a maximum at the surface

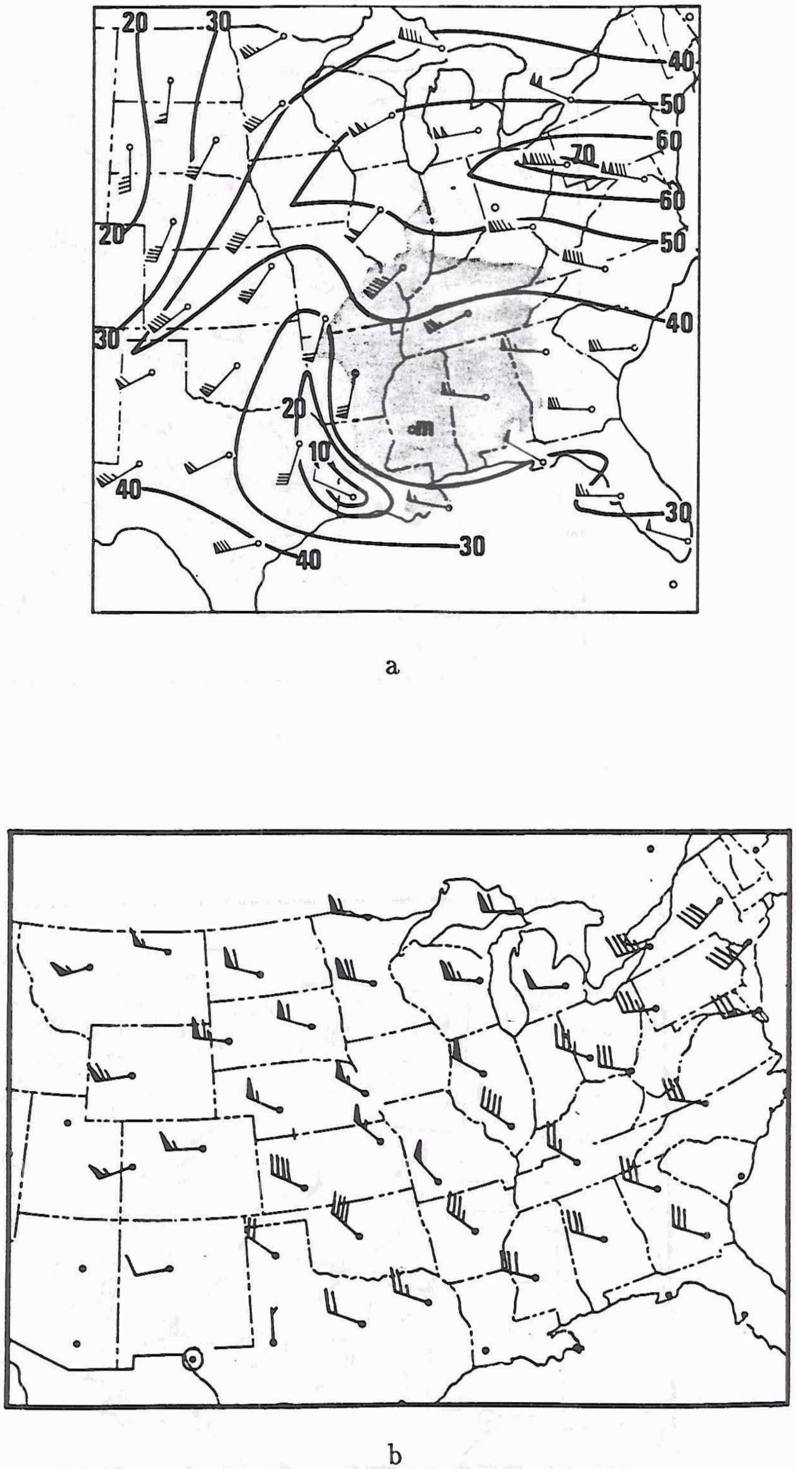
20
30
40
50
60
70
60
50
40
20
30
20
10
40
30
40
30
a
b

Figure 2.1: 200 mb observed wind field at 1200 UTC on (a) 7 May 1978 and (b) 27 June 1979. The shaded area represents the cirrus cloud tops with temperature $\leq -52°C$. A full wind barb is 5 ms^{-1} while a flag is 25 ms^{-1} (From Fritsch and Maddox, 1981a).

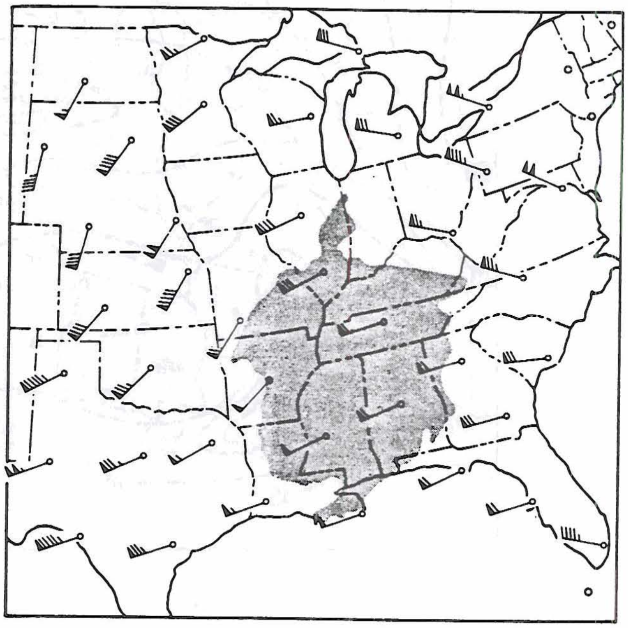

a

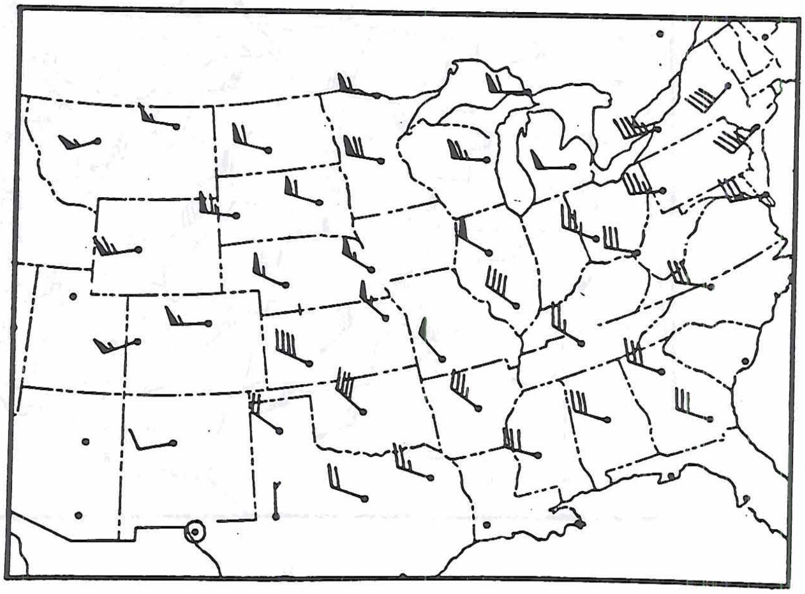

b

Figure 2.2: Same as Fig. 2.1 except for the 200 mb 12 hour LFM forecast wind field (From Fritsch and Maddox, 1981a).

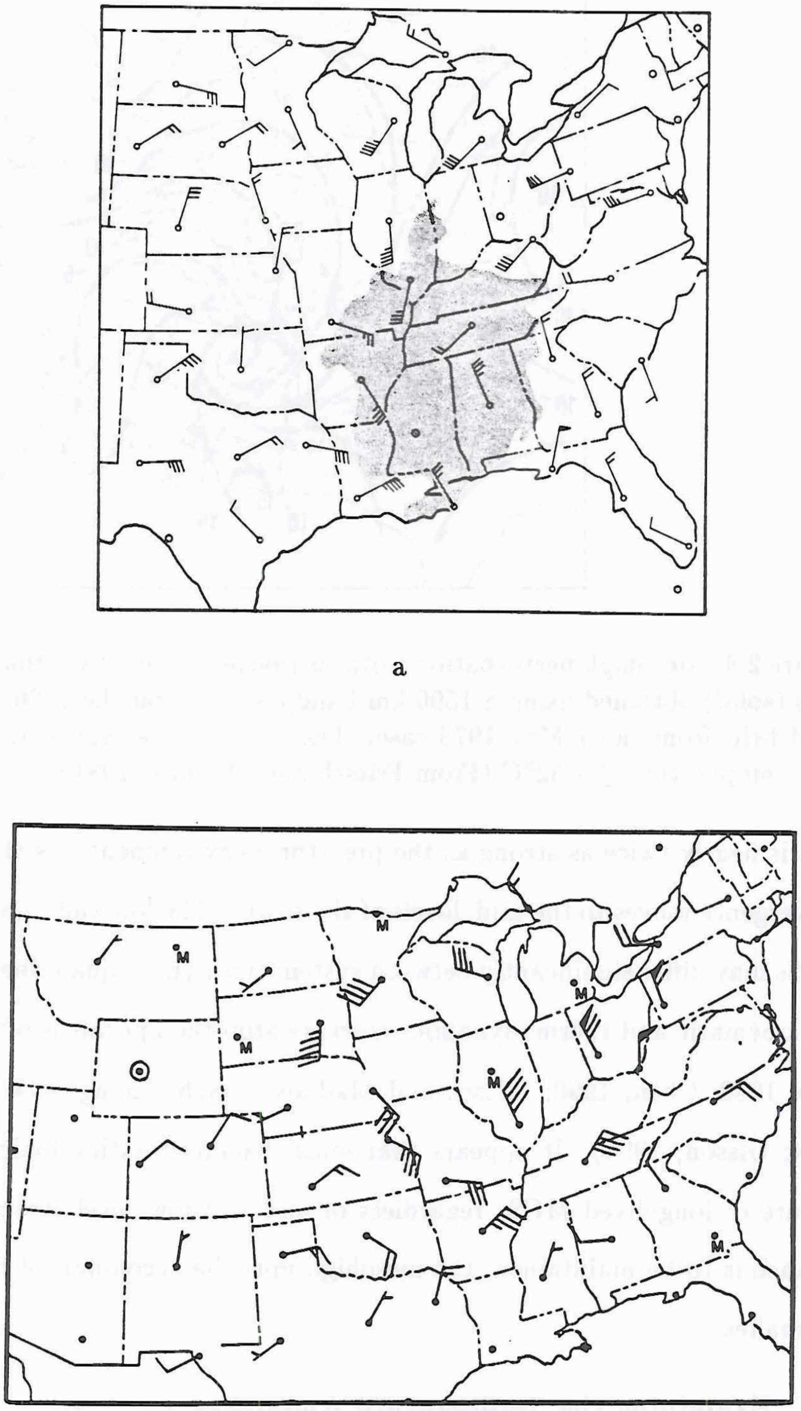

a

b

Figure 2.3: Same as Fig. 2.1 except for the vector difference of the 200 mb observed and 12 hour LFM forecast wind fields (From Fritsch and Maddox, 1981a).

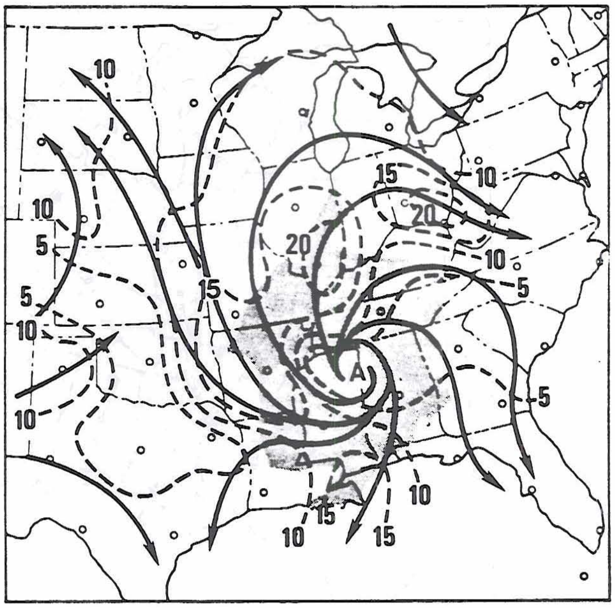

Figure 2.4: Mesohigh perturbation isotachs (dashed, 5 ms^{-1} contour interval) and streamlines (solid) obtained using a 1500 km bandpass filter on the 1200 UTC 200 mb observed wind field from the 7 May 1978 case. The shaded area represents the cirrus cloud tops with temperature ≤ −52°C (From Fritsch and Maddox, 1981a).

that is nearly twice as strong as the pre–storm environment. As the system matures, the convergence moves to the mid–levels of the storm. The low and mid–level structure within MCSs may differ significantly between system types (i.e., squall lines vs. MCCs); however, the kinematic and thermodynamic structure atop the updraft is often similar (Zhang and Gao, 1989; Chen, 1990; Fritsch and Maddox, 1981b; Zhang, 1992; Davis and Weisman, 1994; Olsson, 1994). It appears that quasi–balanced anticyclonic outflow is a common feature of long–lived MCSs regardless of mid and low–level structure. If thermal wind balance is to be maintained, the mesohigh must be accompanied by unique temperature anomalies.

2.3 Examining the Temperature Anomalies

Examining the upper air data for the 7 May 1978 MCC, FM detected anomalously warm and cold pools of air in the upper troposphere. Fig. 2.6 shows the 150 and 300 mb temperature analysis. A 6–8°C intense cold pool is present at 150 mb with a weaker 1–2°C

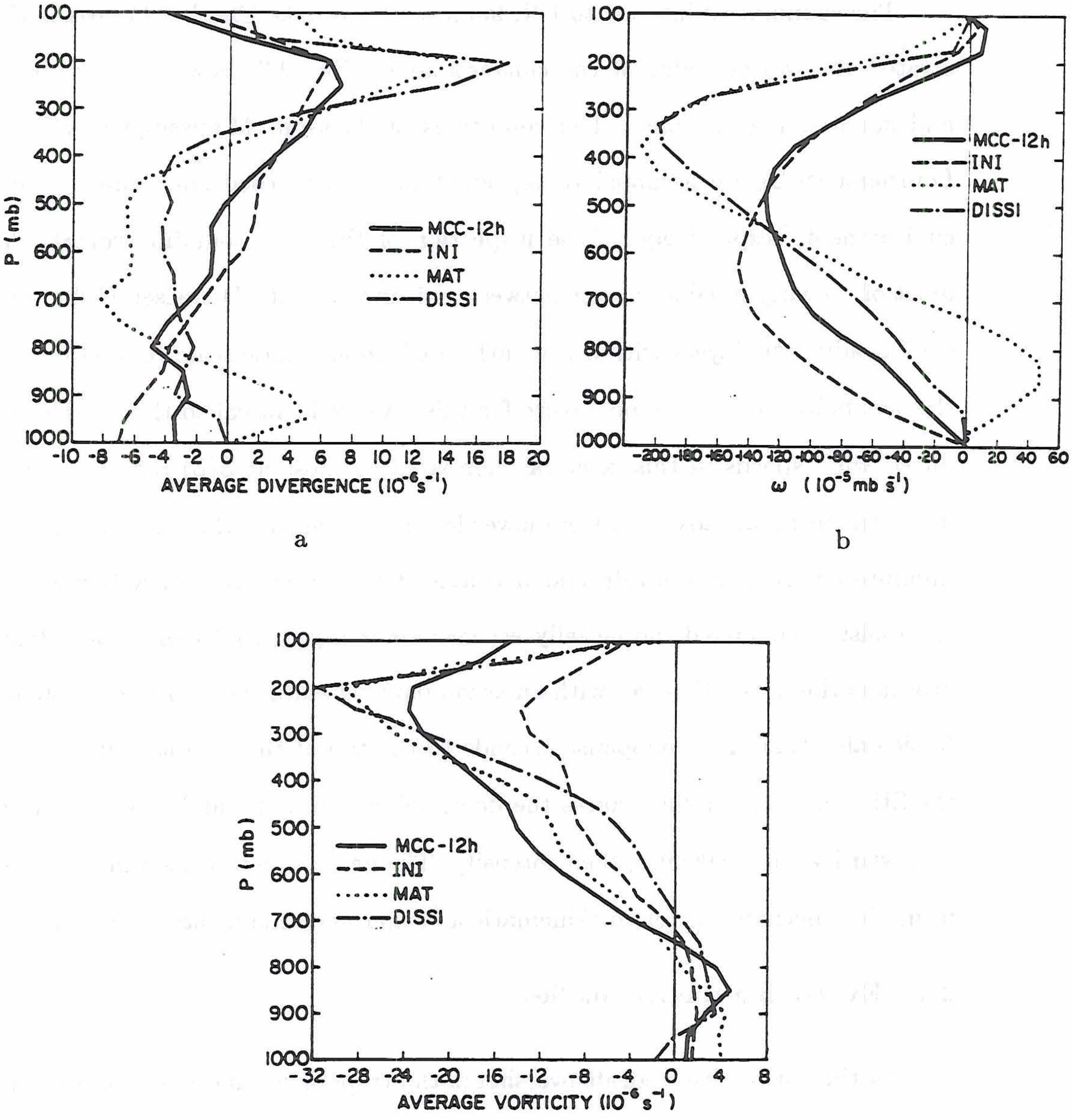

a

b

c

Figure 2.5: MCC (a) horizontal divergence, (b) vertical velocity (ω), and (c) vertical component of relative vorticity profiles for the MCC–12 h, initial, mature, and dissipation stages (From Cotton, et al., 1989).

warm pool below at 300 mb. In addition, FM point out that the soundings show a layer of moisture beginning at about 600 mb indicating the presence of deep convection. Similar thermal features to those identified by FM were also observed by BN in their analysis of soundings from a Gulf Coast convective cluster that formed on 26 April 1991.

The sounding of interest to BN, launched from Lake Charles, Louisiana (LCH), penetrated the western edge of the cluster's anvil. Fig. 2.7 shows the soundings for LCH and surrounding stations. The conditions at Jackson, Mississippi (JAN) and Slidell, Louisiana (SIL) are assumed to represent the undisturbed environment and adjusting environment, respectively. Close inspection of the LCH sounding reveals the development of a nearly adiabatic layer between 185 and 135 mb. Danielsen (1982) has observed similar adiabatic layers within the outflow of tropical mesoscale convection. Notice that the wet bulb potential temperature for this layer is identical to that at the surface. Reduced wind speeds in this layer (as compared to those at SIL) indicate the presence of low momentum air advected from lower levels. BN suggest that the sounding penetrated undilute air from an updraft that had ascended from the planetary boundary layer. As the moist, well–mixed, potentially warmer air is injected into the lower–stratosphere it produces the adiabatic layer with an accompanying stable layer between 280 and 250 mb. Notice also that the tropopause ascends to the top of the adiabatic layer. As shown in the SIL sounding, mixing causes the depth of the adiabatic and mixed layers to increase downward while weakening their intensity. The next section will summarize the proposed formation mechanisms for the kinematic and thermodynamics structures discussed above.

2.4 Explaining the Anomalies

As the convective updraft overshoots the tropopause and enters the stratosphere, it becomes significantly colder than its environment. According to FM, if this source of cold air can be maintained by a continuous updraft, then a quasi-permanent dome of cold air develops with a hydrostatically induced high pressure at its base. The cold pool may be further enhanced by the net downward transport of heat produced by the turbulent entrainment of warm stratospheric air into the outflow (Shutts and Gray, 1994). This

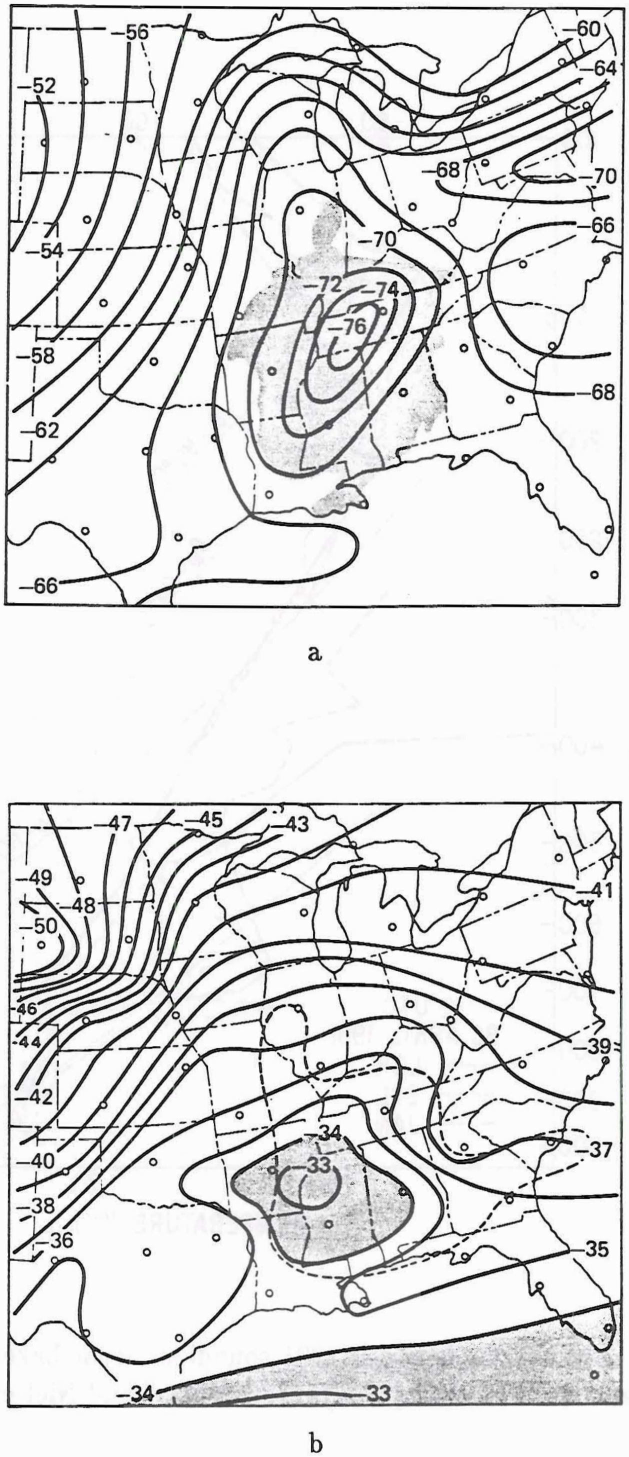
-56
-52
-60
-64
-68
-70
-54
-66
-70
-72
-74
-76
-58
-68
-62
-66
-47
-45
-43
-49
-48
-50
-41
-46
-44
-39
-42
-34
-37
-40
-33
-38
-36
-35
-34
-33

a

b

Figure 2.6: Temperature analysis at (a) 150 and (b) 300 mb for 1200 UTC on 7 May 1978. Shading indicates (a) −52°C or colder cloud tops, and (b) temperatures warmer than −34°C (From Fritsch and Maddox, 1981a).

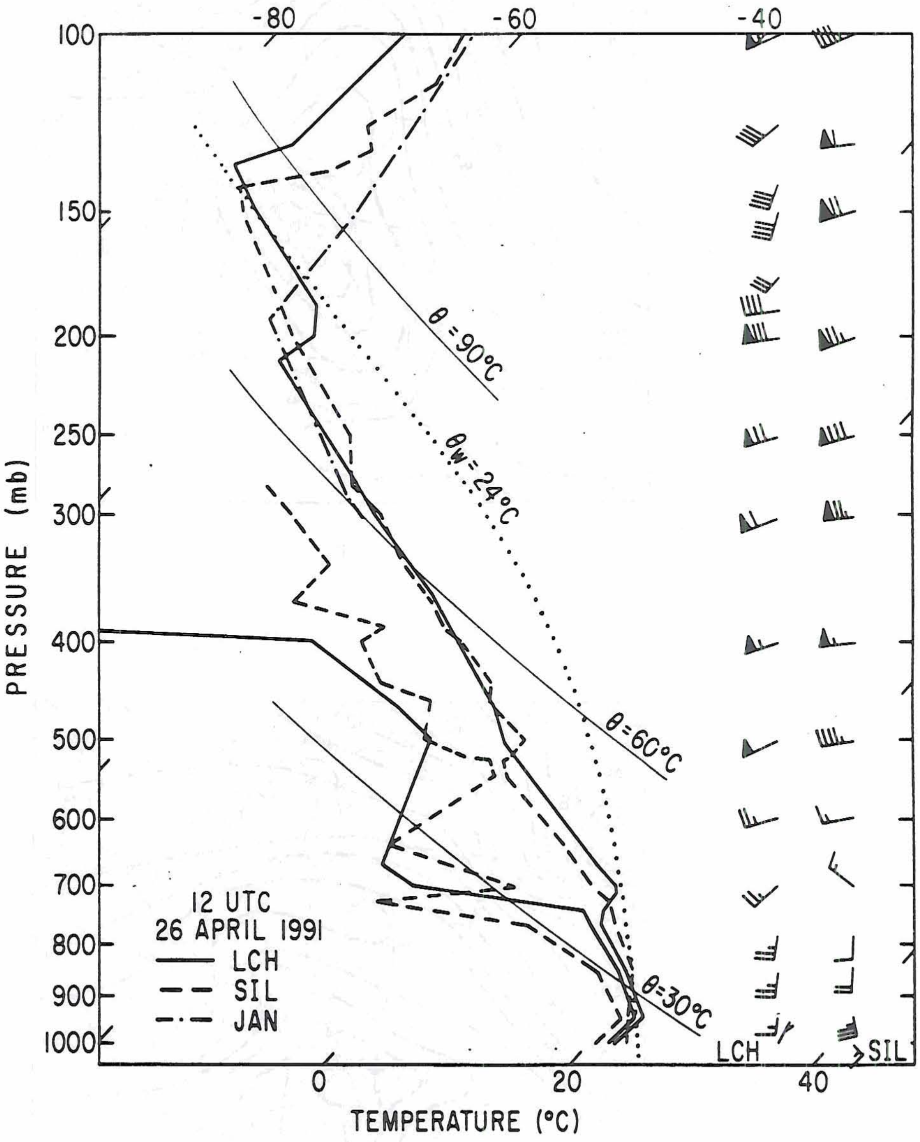

Figure 2.7: 1200 UTC, 26 April 1991 soundings from Lake Charles, LA (LCH); Slidell, LA (SIL); and Jackson, MS (JAN) (From Bosart and Nielsen, 1993).

effect will be considered in greater detail later in this chapter (Section 2.6). Using a mesoscale model, Fritsch and Brown (1982) simulated the cold pool by adding a shallow layer of cooling at the top of their convective heating profile. A region of high pressure was produced; however, it also developed (although weaker) when the cooling was absent. Another mechanism was implicitly present in their model.

Ninomiya (1971a) and Fankhauser (1974) theorized that mesoscale heating in the upper levels of the convection produces vertical motions and adiabatic cooling. Fritsch and Brown (1982) found that this source of cold air could also produce a region of high pressure albeit weaker than that produced by the updraft. Wetzel et al. (1983) propose that the heating increases the thickness of the layer, producing the mesohigh. Their observations show an increase of 60 m in the layer thickness. As the ascending mass from both the updraft and heating encounters the tropopause, it loses its buoyancy and spreads laterally.

If the injection of mass in the upper troposphere and lower stratosphere continues for a period longer than the inertial time scale (f^{-1}), the flow will geostrophically adjust toward gradient balance forming an anticyclonic lens. The amount of adjustment will depend on the horizontal scale of the outflow in relation to the Rossby radius of deformation ($\lambda = c_n/f$). Thermal wind balance requires that this circulation be accompanied by a cold (warm) temperature anomaly above (below). In Section 2.5, we will discuss the gradient adjustment process in more detail. Recall BN's observation that the lens initially contains less momentum than that of the tropospheric environment.

A lens of low momentum air at the tropopause may act as an obstacle to the mean flow (FM; Wetzel et al., 1983). Bernoulli's principle states that a decrease in speed as the mean flow encounters the obstacle will result in an increase in pressure. This is the least likely of the suggested mechanisms since the observed high pressure is located above the convection and not upstream. A final mechanism offered by Fritsch and Brown (1982), indicates the importance of radiation.

Cirrus clouds undergo radiational cooling to space along their tops and radiational warming from the surface along their bases. Such a gradient in the radiation profile may strengthen the dynamically–forced cold and warm anomalies mentioned previously (FM; Fritsch and Brown, 1982). This effect will be discussed in more detail in Section 2.6. In the next section, we will consider the impact of gradient adjustment on the balanced state of the system.

2.5 Understanding Gradient Adjustment

Most of the early investigations of atmospheric convection and gradient adjustment concentrated on the formation of cyclonic vortices by the compensating convergence of mass and angular momentum following the ascent of convective thermals (Inman, 1966; McIntyre, 1967; Sasaki and Friday, 1967; Wilkins et al., 1969; Friday, 1967, 1969; McDonald, 1990, 1992). Little attention was given to the circulations that form as the convection comes to rest at the level of neutral buoyancy. The earliest examination of mass injections and gradient adjustment came not from atmospheric studies but from studies of ocean dynamics.

Observations have revealed the presence of anticyclonic eddies within the oceans at a variety of scales (Armi and Zenk, 1984; Manley and Hunkins, 1985; Dugan et al., 1982). Oceanographers have speculated that some of these vortices are caused by deep water formation (Killworth, 1976, 1983; Gascard, 1978) and hydrothermal venting (Baker et al. 1989; Speer, 1989). Both numerical (Crépon et al., 1989; Barnier, et al., 1989; McDonald, 1992) and laboratory studies (Helfrich, 1994) have been conducted to understand these phenomena. Most notably, Gill et al. (1979) and Gill (1981) used numerical and laboratory experiments to understand the adjusted state that develops following the formation of deep water in the Greenland Sea.

Using a homogeneous, two–layer, shallow water model, Gill et al. (1979) examined the flow that develops following the gradual transfer of fluid from the upper to the lower layer. Model calculations clearly show the interface doming, or geopotential change, between the two fluids with a corresponding geostrophically balanced, anticyclonic circulation. Similar features to those obtained by the model were observed in laboratory experiments with the exception of cyclonic vorticity near the dome center associated with momentum transfer from the cyclonically rotating mass sink.

Expanding on the two-layer model, Gill (1981) studied the instantaneous injection of a homogeneous layer of fluid into a uniformly stratified, rotating environment. Assuming that the injection is instantaneous reduces the solution to an initial value problem. Also, by making the injection homogeneous and transforming to semi-geostrophic coordinates, the solution is isolated to the exterior fluid in the form of a linear Laplace equation. Gill found that the solution was not dependent on the transient state but only on the initial potential vorticity distributions. Fig. 2.8 shows the model derived temperature and velocity distribution. Notice the lenticular structure in the temperature field with corresponding baroclinic anticyclone. The aspect ratio of the lens scales as $\lambda/H = N/f$, where λ and H are the Rossby deformation radius and depth, respectively, and N and f are the buoyancy and inertial frequencies, respectively. Numerical experiments including viscous effects indicate that horizontal diffusion spreads the temperature field laterally, causing the lens to flatten and the circulation to weaken. Laboratory experiments conducted by Hedstrom and Armi (1988) have verified the viscous dependent aspect ratio. In numerical experiments similar to Gill's, Shutts (1987), Shutts et al. (1988), Shutts (1994), and Shutts and Gray (1994) have studied the impact of mass intrusions in the atmosphere.

Using a linearized, rectilinear, Lagrangian, parcel model, Shutts (1987) examined the thermodynamic and kinematic structure of a Boussinesq atmosphere following the rearrangement of the parcels. The balanced state has a lens structure at the level of neutral buoyancy similar to that obtained by Gill (1981), with a front along the axis of the sink formed by the compensating convergence. The aspect ratio of the lens is consistent with Gill's formulation. Shutts et al. (1988) extended the model to the axisymmetric case using semi-geostrophic coordinates.

Fig. 2.9 shows the results of this model for a mesoscale convective simulation. Notice that the vertical surface front does not form in this case due to the conservation of angular momentum; instead, a sloping front or "eye wall" forms as mass is drawn down into the sink. In addition to the balanced dynamics, Shutts (1994) and Shutts and Gray (1994) also considered the transient aspects of the geostrophic adjustment problem.

Shutts (1994) showed that the effect of rotation is to trap a portion of the energy in the balanced flow that would have otherwise been radiated away as gravity-inertia

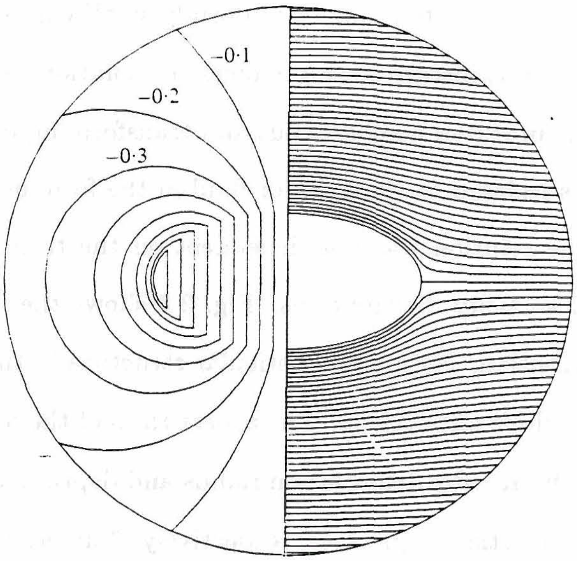

Figure 2.8: Contours of temperature (right) and velocity (left) from an analytic model of a homogeneous intrusion of fluid into a rotating, continuously stratified environment. The contour interval on both sides is 0.1 nondimensional units. The velocities scale as NH (From Gill, 1981).

waves. The amount of energy trapped is dependent on the scale of the disturbance in relation to λ. Using a rectilinear, anelastic, moist convective plume model, Shutts and Gray (1994) showed that 30-40% of the initial APE (APE_0) is partitioned to the final balanced kinetic energy (KE). This is approximately an order of magnitude greater than that predicted by Schubert et al.'s (1980) linear analysis (Shutts and Gray, 1994). Hack and Schubert (1986) showed that the amount of energy partitioned to the balanced flow increases as the inertial stability of the vortex increases. Partitioning the flow from an MCC simulation into balanced and unbalanced components, Olsson (1994) found that during the storm's life, as much as 84% of the total KE may be partitioned into the balanced KE.

CLMT explain that the scale of mesoscale disturbances is determined not by the linear form of the Rossby radius of deformation $\lambda = c_n/f$ but by the general form (Schubert et al.,1980)

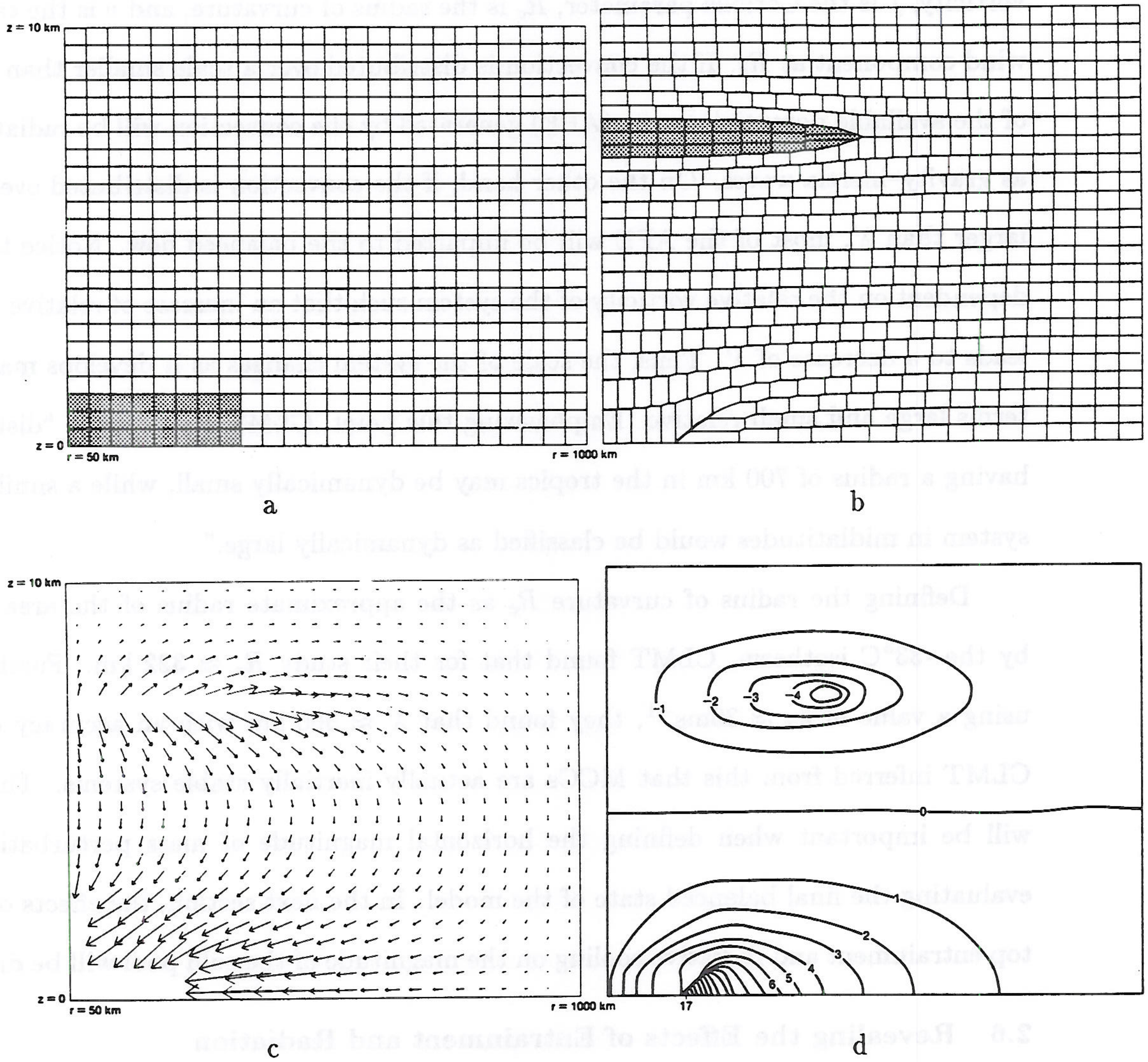

a

b

c

d

Figure 2.9: Results from an axisymmetric, Lagrangian parcel model. Fields shown are the (a) initial element configuration with shaded area being the positively buoyant elements (2.1K increase in θ with each element), (b) final element configuration with lens and "eye" wall structure, (c) parcel displacement field, and (d) the balanced tangential velocity (1 ms^{-1} contour interval). Initially, elements in the same horizontal plane have the same potential temperature while elements in the same vertical column have the same angular momentum (From Shutts et al., 1988).

$$\lambda' = \frac{c_n}{\sqrt{(\zeta + f)\left(2\frac{v}{R_c} + f\right)}}, \tag{2.1}$$

where c_n is the phase speed of a gravity–inertia wave, ζ is the vertical component of relative vorticity, f is the Coriolis parameter, R_c is the radius of curvature, and v is the tangential wind component at R_c. If the convection is distributed over a scale smaller than λ', most of the available potential energy (APE) generated by the convection will be radiated away as gravity–inertia waves. On the other hand, if the convection is distributed over a scale larger than λ', most of the APE will be imparted to the balanced flow. Notice that λ' is dependent on the relative vorticity of the system such that an increase of relative vorticity leads to a decrease of λ'. Thus, the scale of the system changes as it develops making the terms large and small relative. Emphasizing this point, CLMT state that a "disturbance having a radius of 700 km in the tropics may be dynamically small, while a similar–sized system in midlatitudes would be classified as dynamically large."

Defining the radius of curvature R_c as the approximate radius of the area covered by the -33°C isotherm, CLMT found that for their study $R_c \approx 322$ km. Furthermore, using a value of $c_n \approx 30\text{ms}^{-1}$, they found that $\lambda' \approx 300$ km with an accuracy of ±4%. CLMT inferred from this that MCCs are actually inertially stable systems. This result will be important when defining the horizontal magnitude of mass perturbations and evaluating the final balanced state of the model. In the next section, the effects of cloud–top entrainment and radiative cooling on the magnitude of the cold pool will be discussed.

2.6 Revealing the Effects of Entrainment and Radiation

2.6.1 Cooling by Entrainment

When shallow convection encounters an inversion, it entrains warm air from above the inversion. Ball (1960) showed that this entrainment results in a net downward transport of heat, causing the height of the inversion to increase while the layer below remains well mixed and nearly moist adiabatic. This process is essential to the dissipation of turbulent kinetic energy and the production of potential energy. In his studies of stratosphere–troposphere exchange, Danielsen (1968, 1982, 1993) has proposed a similar mechanism (shown in Fig. 2.10) for deep penetrative convection encountering the tropopause.

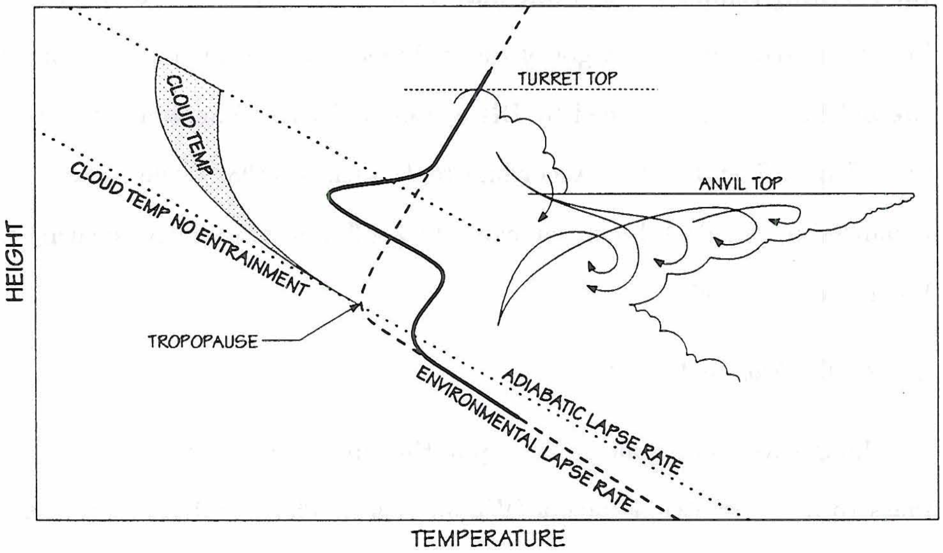

Figure 2.10: Theoretical mechanism for stratospheric anvil formation and its associated temperature distribution (From Danielsen, 1982).

As deep convection impinges on the tropopause, updrafts overshoot the level of neutral buoyancy and enter the stratosphere. On average, vertical velocities are about 20-60 ms^{-1} with penetrations of 1–3 km (Saunders, 1962). Increased static stability within the stratosphere causes the updraft to lose buoyancy and decelerate. Like a giant fountain, the decelerating air eventually collapses down onto the updraft.

Turbulent eddies, associated with shear instabilities, develop at the boundary of the overshooting updraft (Klaassen and Clark, 1985; Clark et al., 1988; Grabowski, 1989; Grabowski and Clark, 1991, 1993) and entrain warm stratospheric air. If the level of neutral buoyancy is the tropopause, the increased buoyancy of the diluted air causes the collapsing updraft to come to rest within the stratosphere. IR satellite imagery (Adler and Fenn, 1979; Fujita, 1982; Heymsfield and Blackmer, 1988; Ebert and Holland, 1992), aircraft observations (Adler et al., 1983; Spinhirne et al., 1983; Danielsen, 1981, 1993; Poulida et al., 1995) and numerical simulations (Adler and Mack, 1986; Schlesinger, 1990; Stenchikov et al., 1995) support the development of anvils within the stratosphere.

The entrainment and mixing within the stratospheric outflow result in a net downward transport of heat and the production of a well mixed, adiabatic layer with sharp temperature gradients along its horizontal boundaries. Ackerman et al. (1988) warns that the resulting temperature profile may be less than adiabatic (or even isothermal) depending on the structure and vigor of the turbulence within the layer. Notice that the shape of the LCH sounding obtained by BN agrees well with Danielsen's theoretical profile (compare Figs. 2.7 and 2.10). According to Danielsen (1982), the mixing within the layer is enhanced by the destabilization caused by differential radiative heating along the top and bottom of the anvil.

2.6.2 Cooling by Radiation

Longwave cooling along the top of the outflow causes θ–surfaces to "lift", transferring mass to lower isentropic layers (Wirth, 1995). These diabatic mass transfer mechanisms must be accounted for when considering the adjustment process. Johnson et al. (1990), in their analysis of squall lines, showed that diabatic cooling by radiation leads to mesoscale descent along the upper surface of the stratiform outflow.

Webster and Stephens (1980) have measured cloud–top cooling rates within the tropics of approximately 5–15°Cday^{-1} ($\sim$ .5°Chr^{-1}). Note that their work concentrates primarily on mid–level clouds and not on upper–tropospheric cirrus. Simulations of tropical MCSs by Wong et al. (1993 a, b) show cooling rates between 2 and 8°Cday^{-1}. Although no current measurements exist, similar cooling rates may be expected atop mid–latitude MCSs.

Chen and Cotton (1988) conducted sensitivity studies of a High Plains MCS simulation and found 2°C warming of the cloud–top in the absence of longwave radiative effects. Similar sensitivity analysis by Tao et al. (1993) for a mid–latitude squall line show cooling rates of 2–3°Cday^{-1}.

Starr and Cox's (1985a, b) emphasize that cloud–top cooling is enhanced during the evening. In particular, the additional cooling could have a significant impact on nocturnal systems such as MCCs (Wetzel et al., 1983). MCS simulations conducted by Tripoli and

Cotton (1989b) show an increase in cloud–top cooling from 4 to 16°Cday^{-1} during the evening.

Chapter 3

MODEL

3.1 Introduction

In the previous chapter, we discussed in detail the complex kinematic and thermodynamic structure within the lower–stratospheric outflow of an MCS. In addition, we considered the moderating effects of rotation, entrainment, and radiation. As a convective tower stretches through the depth of the troposphere, mass is rapidly redistributed producing an imbalance in the forces acting on the fluid. The nonlinear adjustment process that follows is partitioned into a transient and balanced component. During the transient adjustment, excess mass and energy are shed into the far-field through the propagation of gravity–inertia waves, leaving behind a mass field in hydrostatic and gradient balance. Solutions to the nonlinear transient adjustment are complicated (Shutts and Gray, 1994); however, the linearized form has been solved analytically (Schubert et al., 1980; Fulton and Schubert, 1980; Shutts, 1994). The purpose of this chapter is to describe the analytic development of an axisymmetric, nonlinear, balance model designed to find the adjusted state of an impulsively perturbed system using the conservation of potential vorticity (PV).

Since the core of this model's formulation is based on PV conservation, it will be profitable to first review the definition of PV, how convection generates PV anomalies, and how the balanced flow is extracted from the PV field (Section 3.2). Given this information, we will define the basic state with appropriate governing equations (Section 3.3) and develop a suitable model to extract the balanced state (Section 3.4). It will also be beneficial to analyze the model's energy and mass budgets to ensure that they are consistent (Section 3.5). The remainder of the chapter will explain the numerics used in solving the model (Section 3.6).

3.2 Thinking in Terms of PV

3.2.1 PV Definition

The foundations of PV thinking originate with the early formulations of circulation and vorticity by Helmholtz (1858), Kelvin (Thompson 1869, 1879), V. Bjerknes (1898), and others. As pointed out by Pedlosky (1979, § 2.5), the vorticity equation can describe the evolution of atmospheric motions but places no constraints on that evolution; whereas, we know that gravity (i.e., static stability) and planetary rotation (i.e., inertial stability) place unique restrictions on fluid motions within the atmosphere. In particular, thermal wind balance must be maintained.

As an example of this point, consider two axisymmetric, diabatically generated mass perturbations within a resting, statically stable atmosphere as shown in Fig. 3.1a and c. The APE of the system is increased by the adiabatic displacement of mass at the layer of injection/removal. As gravity–inertia waves transport mass radially, the APE_0 is converted into KE. Ultimately, the deflection of the radial flow by the Coriolis force draws the systems into geostrophic balance. The resulting balanced states are shown in Fig. 3.1b and d. Notice that a portion of the APE_0 must remain in order to maintain thermal wind balance. As stated by Shutts (1994), "rotation prevents the complete conversion of PE to KE through the conservation of angular momentum." Apparently, a unique relationship exists between changes in the APE (i.e., static stability) and the absolute vorticity.

While developing a new hydrodynamic vorticity equation, Ertel (1942) showed that, for adiabatic, inviscid motions, the static stability and absolute vorticity are related by the following material conservation relation:

$$\frac{D}{Dt}\left(\alpha\zeta_a \cdot \nabla\theta\right) = 0, \tag{3.1}$$

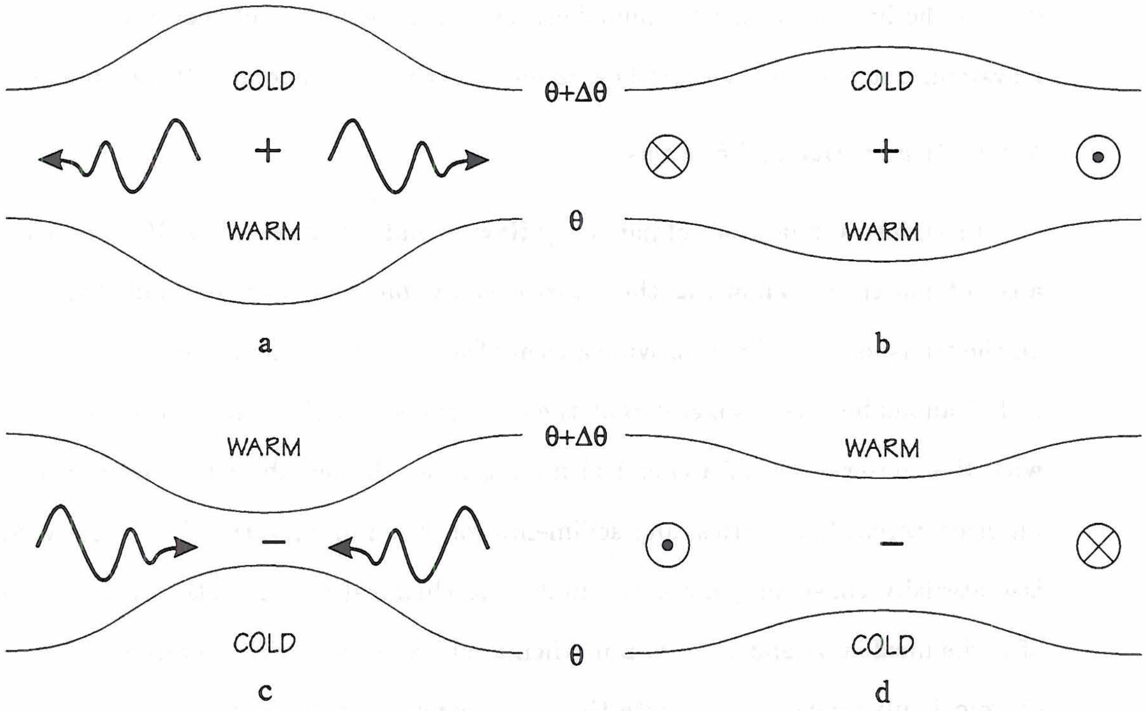

Figure 3.1: (a) Atmosphere perturbed by a mass source "+" with (b) the resulting balanced state. (c) Atmosphere perturbed by a mass sink "-" with (d) the resulting balanced state. The arrows indicate the direction of gravity wave propagation while the circle with a dot in the center denotes flow out of the paper and the circle with an "x" in the center denotes flow into the paper.

where $\alpha = 1/\rho$ is the specific volume, ζ_a is the three-dimensional absolute vorticity, and ∇ is the three-dimensional gradient operator. Amazingly, no approximations are involved in this result. It is valid for three-dimensional, nonhydrostatic, baroclinic flows at any scale. Rossby (1940) defined the parenthetical quantity the *potential vorticity* (PV)

$$P = \alpha\zeta_a \cdot \nabla\theta = \text{constant}. \tag{3.2}$$

Thus, variations in a parcel's static stability and inertial stability are constrained by the requirement that PV be materially conserved. Again, as Shutts (1994) explains, "the total energy is minimized subject to the Lagrangian conservation of potential temperature and angular momentum (Shutts and Cullen 1987); or, alternatively, the conservation of PV (Vallis 1992). In the non-rotational case, energy minimization results in a horizontally homogeneous end state with all the KE appearing in gravity-wave motion." Equation (3.2) defines the link between PV anomalies, and the kinematic and thermodynamic states of a system, but does not address how mass perturbations generate PV anomalies.

3.2.2 Impermeability Theorems

In a controversial[1] pair of papers by Haynes and McIntyre (1987, 1990, hereafter HM), a set of constraints known as the *impermeability theorems* were developed that set limits on the transport of PV and provide a useful framework for understanding the development of PV anomalies. HM suggest that the conservation of PV constitutes a *partial* analogy with the conservation of a chemical mixing ratio. In the absence of chemical reactions, diffusion across boundaries, and sedimentation, the mixing ratio of a chemical substance is materially conserved; however, unlike the chemical mixing ratio, which is composed of a chemical substance, PV is a mathematical construct with no physical analog to the chemical substance. To alleviate this discrepancy, HM define a quantity called *PV substance* (PVS) recognizing that, unlike the chemical substance, PVS is a signed quantity. HM demonstrated mathematically that PVS is trapped between isentropic surfaces and can only be fluxed along the surfaces. Based on this result, they developed the following theorems:

(i) *There can be no net transport of PVS across any isentropic surface.*

(ii) *PVS can neither be created nor destroyed, within a layer bounded by two isentropic surfaces. Corollary: PVS can only be created or destroyed where the layer terminates along a boundary.*

Remarkably, this is true even in the presence of diabatic and viscous processes. Consider how these restrictions, in conjunction with the mixing ratio analogy, might be used to visualize the generation of PV anomolies.

---

[1] Based on observational evidence, Danielson (1990) disputed Haynes and McIntyre's (1987) impermeability conclusions. In a follow-up paper, Haynes and McIntyre (1990) clarified their theory and demonstrated that the differences were primarily semantic.

Fig. 3.2 depicts the development of two mass perturbations and their corresponding PV anomalies induced by the diabatic redistribution of mass by moist convection. Let's examine the lower perturbation first. As mass is diabatically removed from the layer, the isentropes are drawn toward the perturbation by the adiabatic descent of mass filling the void left by the mass sink. According to theorem (i), the increased gradient of isentropic surfaces concentrates the PVS and increases the PVS mixing ratio (i.e., generating a positive PV anomaly). The opposite holds for the upper perturbation. Mass is diabatically injected into the layer causing the isentropes to spread apart. The decreased isentropic gradient dilutes the PVS and decreases the PVS mixing ratio (i.e., generating a negative PV anomaly). By comparing Figs. 3.1 and 3.2, we conclude that a positive(negative) PV anomaly is associated with cyclonic(anticyclonic) vorticity. An understanding of PV conservation combined with the constraints imposed by the impermeability theorems, provide a qualitative picture of the formation and influence of PV anomalies. This information alone, however, does not allow the mathematical extraction of the balanced flow from the distribution of PV.

3.2.3 Invertibility Requirements

Given the perturbed wind and mass fields, the initial PV distribution is obtainable from (3.2) while its future distribution may be forecast by (3.1); however, a problem develops when one attempts to extract the future state of the wind and mass fields from the forecast distribution of PV. For a given value of PV, (3.2) indicates an infinite number of kinematic and thermodynamic combinations. Obviously, additional information is needed.

As pointed out by Hoskins et al. (1985, hereafter HMR), the following conditions must be specified in order to invert the potential vorticity field and obtain a velocity and temperature field consistent with thermal wind balance:

(i) *A reference state must be defined.*

(ii) *Two balanced conditions must be specified.*

(iii) *The inversion problem must be solved globally with appropriate boundary conditions given.*

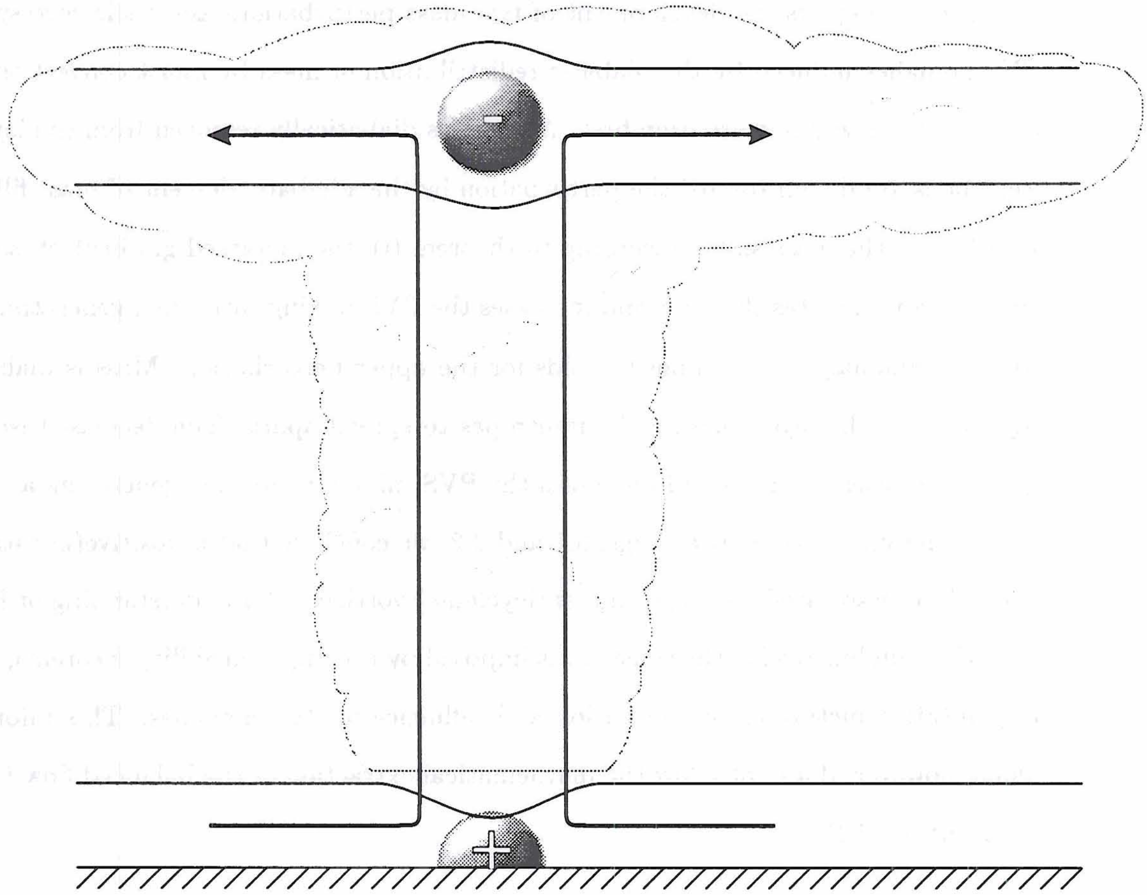

Figure 3.2: Generation of "+" and "-" PV anomalies by moist convection. Horizontal lines represent isentropic surfaces.

Since an anomaly refers to a deviation from some reference, condition (i) is necessary to clarify what is meant by PV anomaly. Conditions (ii) and (iii) will allow us to find a unique balanced state for a given distribution of PV. Notice in (3.2) that the PV is a function of three 3 variables, α, ζ_a and $\nabla\theta$. By specifying two balanced conditions relating the three variables, the PV is reduced to a function of one variable. The resulting system of equations is commonly referred to as the *invertibility principle.* Since the PV anomaly affects the flow both locally and into the far-field, the invertibility principle must be solved globally with appropriate boundary conditions specified. Thus, given an initial distribution of PV and knowing that it is materially conserved, we can solve for the final state of the system consistent with the balance conditions. If a local conservation relation can be developed, then the solution reduces to an initial value problem. Each of these requirements will be dealt with in following sections as the model evolves beginning with condition (i) — specification of the basic state.

3.3 Formulating the Problem of Moist Convection using PV Anomalies

3.3.1 Basic State and Governing Equations

For simplicity, we consider a stably stratified atmosphere at rest relative to an f-plane. Motions within the atmosphere are assumed quasi-static, adiabatic and inviscid. Since the basic state is statically stable (i.e., θ is monotonically increasing with height) and the motions are adiabatic, it will be convenient to use isentropic coordinates in the vertical. However, instead of θ, specific entropy

$$s = c_p \ln\left(\frac{\theta}{\theta_0}\right) = c_p \ln\left(\frac{T}{T_0}\right) - R_d \ln\left(\frac{p}{p_0}\right) \tag{3.3}$$

will be used, where c_p is the heat capacity of dry air at constant pressure, R_d is the gas constant of dry air, "0" denotes a constant reference value with $\theta_0 = T_0$, and the pressure p, density ρ and absolute temperature T are related by the ideal gas law $p = \rho R_d T$. The use of s yields a more convenient form of the hydrostatic equation in which the right hand side is simply T rather than the Exner function[2]. Fig. 3.3a illustrates the model basic state absolute temperature $\bar{T}(s)$ profile. In order to study the impact of stratospheric penetrations by convection, the tropopause is specified within the interior of the domain rather than using the top boundary. $\bar{T}$ was chosen because of its familiarity (e.g., atmospheric soundings), but it is the density profile that we will be most interested in since perturbations will be to the mass field.

Previous models have focused on basic state density profiles that were either Boussinesq (Gill et al., 1979; Shutts, 1987; McDonald, 1990; McDonald, 1992) or anelastic (Shutts, 1994; Shutts and Gray, 1994). In this model, we will consider mass perturbations superimposed on a continuously stratified atmosphere. Recall that the density in

---

[2] Exner function, $\Pi = c_p(p/p_0)^\kappa$.

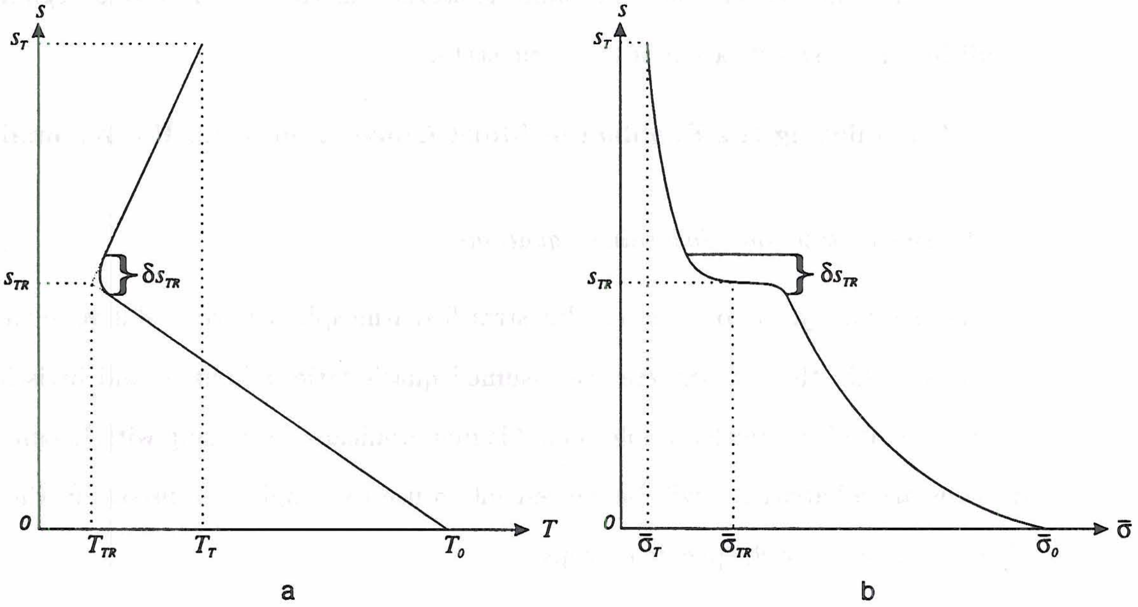

Figure 3.3: Basic state (a) temperature $\bar{T}(s)$ and (b) pseudodensity $\bar{\sigma}(s)$ profiles. δs_{TR} is the specific entropy difference over which the tropopause discontinuity is smoothed.

isentropic coordinates is given by the pseudodensity σ, where $\rho dz = -g^{-1}dp = g^{-1}\sigma ds$ such that $\sigma \equiv -\partial p/\partial s$. The basic state pseudodensity $\bar{\sigma}(s)$ profile (Fig. 3.3b) is derived from $\bar{T}(s)$ by solving for the pressure and then differentiating with respect to s. As an additional simplifying assumption, we will consider the axisymmetric case. The following set of primitive equations, in cylindrical coordinates, governs the motions within our hypothetical atmosphere:

$$\frac{Du}{Dt} - \left(f + \frac{v}{r}\right)v + \frac{\partial M}{\partial r} = 0, \tag{3.4}$$

$$\frac{Dv}{Dt} + \left(f + \frac{v}{r}\right)u = 0, \tag{3.5}$$

$$\frac{\partial M}{\partial s} = T, \tag{3.6}$$

$$\frac{D\sigma}{Dt} + \sigma\frac{\partial(ru)}{r\partial r} = 0, \tag{3.7}$$

where

$$\frac{D}{Dt} = \frac{\partial}{\partial t} + u\frac{\partial}{\partial r}, \tag{3.8}$$

is the material derivative, u and v are the radial and tangential wind components, respectively, and $M = c_pT + gz$ is the Montgomery potential or streamfunction. Poisson's diagnostic relationship

$$T = T_0 e^{s/c_p}\left(\frac{p}{p_0}\right)^{\kappa}, \tag{3.9}$$

may also be added to our equation set. Using the definition $\sigma = -\partial p/\partial s$, the above system of equations (3.4)–(3.9) is closed in the unknowns u, v, M, T, σ, and p.

The PV conservation relation for this system is found by combining the isentropic absolute vorticity equation

$$\frac{D\zeta_a}{Dt} + \zeta_a\frac{\partial(ru)}{r\partial r} = 0, \tag{3.10}$$

with the continuity equation (3.7), eliminating the isentropic divergence to obtain

$$\frac{D}{Dt}\left(\frac{\zeta_a}{\sigma}\right) = 0, \tag{3.11}$$

where, $\zeta_a = f + \partial(rv)/r\partial r$ is the isentropic absolute vorticity and $P = \zeta_a/\sigma$ is the PV. In later calculations, it will be convenient to use the inverse of P or the potential pseudodensity $\sigma^* = f/P = (f/\zeta_a)\sigma$ (i.e., the pseudodensity that a parcel would have if $\zeta_a = f$). With this definition, (3.11) may be rewritten as

$$\frac{D\sigma^*}{Dt} = 0. \tag{3.12}$$

With the basic state and governing equations defined, we need only define how the system will be perturbed.

3.3.2 Perturbation

Exactly what form the perturbation should take and how it should be imparted on the basic state presents some difficulties. As discussed in Chapter 2, convection is a highly turbulent process and as such is computationally cumbersome and difficult to model; however, simplifying assumptions to the primitive equations or to the form of the perturbation will reduce the complexity.

If the time scale of the convection is much less than the time scale of the adjustment (f^{-1}), then the movement of mass is assumed to occur instantaneously. Typically, the vertical motions within a convective updraft are rapid (10–15 min); whereas, the adjustment occurs over much longer time scales ($f^{-1} \approx 4$ hrs at 30°N) (Shutts, 1987; Helfrich, 1994). This assumption is valid for most forms of atmospheric convection. Even within an MCC, where convection may last for hours, the time scale over which mass is injected into the upper troposphere is much less than the adjustment time scale (Maddox, 1983). By making this assumption, the complex turbulent transport process is excluded. Observe that the fluid could be gradually injected, preserving a state of quasi-balance (Gill et al., 1979). Although useful, this method would eliminate our ability to treat the problem as an initial value problem. The pseudodensity perturbation can be expressed as follows:

$$\sigma'(r,s,0) = \hat{\sigma} F(r) G(s), \tag{3.13}$$

where $F(r)$ and $G(s)$ are the horizontal and vertical structure functions, respectively, and $\hat{\sigma}$ is the amplitude of the perturbation. The vertical and horizontal perturbation profiles are mathematically given by

$$F(r) = \begin{cases} 0 & r_2 \le r \le \infty, \\ 1 - I[(r-r_1)/(r_2-r_1)] & r_1 \le r \le r_2, \\ 1 & 0 \le r \le r_1, \end{cases} \tag{3.14}$$

and

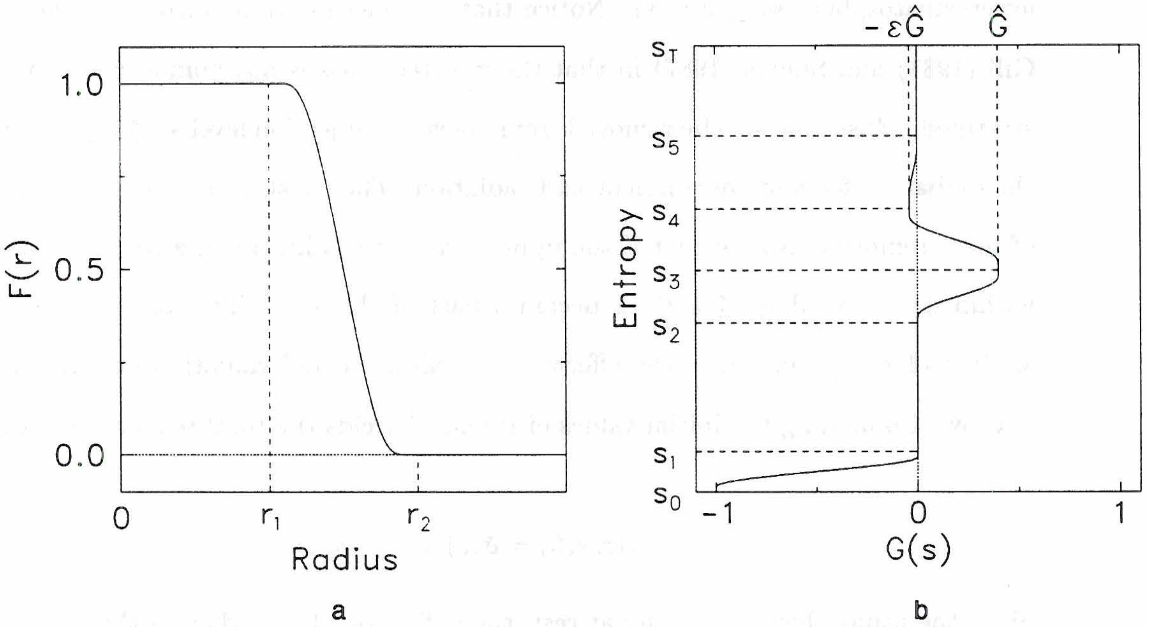

Figure 3.4: The (a) horizontal $F(r)$ and (b) vertical G(s) structure functions for a hypothetical MCS.

$$G(s) = \frac{1}{2}\begin{cases} 0 & s_5 \leq s \leq s_T, \\ -\epsilon\hat{G}\{1 - I[(s-s_4)/(s_5-s_4)]\} & s_4 \leq s \leq s_5, \\ \hat{G}\{1-(1+\epsilon)I[(s-s_3)(s_4-s_3)]\} & s_3 \leq s \leq s_4, \\ \hat{G}I[(s-s_2)(s_3-s_2)] & s_2 \leq s \leq s_3, \\ 0 & s_1 \leq s \leq s_2, \\ -[1 - I(s/s_1)] & 0 \leq s \leq s_1, \end{cases} \tag{3.15}$$

where

$$I(x) = \exp\{-(2x)^{-1}\ln(2)\exp[(1-2x)/(1-x)]\} \quad 0 \leq x \leq 1 \quad , \tag{3.16}$$

is a smooth unit step function with the properties $I(0) = 0$, $I(\frac{1}{2}) = \frac{1}{2}$, and $I(1) = 1$. Fig. 3.4 shows the structure functions. The constant $\hat{G}$ is defined such that mass continuity is maintained (i.e., $\int_0^{s_T} G(s)ds = 0$)

$$\hat{G} = \frac{s_1(1-\bar{I})}{(s_3-s_2)\bar{I} + (s_\tau - s_3)[1-(1+\epsilon)\bar{I}] + \epsilon(s_5-s_4)(\bar{I}-1)}, \tag{3.17}$$

where $\bar{I} = \int_0^1 I(x)dx \approx 0.501407$ is the mean of the smoothing function. Mass is removed from a shallow surface layer $0 \leq s \leq s_1$ and injected into the upper–troposphere or lower–stratosphere $s_2 \leq s \leq s_4$. Notice that this method differs from that employed by Gill (1981) and Shutts (1987) in that the injected mass is not homogeneous but is itself stratified. Mass may also be removed from above the injection level $s_4 \leq s \leq s_5$ simulating the diabatic effects of entrainment and radiation. The constant ϵ determines the amount of mass removed. Notice that if the upper mass sink is included, a section of the profile within the interval $s_3 \leq s \leq s_4$ becomes part of the sink. This proves to be a useful artifact of the profile since the effects of entrainment and radiation do extend into the outflow. Combining the initial values of $\bar{\sigma}$ and σ' yields the total perturbed mass field

$$\sigma(r,s,0) = \bar{\sigma}(s) + \sigma'(r,s,0). \tag{3.18}$$

Since the atmosphere is initially at rest, the definition of σ^* indicates that

$$\sigma^*(r,s,0) = \sigma(r,s,0). \tag{3.19}$$

With the initial distribution of σ^* defined, we can develop a model to extract the final balanced state of the system.

3.4 Extracting the Balanced State from the PV Distribution

3.4.1 Gradient Balance Condition

An instantaneous perturbation to the mass field disturbs the horizontal force balance $(f + v/r)v \neq \partial M/\partial r$ producing radial and tangential flow through (3.4) and (3.5), respectively. Adjustments to the mass field through continuity (3.7) will gradually draw the system toward a new balanced state.

HMR's provision (ii) states that two balanced conditions be specified. Requiring that motions be quasi-static meets the first condition. To maintain the highest level of generality, we choose gradient balance as the second. Using the definition for P, ζ_a and σ, the following set of equations describes the balanced motion:

$$\left(f + \frac{\partial(rv)}{r\partial r}\right)\sigma^* + f\frac{\partial p}{\partial s} = 0, \tag{3.20}$$

$$\left(f + \frac{v}{r}\right) v = \frac{\partial M}{\partial r}, \tag{3.21}$$

$$\frac{\partial M}{\partial s} = T_0 e^{s/c_p} \left(\frac{p}{p_0}\right)^{\kappa}. \tag{3.22}$$

According to HMR's condition (iii), appropriate boundary conditions must also be specified. We shall assume that both the upper and lower boundaries are isentropic surfaces. Furthermore, we shall require that the upper boundary be an isobaric surface while the lower boundary will be taken as a constant height surface. Along the outer boundary, the pressure approaches a far-field value $\bar{p}(s)$ representing the mean mass distribution. From these requirements, our boundary conditions become

$$p = p_T \qquad \text{at} \qquad s = s_T, \tag{3.23}$$

$$M = c_p T_0 \left(\frac{p}{p_0}\right)^{\kappa} \qquad \text{at} \qquad s = 0, \tag{3.24}$$

$$p \longrightarrow \bar{p} \qquad \text{as} \qquad r \longrightarrow \infty. \tag{3.25}$$

(3.20)–(3.25) represents the invertibility principle for $v(r,s)$, $M(r,s)$ and $p(r,s)$ in terms of $\sigma^*(r,s)$ and $\bar{p}(s)$. Thus, given the forecast distribution of σ^* from (3.12) and $\bar{p}(s)$, (3.20)–(3.22) are solved concurrently to find v, M and p. Alternatively, (3.20)–(3.22) could be combined into a single second order partial differential equation in terms of v, M or p, and σ^*. HMR and Thorpe (1985, 1986) discuss the invertibility principles for v and p, respectively; however, we choose to take the more common approach that, in its simplest form, inverts the Laplacian of a streamfunction (Raymond, 1992). In this case, the Laplacian is a complicated second order differential operator and the streamfunction is M. By multiplying (3.21) by r^3, differentiating this result with respect to r, and using (3.20) and (3.22) to eliminate v and p, we obtain the invertibility principle in terms of M,

$$\left[f^2 + \frac{\partial}{r^3\partial r}\left(r^3\frac{\partial M}{\partial r}\right)\right]\sigma^* + c_p\rho f\left(f + \frac{2v}{r}\right)e^{s/c_p}\frac{\partial}{\partial s}\left(e^{-s/c_p}\frac{\partial M}{\partial s}\right) = 0. \tag{3.26}$$

The boundary conditions (3.24)–(3.25) in terms of M become

$$\frac{\partial M}{\partial s} = T_T \qquad \text{at} \qquad s = s_T, \tag{3.27}$$

$$c_p\frac{\partial M}{\partial s} = M \qquad \text{at} \qquad s = 0, \tag{3.28}$$

$$M \rightarrow \bar{M}(s) \qquad \text{as} \qquad r \rightarrow \infty, \tag{3.29}$$

where $\bar{M}(s)$ is the far-field profile of M associated with $\bar{p}(s)$. Only one more difficulty separates us from a solution to this problem.

Consider for a moment the implications of the material conservation of σ^* (3.12) and the definition of the material conservation operator (3.8). Notice that the future distribution of σ^* depends on the radial advection by gravity-inertia waves. Our goal has been to neglect the transient adjustment, but the advection of σ^* by the transient oscillations prohibits this from occurring. This problem can be circumvented by transforming to a new coordinate system that makes u implicit in the coordinate transform and reduces the material conservation to a local conservation.

3.4.2 Gradient Balance Condition with Potential Radius Coordinate

In order to develop an alternate radial coordinate, we must identify some materially conserved property of the flow that will allow us to eliminate u from (3.8). Notice that the tangential momentum equation (3.4) may be rewritten in absolute angular momentum form

$$\frac{D}{Dt}\left(rv + \tfrac{1}{2}fr^2\right) = 0. \tag{3.30}$$

Using this conservation principle, Schubert and Hack (1983) defined the potential radius coordinate R which is related to physical radius by

$$\tfrac{1}{2} f R^2 = rv + \tfrac{1}{2} f r^2. \tag{3.31}$$

R represents the radius that a parcel in physical space must be moved, while conserving angular momentum, for its tangential wind component v to vanish. Mathematical consistency requires that the R coordinate be accompanied by a corresponding S and $\mathcal{T}$ coordinate in order to distinguish between partial derivatives at fixed r ($\partial/\partial s$ and $\partial/\partial t$) from those at fixed R ($\partial/\partial S$ and $\partial/\partial \mathcal{T}$). Derivatives in either space are related by

$$\left(\frac{\partial}{\partial r}, \frac{\partial}{\partial s}, \frac{\partial}{\partial t}\right) = \left(\frac{\partial R}{\partial r}\frac{\partial}{\partial R}, \frac{\partial R}{\partial s}\frac{\partial}{\partial R} + \frac{\partial}{\partial S}, \frac{\partial R}{\partial t}\frac{\partial}{\partial R} + \frac{\partial}{\partial \mathcal{T}}\right). \tag{3.32}$$

Applying (3.32) to (3.8) reveals that

$$\frac{D}{Dt} = \frac{\partial}{\partial \mathcal{T}}. \tag{3.33}$$

Advection by u has been eliminated from the calculation by making it implicit in the transformation. The material conservation in physical space has been converted into a local conservation in transformed space allowing us to rewrite (3.12) as

$$\frac{\partial \sigma^*}{\partial \mathcal{T}} = 0, \tag{3.34}$$

where σ^* in the transformed coordinate may be written in Jacobian form

$$\sigma^* = \frac{f}{\zeta_a}\sigma = -\frac{\partial(\frac{1}{2}r^2)}{\partial(\frac{1}{2}R^2)}\frac{\partial p}{\partial s} = -\frac{\partial(\frac{1}{2}r^2, s)}{\partial(\frac{1}{2}R^2, S)}\frac{\partial(\frac{1}{2}r^2, p)}{\partial(\frac{1}{2}r^2, s)} = -\frac{\partial(\frac{1}{2}r^2, p)}{\partial(\frac{1}{2}R^2, S)}. \tag{3.35}$$

With (3.32) and (3.35), the invertibility principle (3.26) transforms to

$$\sigma^* + \frac{\partial(\frac{1}{2}r^2, p)}{\partial(\frac{1}{2}R^2, S)} = 0, \tag{3.36}$$

$$f v^* = \frac{\partial \mathcal{M}}{\partial R}, \tag{3.37}$$

$$\frac{\partial \mathcal{M}}{\partial S} = T_0 e^{s/c_p} \left(\frac{p}{p_0}\right)^{\kappa}, \tag{3.38}$$

where $\mathcal{M} = M + \frac{1}{2}v^2$ and $v^* = (R/r)v$ are the transformed streamfunction and tangential velocity, respectively. Combining (3.36)–(3.38), a single expression for the invertibility principle in terms of $\mathcal{M}$ is obtained

$$\left[f^2 - R^3 \frac{\partial}{\partial R}\left(\frac{\partial \mathcal{M}}{R^3 \partial R}\right)\right] e^{S/c_p} \frac{\partial}{\partial S}\left(e^{-S/c_p} \frac{\partial \mathcal{M}}{\partial S}\right)$$
$$+ \left(\frac{\partial^2 \mathcal{M}}{\partial R \partial S}\right)^2 + \frac{\sigma^*}{\rho c_p}\left(f + \frac{2}{f}\frac{\partial \mathcal{M}}{R \partial R}\right)^2 = 0. \tag{3.39}$$

The upper and lower boundary conditions remain the same except for being expressed in transformed coordinates

$$\frac{\partial \mathcal{M}}{\partial S} = T_T \qquad \text{at} \qquad S = S_T, \tag{3.40}$$

$$\left(f^2 + \frac{2}{R}\frac{\partial \mathcal{M}}{\partial R}\right)\left(\mathcal{M} - c_p \frac{\partial \mathcal{M}}{\partial S}\right) - \frac{1}{2}\left(\frac{\partial \mathcal{M}}{\partial R}\right)^2 = 0 \qquad \text{at} \qquad S = 0, \tag{3.41}$$

where $S_T = c_p \ln(\theta_T/\theta_0)$. Along the outer boundary $R = R_{max}$, a boundary condition (Dirichlet[3]) that simulates an infinite domain is adopted. If $R_{max} \gg \lambda'$, where λ' is associated with the primary mode of the forcing, then σ^* and $\mathcal{M}$ along the outer boundary are assumed independent of R. With this assumption, the invertibility principle at $R = R_{max}$ is solved as a one-dimensional problem in S. Specifically, $\sigma^*(R_{max}, S) = \sigma(R_{max}, S) = -\partial p/\partial S$ is integrated to obtain p and (3.38) is integrated along R_{max} to obtain $\mathcal{M}$.

No physical boundary is actually present at $R = 0$; consequently, instead of defining a boundary condition here, we will find a limiting form of the invertibility principle. We begin with the average vorticity within a horizontal circle of radius r

---

[3] Given a function $u(x, y, z)$, the solution of the Laplacian, $\nabla^2 u = 0$, over a region R with boundary condition $u(x, y, z) = f(x, y, z)$ on the boundary C is called a *Dirichlet problem.* If the boundary curve C and the boundary value function f are reasonably well behaved, then a unique solution exists to the problem.

$$\frac{2}{r^2}\int_0^r \zeta r' dr' = f + \frac{2v}{r} = f + \frac{2}{f}\frac{\partial \mathcal{M}}{R\partial R}. \tag{3.42}$$

If ζ approaches some finite limit ζ_0 as $r \rightarrow 0$, then $v = O(r)$. This being the case, according to the definition of R, r and R must tend toward zero together (i.e., $r = O(R)$ and $R = O(r)$). The limit of (3.42) as $r \rightarrow 0$ is

$$\zeta_0 = \lim_{R\rightarrow 0}\left(f + \frac{2}{f}\frac{\partial \mathcal{M}}{R\partial R}\right). \tag{3.43}$$

Recognizing from (3.37) that $\lim\limits_{R\rightarrow 0} \partial\mathcal{M}/\partial R = 0$, we can apply L'Hôpital's Rule[4] to (3.43) giving

$$\zeta = f + \frac{2}{f}\frac{\partial^2 \mathcal{M}}{\partial R^2} \quad \text{at} \quad R = 0. \tag{3.44}$$

Substituting this expression into $\sigma = (\zeta/f)\sigma^*$ along with the definition of σ, the ideal gas law, and the hydrostatic relation (3.38), we obtain the following invertibility relation along $R = 0$

$$\left(1 + \frac{2}{f^2}\frac{\partial^2 \mathcal{M}}{\partial R^2}\right)\sigma^* + \rho c_p e^{S/c_p}\frac{\partial}{\partial S}\left(e^{-S/c_p}\frac{\partial \mathcal{M}}{\partial S}\right) = 0 \quad \text{at} \quad R = 0. \tag{3.45}$$

The upper boundary condition associated with this invertibility principle remains unchanged

$$\frac{\partial \mathcal{M}}{\partial S} = T_T \quad \text{at} \quad R = 0,\ S = S_T; \tag{3.46}$$

however, the lower boundary condition becomes

$$\mathcal{M} - c_p\frac{\partial \mathcal{M}}{\partial S} = 0 \quad \text{at} \quad R = 0,\ S = 0. \tag{3.47}$$

(3.45)–(3.47) represents the invertibility principle at $R = 0$.

---

[4] If $\lim f(x)/g(x)$ results in the indeterminate form 0/0 or ∞/∞, then the $\lim f(x)/g(x) = \lim f'(x)/g'(x)$ provided that the latter limit exists (or is infinite).

3.5 Analyzing the Balanced Fields

3.5.1 Energetics

When developing a numerical model, it is always prudent to analyze the energy of the system to ensure that it is consistent with your formulation and the phenomena being modeled. The flux form of the KE equation for (3.4)–(3.9) is

$$\frac{\partial(\sigma K)}{\partial t}+\frac{\partial(ru\sigma K)}{r\partial r}+\sigma u\frac{\partial M}{\partial r}=0. \tag{3.48}$$

where $K=\frac{1}{2}(u^2+v^2)$ is the KE. Applying the definitions $M=c_pT+gz$ and $\sigma=-\partial p/\partial s$, and remembering that the flow is adiabatic, it can be shown that

$$\frac{\partial(\sigma K)}{\partial t}+\frac{\partial[ru\sigma(K+\phi)]}{r\partial r}+\frac{\partial}{\partial s}\left(-\phi\frac{\partial p}{\partial t}\right)+\sigma\alpha\omega=0, \tag{3.49}$$

where $\omega=Dp/Dt$ is the vertical p-velocity. KE is generated through thermodynamic expansion and dissipated through work done along the boundaries by pressure. Similarly, the potential energy (PE) is given by

$$\frac{\partial(\sigma H)}{\partial t}+\frac{\partial(ru\sigma H)}{r\partial r}-\sigma\alpha\omega=0. \tag{3.50}$$

where $H=c_pT$ is the enthalpy. Notice that $\sigma\alpha\omega$ represents the conversion between KE and PE. Summing (3.49) and (3.50) yields the total energy equation

$$\frac{\partial[\sigma(K+H)]}{\partial t}+\frac{\partial[ru\sigma(K+M)]}{r\partial r}+\frac{\partial}{\partial s}\left(-\phi\frac{\partial p}{\partial t}\right)=0. \tag{3.51}$$

To find the total energy of the system, we integrate over the domain noting that at the upper boundary $\partial p/\partial t=0$ and at the lower boundary $\phi=0$

$$\frac{d}{dt}(\mathcal{K}+\mathcal{H})=\langle ru\sigma(K+M)\rangle_{r=r_{max}}, \tag{3.52}$$

where $\langle\ \rangle=\int_0^{s_T}(\ )\,ds$,

$$\mathcal{K}=\iint\sigma Krdrds, \tag{3.53}$$

is the total KE and

$$\mathcal{H} = \iint \sigma H r dr ds, \tag{3.54}$$

is the total PE. Notice that the total energy is not conserved by the system. During the transient adjustment, gravity-inertia waves transport KE and PE across the outer boundary $r = r_{max}$ and out of the system. Using the definition of σ and (3.9), $\mathcal{H}$ may be rewritten

$$\mathcal{H} = \frac{\theta_0 p_0}{1+\kappa} \iint \left(\frac{p}{p_0}\right)^{1+\kappa} e^{s/c_p} r dr ds. \tag{3.55}$$

The minimum $\mathcal{H}$ obtainable by adiabatically redistributing mass is

$$\bar{\mathcal{H}} = \frac{\theta_0 p_0}{1+\kappa} \iint \left(\frac{\bar{p}}{p_0}\right)^{1+\kappa} e^{s/c_p} r dr ds, \tag{3.56}$$

where $\bar{p} = r_{max}^{-2} \int_0^{r_{max}} p(s) r dr$ is the averages pressure on an isentropic surface. The difference $\mathcal{H} - \bar{\mathcal{H}}$ is the amount of PE that may be converted into KE (i.e., the APE)

$$APE = \frac{\theta_0 p_0}{1+\kappa} \iint \left[\left(\frac{p}{p_0}\right)^{1+\kappa} - \left(\frac{\bar{p}}{p_0}\right)^{1+\kappa}\right] e^{s/c_p} r dr ds. \tag{3.57}$$

Notice that the APE is also dependent on the outer boundary. The APE, as defined by Lorenz (1955), is defined for a finite horizontally boundless domain (i.e., an atmosphere bounding a spherical surface). As r_{max} is increased, the APE will decrease. A similar problem was encountered by Shutts and Gray (1994). They found that the outer boundary must be at least a Rossby deformation radius away from the perturbation. Model sensitivity studies show that an outer boundary distance of 2000 km is sufficient for the simulations to be considered in the next chapter.

3.5.2 Mass Removed

The intensity of the resulting balanced circulations will obviously be a function of the amount of mass that is redistributed. We could compare the balanced flow to $\hat{\sigma}$; however, the physical meaning of $\hat{\sigma}$ is difficult to grasp. Instead, we choose to compare the balanced than a single solution to the coordinate is obtained. To improve on this result and improve the model stability, the dependence of ρ on M is accounted for by solving a Newtonian iteration on M. When the mass perturbation is relatively strong, the nonlinearities may cause the solution to become unstable. Under this circumstance, a continuation method is employed.

Using a weaker solution as the initial approximation to the perturbed field, the relaxation is continued. As many as ten continuations may be used to obtain a stable solution. Once a solution has been obtained, the resulting fields are transformed from (R, S) to (r, z) using cubic Hermite splines with monotonicity preserved.

Chapter 4

RESULTS

4.1 Introduction

In Chapter 3, a nonlinear, axisymmetric, gradient balanced model was developed to compute the adjusted state of an initially stationary, continuously stratified atmosphere following an instantaneous vertical redistribution of mass. This chapter will present and discuss results from numerous simulations conducted with the model. First, a control simulation is developed and compared to the observational data presented in Chapter 2 (Section 4.2). A series of sensitivity tests are then performed to determine the effects of variable forcing, static stability, latitude, and cloud–top cooling on vortex structure and strength (Section 4.3).

4.2 Developing the Control Simulation

In this study, the control simulation serves a dual purpose. First, as with any experimental control, it is used as a base for sensitivity analysis; however, for our purposes, it will also be used as a model comparison to observational data. By designing the control in this way, the physics of the model can be validated against observational evidence prior to conducting the sensitivity studies. With this in mind, the control simulation is developed in the following sections.

4.2.1 Initial Conditions

The basic state, initial conditions for the control simulation, as defined by the temperature profile $\bar{T}(s)$ (Fig. 3.3a), are obtained from the observational data in Chapter 2 and are listed in Table 4.1a. Most of the initial conditions are drawn from the JAN sounding (Fig. 2.7). Although this sounding is not complete, it does show the height of the tropopause approximately 350 km from LCH and according to BN, is representative of other soundings far removed from the convection. To simplify the analytic form of $\bar{T}(s)$ in relation to the JAN sounding, the stratospheric lapse rate is assumed to be isothermal throughout its depth while the tropospheric lapse rate linearly increases (in isentropic coordinates) to the surface. A surface temperature is chosen which reproduces the average lapse rate of the LCH and SIL soundings. Plotted in Fig. 4.3 as the dashed curve is the resulting $\bar{T}(s)$ profile. This profile is converted to pressure and then differentiated with respect to entropy to obtain the initial $\bar{\sigma}(s)$ profile shown in Fig. 4.1a.

Parameter Name	Symbol	Value
latitude	ϕ	30°N
rotation rate	Ω	$7.292\times10^{-5}s^{-1}$
top entropy	s_T	1.0 (100 mb)
top temperature	T_T	$-60C$
tropopause entropy	s_{TR}	0.37 (200 mb)
tropopause temperature	T_{TR}	$-60C$
tropopause depth	δs_{TR}	$1C$
surface temperature	T_0	$26C$

a

Parameter Name	Symbol	Value
perturbation radius	r_2	300 km
smoothing radius	r_1	240 km
perturbation amplitude	σ	3.6 kgKm^{-3}
entrainment amplitude	ϵ	0
perturbation height parameters from Fig.	s_4	0.64 (150 mb)
	s_3	0.49 (175 mb)
	s_2	0.37 (200 mb)
	s_1	0.09 (700 mb)

b

Table 4.1: Control settings of the (a) basic state and (b) perturbation parameters. The values of entropy $s = c_p \ln(\theta/\theta_0)$, have been nondimensionalized by $s_T = c_p \ln(\theta_T/\theta_0)$. To further clarify the meaning of these values, equivalent pressure level have been included.

Similarly, the perturbation initial conditions, as defined by the $F(r)$ and $G(s)$ profiles illustrated in Fig. 3.4, are obtained from the observational data in Chapter 2 and are listed in Table 4.1b. The perturbation radius r_2 was chosen by estimating the average radius of the cloud shields observed by FM and BN. Both were found to be consistent with CLMT's composite values of R_c. Obviously the mass forcing within the outflow is not constant across r_2 but gradually diminishes near the boundary. To account for this, the mass perturbation is radially smoothed to zero over the outer 60 km of r_2. Since the model is impulsively rather than gradually forced, the magnitude of the mass forcing $\hat{\sigma}$ is restricted to the amount of mass available in the basic state at each level $\bar{\sigma}(s)$ which ranges from 0.112 $\mathrm{kgKm^{-3}}$ at the top to 3.774 $\mathrm{kgKm^{-3}}$ at the surface. In the vertical, the depth of the mass sink s_1 was chosen by considering both the planetary boundary layer depth at LCH (Fig. 2.7) and the depth of surface convergence analyzed by CLMT (Fig. 2.5a). Likewise, the depth and vertical placement of the mass injection were chosen by considering the structure of the outflow at LCH. Notice that s_5 is absent from the table. This parameter is only used when cloud-top cooling is included (i.e., $\epsilon \neq 0$). The resulting vertical profile of $G(s)$ is shown in Fig. 4.1b. Both $\bar{\sigma}(s)$ and $\sigma'(r,s) = \hat{\sigma}F(r)G(s)$ are combined to produce $\sigma(r,s)$, the convectively perturbed mass distribution, which for an atmosphere at rest is simply $\sigma^*(r,s)$ (Fig. 4.4).

Notice that the thermodynamic structure of the troposphere is markedly altered by the impulsive redistribution of mass. As a clue to this change, Fig. 4.4 shows that the center of the σ^* anomaly *appears* to be below the tropopause (or the base of the mass injection) in pressure coordinates but not in isentropic coordinates. As the atmospheric center of mass is shifted upward, a hydrostatic pressure increase develops through the column extending from the top of the perturbation to the surface (Fig. 4.2). This pressure anomaly not only increases the tropopause pressure, causing the injection to appear deeper in isobaric coordinates, but also adiabatically warms the column, producing a 10–15°C temperature change between 200 and 300 mb (Fig. 4.3).

With the initial σ^* field defined from σ, the invertibility relation is solved and the balanced state of the control simulation obtained (Figs. 4.5–4.10). To explain the structure of the balanced state, in relation to the initial structure, we must understand, at least qualitatively, the transient adjustment that has occurred.

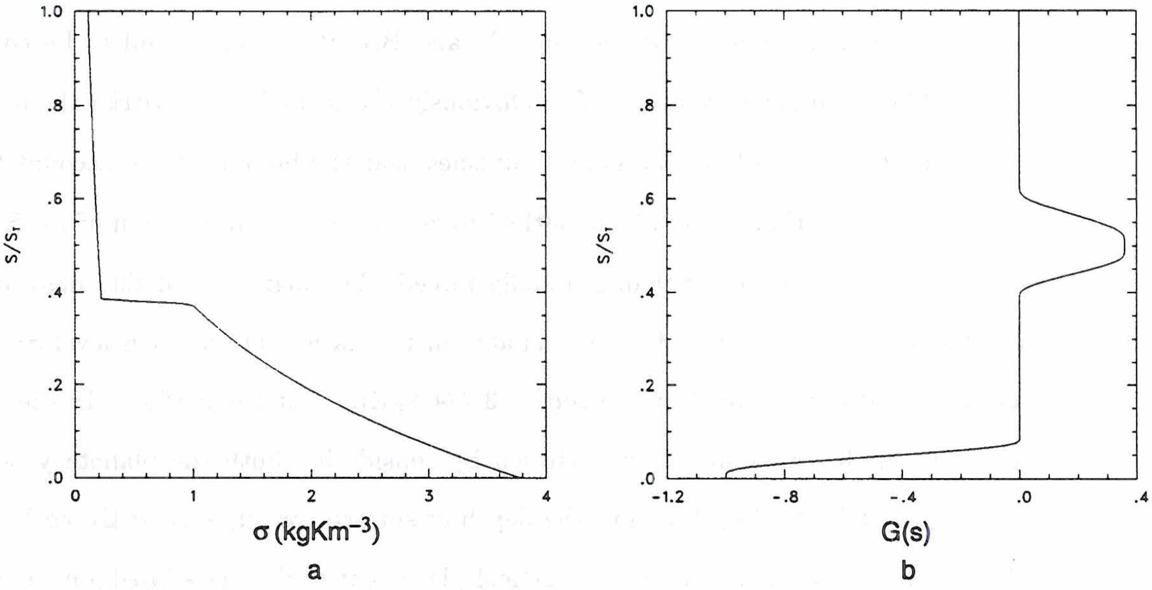

Figure 4.1: Control simulation initial (a) $\bar{\sigma}(s)$ and (b) $G(s)$ profiles.

4.2.2 Balanced State

Horizontal force imbalances, produced by the mass perturbation, generate gravity–inertia waves which transport mass radially. As a result, σ^* is materially advected outward, increasing the radial extent of the anomaly (compare Fig. 4.4 with Fig. 4.5). Recognizing that $r = R$ for an atmosphere initially at rest, we can determine the amount of displacement from the final distribution of R (Fig. 4.10). Compare these displacements with those obtained by Shutts et al. (1988) (Fig. 2.9c). The nonlinear advection by gravity–inertia waves, implicit in the coordinate transformation, is clearly evident. If the displacements are large relative to λ', the flow will adjust toward gradient balance producing the anticyclonic anomaly shown in Fig. 4.6a.

The outward transport of mass also causes the initial hydrostatic pressure anomaly to decrease, adiabatically cooling the troposphere. However, it will not cool back to its initial temperature (Fig. 4.6b) due to the small amount of mass that remains following the adjustment. Less clear in Figs. 4.5–4.6 are the vertical displacements (see Fig. 2.9c) produced during the adjustment.

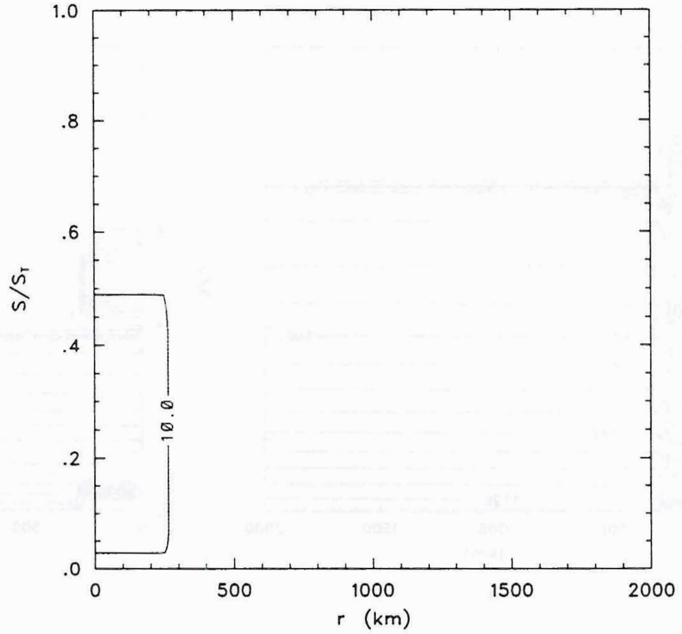

Figure 4.2: Control simulation, hydrostatic pressure anomaly (10 mb contour interval).

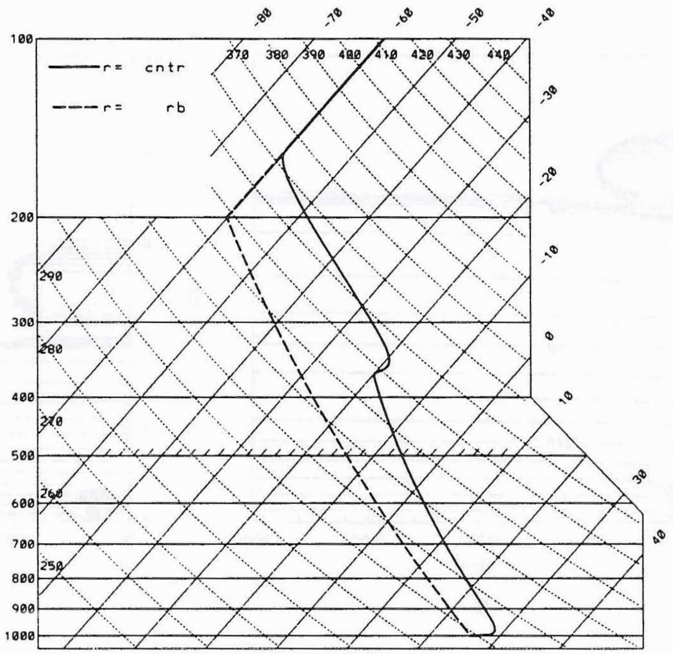

Figure 4.3: Control simulation, basic state (dashed) and perturbation (solid) temperature profiles.

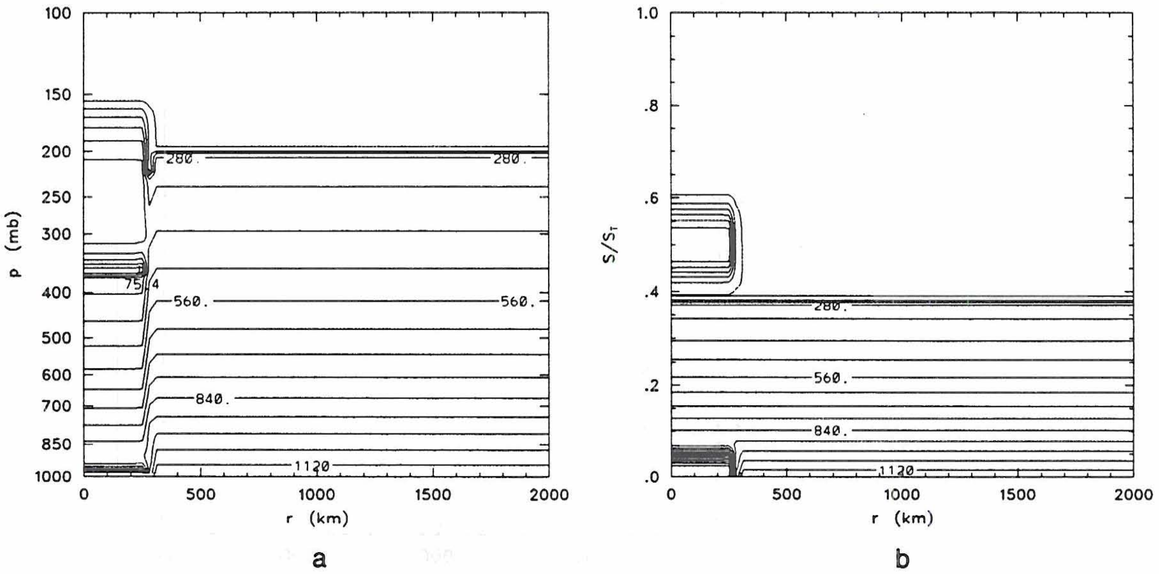

Figure 4.4: Control simulation initial σ^* field in (a) isobaric and (b) isentropic coordinates (70 kgKm^{-3} contour interval). Notice the change in the perturbation depth between (a) and (b).

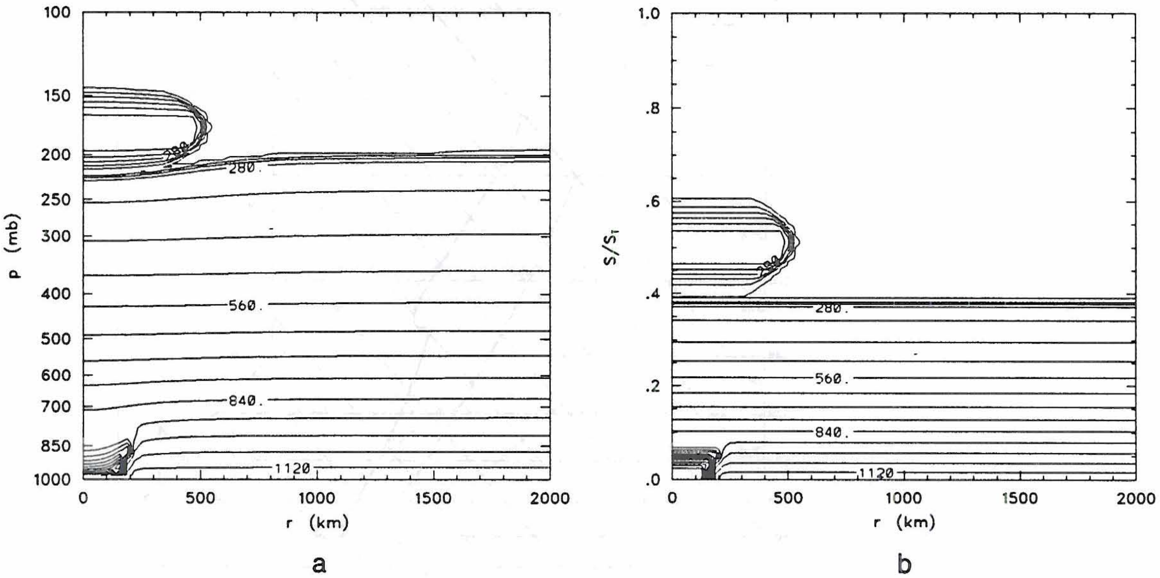

Figure 4.5: Same as Fig. 4.4 except that the fields are for the adjusted state. It appears that the perturbation forces the tropopause downward along its base and produces an additional inversion along its top. Notice that the sloping "eye" wall structure on the outer edge of the surface σ^* anomaly is similar to that obtained by Shutts et al. (1988).

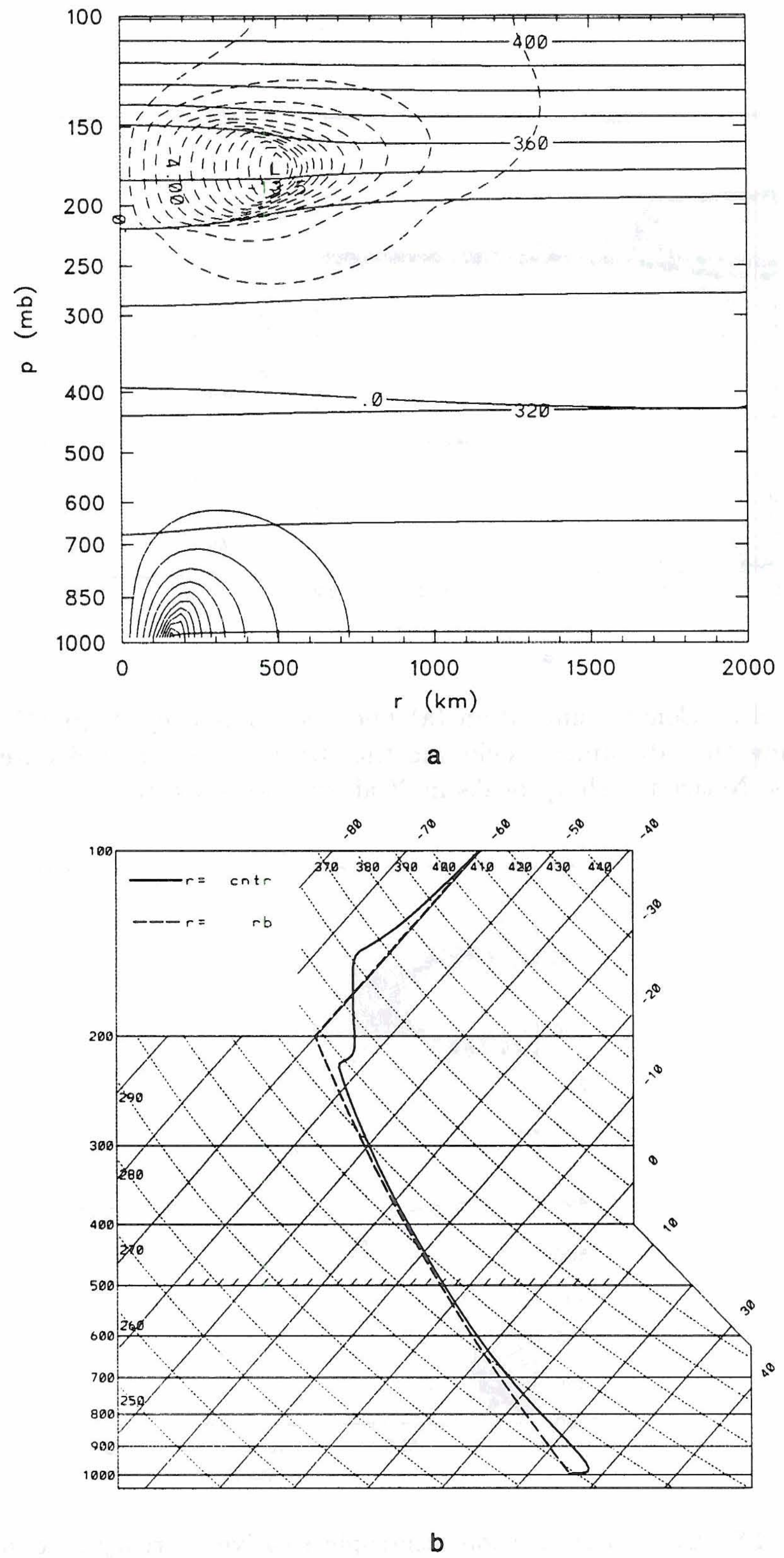

Figure 4.6: Control simulation adjusted state including the (a) tangential velocity v (1 ms^{-1} contour interval) and potential temperature θ fields (10 K contour interval), and the (b) basic state (dashed) and adjusted (solid) temperature profiles.

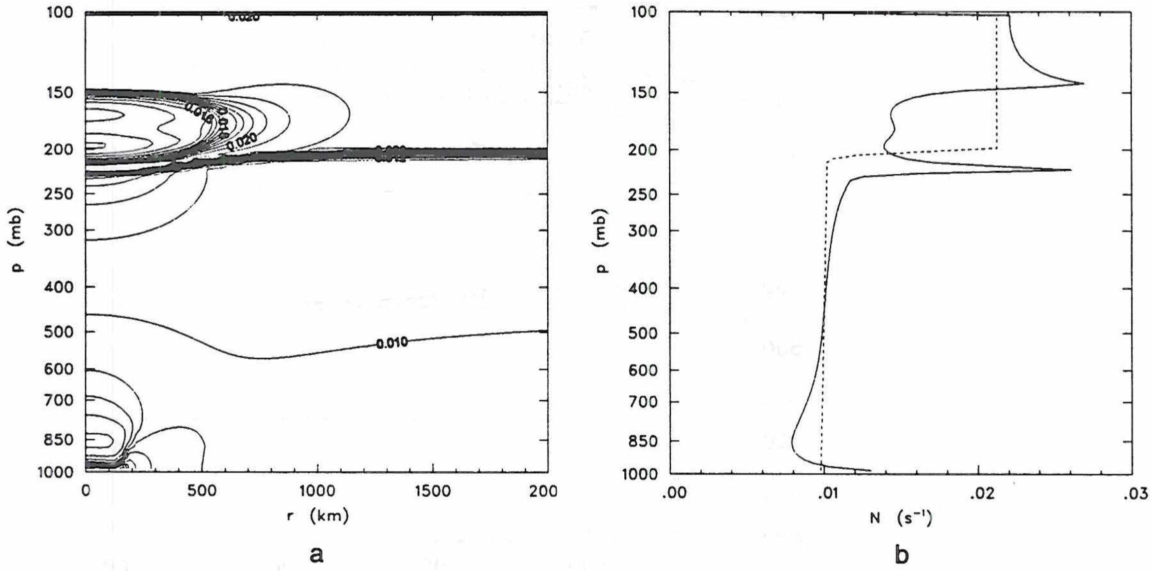

Figure 4.7: Control simulation (a) buoyancy frequency N (0.005 s^{-1} contour interval) following the adjustment including the (b) inner (solid) and outer (dashed) boundary profiles. Notice the sharp peaks in N above and below the perturbation.

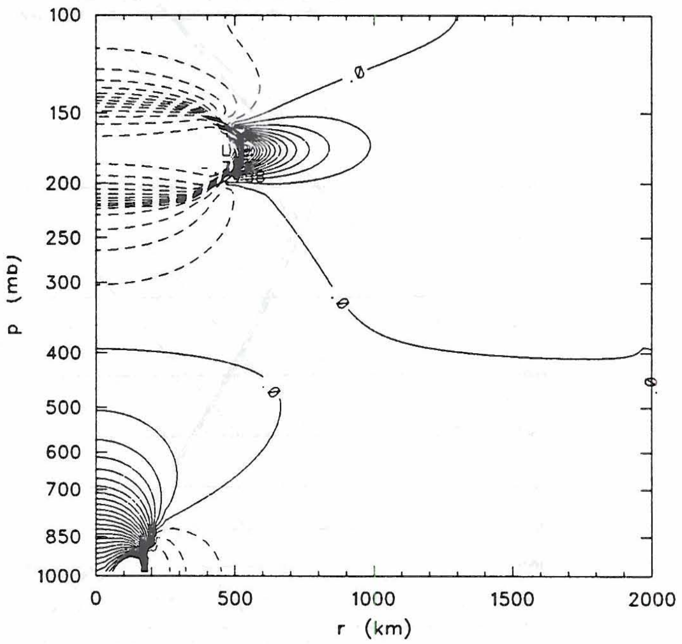

Figure 4.8: Control simulation isentropic relative vorticity ζ following the adjustment (5.0×10^{-6} s^{-1} contour interval).

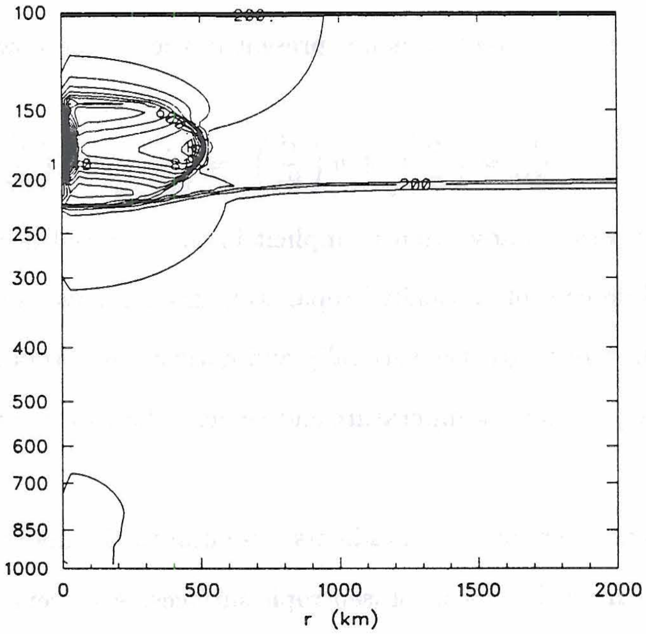

Figure 4.9: Control simulation aspect ratio λ'/H' (contour interval is 50).

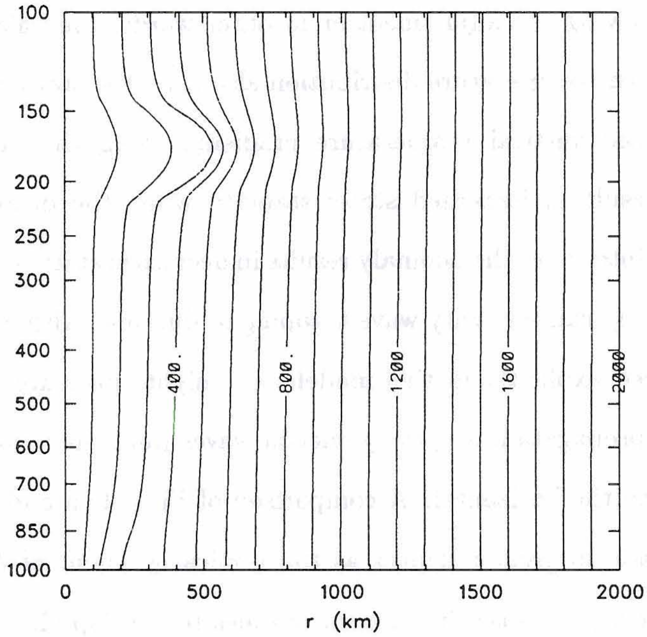

Figure 4.10: Control simulation potential radius R following the adjustment (100 km contour interval). Contours represent surfaces of constant angular momentum. Notice that the upper displacements are much greater than those at the surface.

Unbalanced vertical pressure gradients produced by the mass perturbation generate vertically–propagating gravity waves. It would appear from the governing equations (3.4)–(3.8) that vertical advection is not present in the model; however, recognizing that

$$\frac{D}{Dt} = \left(\frac{\partial}{\partial t}\right)_\theta + u\left(\frac{\partial}{\partial r}\right)_\theta = \left(\frac{\partial}{\partial t}\right)_p + u\left(\frac{\partial}{\partial r}\right)_p + \omega\frac{\partial}{\partial p}, \tag{4.1}$$

we see that vertical advection is implicit in the material derivative. Thus, the adiabatic ascent and descent of vertically propagating gravity waves produces a warm–cold couplet (Fig. 4.6b). Amazingly, the vertically and horizontally propagating gravity waves work in harmony to produce a temperature and velocity distribution that maintains thermal wind balance.

Horizontal temperature gradients, essential to the maintenance of thermal wind balance, result from the *bowing* of isentropic surfaces. Apparent in the isentropes of Fig. 4.6a is a lens structure similar to that obtained by Gill (1981) and Shutts et al. (1988) (Figs. 2.8 and 2.9b). In terms of energy, the lens represent the fraction of APE_0 remaining in the system following the adjustment or in other words, the balanced APE. Notice that the changes in the temperature distribution also alter the static stability (Fig. 4.7).

Increased vertical temperature gradients along the horizontal boundaries of the anomaly result in increased static stability while the decreased temperature gradient within the interior of the anomaly results in decreased static stability. Large static stability gradients may cause gravity wave trapping or ducting. Although the transient adjustment is not solved explicitly in this model, one might speculate that as the peaks in N develop, the propagation of gravity–inertia waves (and the adjustment) will be increasingly restricted to the horizontal. A comparison of Figs. 4.6a and 4.7a shows that the adjustment spreads to greater depths as the vertical gradient of N weakens. Restricting the adjustment depth causes intense shear zones to develop above and below the anomaly.

Strong shear is also produced in the horizontal as shown in the distribution of isentropic relative vorticity ζ (Fig. 4.8). A strong gradient of cyclonic vorticity is found along the outer edge of the anomaly. In contrast, the interior is dominated by nearly constant anticyclonic vorticity. This structure agrees well with both Gill's (1981) and Shutts et al.'s (1988) results (Figs. 2.8 and 2.9). Along the outer edge of the perturbation, the flow is becoming more inertially stable while the interior is becoming less inertially stable. Radial displacements are inhibited by the inertial stability such that the largest displacements or strongest adjustment is experienced by parcels within the interior of the perturbation (Fig. 4.10).

Recall that Gill (1981) and Shutts et al.'s (1988) linear formulations showed that the aspect ratio of the lens is given by $\lambda/H = N/f$. In regions were N varies significantly from that of the basic state or ζ becomes large in comparison to f, the aspect ratio is more accurately represented by the rotational form $\lambda'/H' = N(r,s)/\sqrt{(\zeta+f)\left(\frac{2v}{r}+f\right)}$. Fig. 4.9 shows that most of the domain, except for the interior of the anomaly, is dominated by λ/H which for the stratosphere is approximately 200. Decreased inertial stability within the interior of the perturbation causes a four fold increase in the aspect ratio ($\lambda'/H' \approx 800$). Thus, for a given value of H', λ' increases within the interior resulting in a shift of the adjustment from the velocity to the mass field (Schubert et al., 1980).

At the surface, gravity–inertia waves transport mass inward to fill the void left by the mass sink; however, Fig. 4.10 indicates that lateral displacements are minimal (in comparison to the upper perturbation). As pointed out by Shutts et al. (1988), radial inflow is limited by the conservation of angular momentum. If the flow was allowed to converge onto the axis, conservation of angular momentum would produce an infinite tangential velocity; consequently, to fill the sink, mass must also descend (Fig. 2.9c). Adiabatically descending gravity waves produce the warm core low (Fig. 4.6a and b) and sloping "eye wall" frontal structure (Fig. 4.5) observed by Shutts et al. (1988).

4.2.3 Comparison to Observations

At this point, we can compare the results of the model to the observations presented in Chapter 2 and discuss the validity of the model physics. First, consider the similarities between the model–derived wind field (Fig. 4.6a) and the perturbation wind fields obtained by FM (Fig. 2.1–Fig. 2.4). The simulated anticyclone has a minimum velocity of -13.5 ms^{-1} at 500 km which is approximately a third less than the analyzed 20 ms^{-1}. Two factors contribute to this difference. First, the latitudes of the systems studied by FM were 5°–10°

farther north than the 30° used in the simulation. As will be shown in a later section, increasing latitude increases the strength of the balanced circulation. Second, the amount of forcing may be stronger in the observational studies. Recall that the model's forcing is limited by the amount of mass initially available in the basic state. If the model were time dependent, mass could be supplied continuously resulting in greater forcing and stronger balanced circulations. At the surface, a warm core cyclone develops with a maximum velocity of 11.5 ms^{-1} at 156 km. CLMT's analysis does show the development of cyclonic vorticity at the surface prior to and during the systems formation; however, the mesoscale cyclone which develops in the model has more in common with oceanic systems such as polar lows (Rasmussen, 1985; Shapiro et al., 1987) and tropical cyclones (Shea and Gray, 1973) than it does with those systems observed over land. More detailed simulation including the effects of downdrafts are needed to fully understand the mid–tropospheric and surface features analyzed by CLMT.

Interesting similarities between the model results and observations can also be seen in the adjusted temperature profile (Fig. 4.6b), and the soundings at LCH and JAN (Fig. 2.7). The warm–cold couplet produced by the lens has a vertical structure that is nearly identical to the temperature distributions in the soundings. Model warm and cold anomalies are 5.3°C and 4.2°C, respectively, as compared to the 2–3°C and 13°C of the soundings. Recall that FM observed a 1–2°C warm anomaly and a 6–8°C cold anomaly. Evidently, the model warming is too strong while the model cooling is much too weak. The discrepancies can be partially accounted for as follows.

Recall from Fig. 4.3 that the nonhydrostatic pressure increase, caused by the initial mass perturbation, generates a deep layer of warm air. A remnant of this effect is present in the warm anomaly. Since the actual transient vertical motions which generate the mass perturbation are nonhydrostatic, it is believed that this hydrostatic effect is an artifact of the model and not an actual physical process; consequently, the magnitude of the warm pool is overestimated by approximately 1–2°C.

Discrepancies in the cold anomaly, on the other hand, are caused by the lack of additional cooling atop the perturbation produced by entrainment and radiative processes not included in the model. The impact of these processes will be considered in later sensitivity studies. Entrainment and turbulent mixing also impact the temperature gradient within the injection.

Notice that the observed adiabatic gradient within the anvil at LCH is not reproduced. Since the model flow is hydrostatic, turbulent motions are not generated; thus, the observed homogeneous layer is not reproduced. The model does, however, form the sharp inversions that are observed above and below the injection.

Interestingly, the double inversion structure is dynamically linked to the σ^* field. Inversions or gradients in static stability are associated with gradients in σ^*. Fig. 4.5 shows that the inversion splits at the perturbation. One branch represents the depressed tropopause while the other is formed by the cold pool atop the lens. Several sensitivity studies will now be examined to determine the impact of varying the perturbation parameters in Table 4.1. The forcing parameters $\hat{\sigma}$ and r_2 will be considered first.

4.3 Comparing the Control to Sensitivity Simulations

4.3.1 Forcing Changes

Fig. 4.11 shows the relationship between $\hat{\sigma}$ and the percentage of mass removed and injected within two perturbation radii r_2. In the forcing diagrams that follow, $\hat{\sigma}$ will be shown on the bottom of the figures and the percentage of mass removed along the top. In addition, the control simulation is identified by the blackened data points. Fig. 4.12 illustrates the effect of varying $\hat{\sigma}$ on the velocity extremes and the parcel displacements necessary to produce those extremes.

As one might expect, increases in forcing produce stronger vortices; however, not as obvious are the nonlinear growth rates. When $\hat{\sigma} = 0.5$, the anticyclone is four times stronger than the cyclone; whereas, when $\hat{\sigma} = 3.6$, the anticyclone strength has decreased to 1.2 that of the cyclone. It appears that the anticyclone growth approaches a linear limit while the cyclone growth continues to accelerate. This is again consistent with angular momentum conservation. When $\hat{\sigma} \approx 4$, the magnitudes of the vortices are identical;

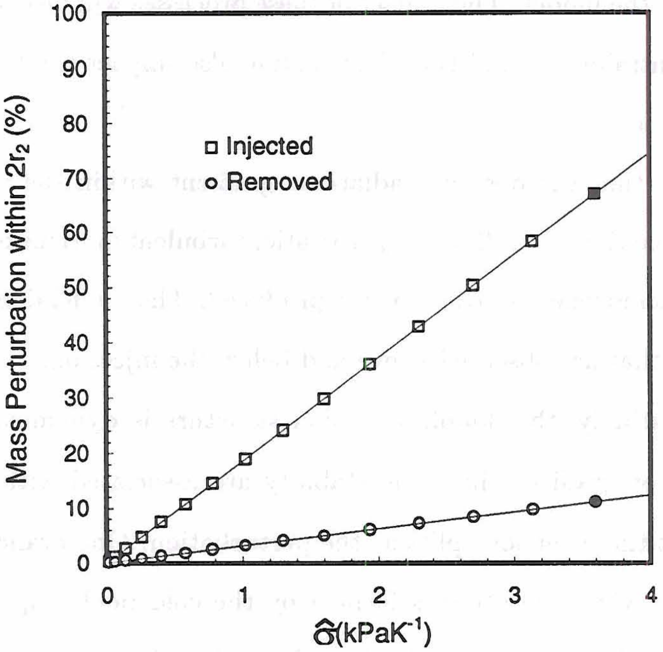

Figure 4.11: Relationship between the perturbation amplitude $\hat{\sigma}$ and the percentage of mass removed from a cylinder of radius $2r_2$, bounded by the surface and s_1. The blackened data points indicate the values used in the control simulation.

however, the parcel displacements are not. The displacement of the velocity maximum is only about half that of the minimum.

Likewise, forcing increases produce more energetic vortices (Fig. 4.13a). Notice that the APE_0 is an order of magnitude greater than the balanced APE and KE, indicating significant gravity–inertia wave generation. When the forcing is weak, about 5.8% of the APE_0 is retained and another 9% is converted into balanced KE (Fig. 4.13b). The remaining 85.2% radiates beyond the domain as gravity–inertia waves during the transient adjustment. Apparently, nonlinearities also affect the partitioning of the energetics. As the forcing is increased, the fraction of the APE remaining decreases to 4.2% while the fraction converted to balanced KE decreases to 8%. Forcing increases decrease the inertial stability of the system and reduce the efficiency of the adjustment such that less disturbance energy is partitioned to the balanced state of the system.

Increases in r_2 also impact the amount of mass forcing. Variations in r_2 are equivalent to changes in the size of the convective system. Below about 200 km radius, the cyclone is

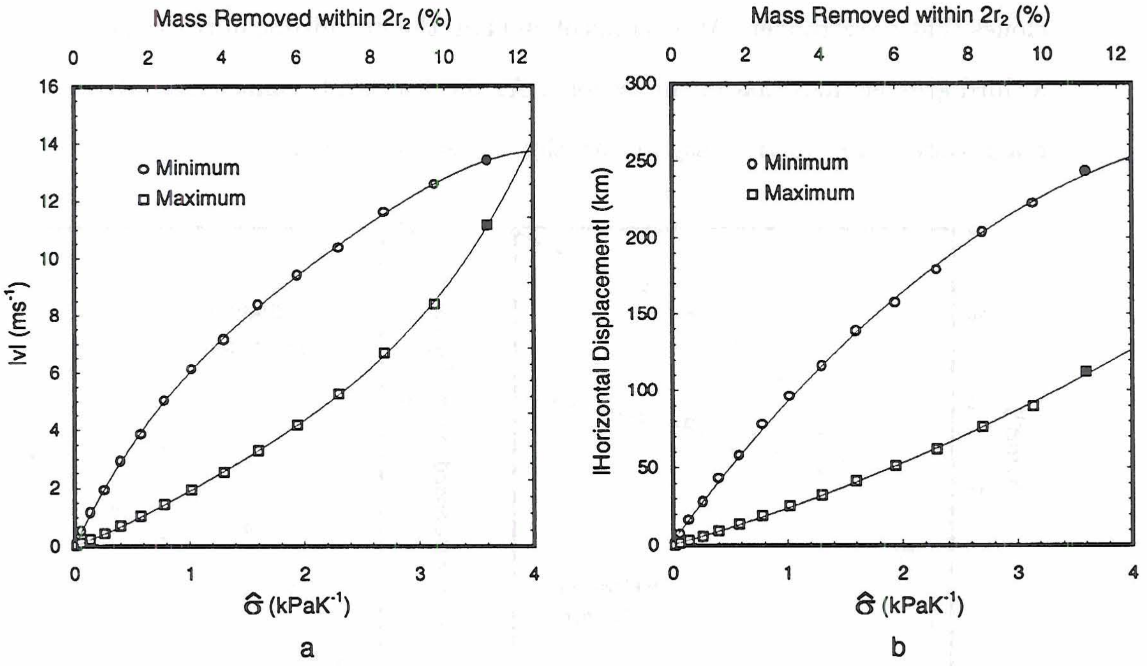

Figure 4.12: Variation of the (a) velocity extremes and the (b) radial displacements needed to produce the velocity extremes in relation to the forcing. The blackened data points are the same as in Fig. 4.11.

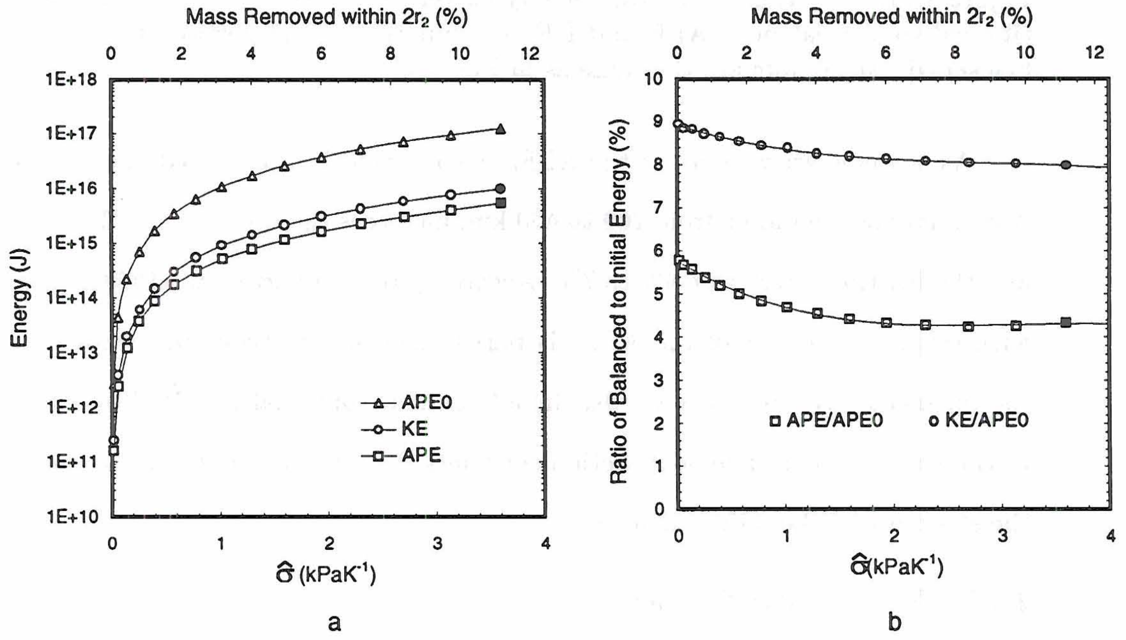

Figure 4.13: Relationship between the energetics and the forcing including the (a) integrated APE_0, APE, and KE; and the (b) percentage of APE_0 partitioned to the balanced APE and KE. The blackened data points are the same as in Fig. 4.11.

stronger than the anticyclone (Fig. 4.14a); whereas, larger scale systems produce anticyclones that are stronger. At a radius of 600 km, the magnitude of the anticyclone is nearly a third greater than that of the cyclone. As the systems become smaller than 100 km, the magnitude of the vortices asymptotically decreases to zero.

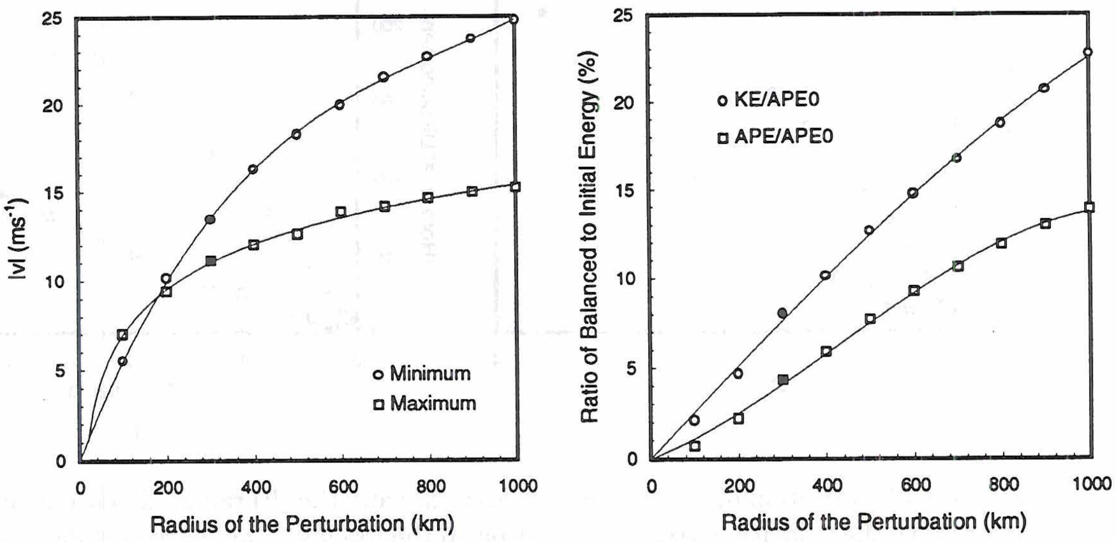

a

b

Figure 4.14: Variation of the (a) velocity extremes and the (b) percentage of APE_0 partitioned to the balanced APE and KE as a function of the perturbation radius r_2. The blackened data points are the same as in Fig. 4.11.

As systems grow, more of the APE_0 is converted into balanced energy (Fig. 4.14b). A doubling of the radius from 200 to 400 km, increases the fractional APE from 2% to 6% and the fractional KE from 4% to 7%. According to Schubert et al. (1980), as r_2 increases with respect to λ, less of the APE_0 is partitioned to gravity–inertia waves and more to the balanced flow. In other words, the adjustment continually shifts from the mass field to the velocity field. The next section considers the impact of changing static stability on the structure of the adjusted state.

4.3.2 Static Stability Changes

If the updraft fails to penetrate into the stratosphere, the outflow will come to rest below the tropopause. Fig. 4.15 shows the adjusted state of a simulation that is identical to the control except that the 50 mb perturbation is now located immediately beneath the tropopause.

Overall, the balanced state of the system weakens relative to the control. The anticyclone magnitude has decreased by 27% to -9.87 ms^{-1} with an 80 km decrease in radial extent to 420 km. Also, there is a 3°C reduction in the cold anomaly and a 2.5°C reduction in the warm anomaly. In contrast to the control, the tropopause is forced upward with no secondary temperature minimum. By maintaining a 50 mb perturbation depth, the mass forcing is identical to the control simulation; therefore, the variations can only be due to the change in static stability incurred by moving the injection from the stratosphere to the troposphere.

Variations in static stability are measured in terms of the Brunt Väisälä or buoyancy frequency $N = \sqrt{\rho g^2/\sigma c_p}$. Fig. 4.16b indicates that the basic state N is nearly constant in both the troposphere and stratosphere with a large discontinuity at the tropopause. The phase speed c_n of an internal gravity wave within a continuously stratified fluid is proportional to N. Thus, as the static stability decreases, gravity–inertia waves propagate more slowly and the adjustment occurs over shorter horizontal scales (i.e., $\lambda = c_n/f$ decreases; compare Figs. 4.10 and 4.19). In addition, according to angular momentum conservation, the balanced flow will be weaker since the horizontal displacements are smaller. Recall that the aspect ratio is also proportional to N.

In this case, λ'/H' is approximately 200 which is about double that of the troposphere ($\lambda/H \approx 100$). Thus, for a given H', the decreased N within the troposphere results in a λ' which is smaller than that of the control simulation. Large values of λ'/H' atop the anomaly show the influence of increased static stability above the tropopause. Understanding the impact of N on the adjustment is further clarified by considering the changes in the balanced state that result from gradually moving the perturbation through the tropopause.

As the perturbation comes into contact with the tropopause and the increased static stability of the stratosphere above, the anticyclone magnitude rapidly increases from 9 to 15 ms^{-1} (Fig. 4.20a). For vertical separations greater than H, between the perturbation

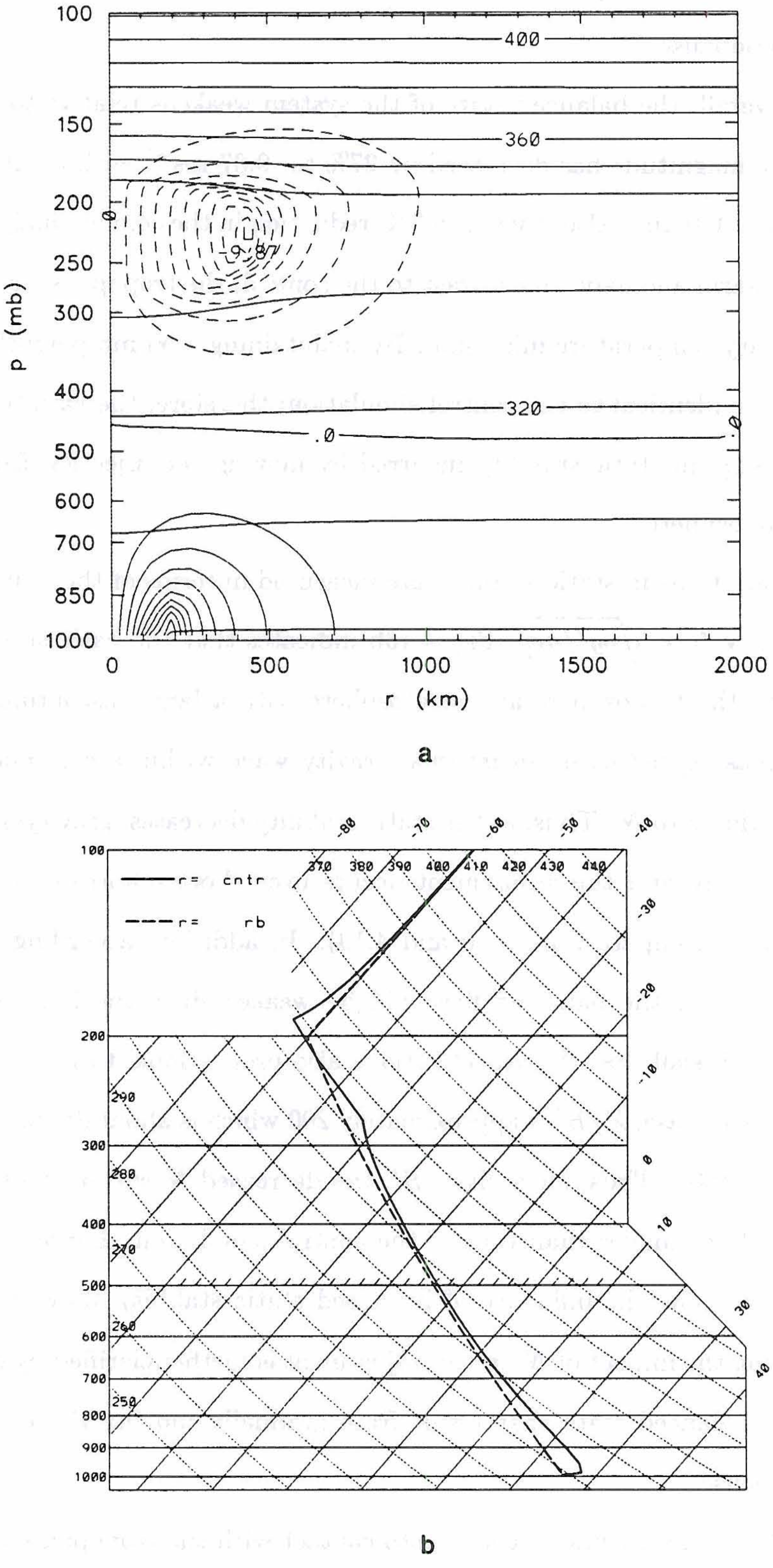

Figure 4.15: Same as Fig. 4.6 except that the 50 mb perturbation is located immediately beneath the tropopause.

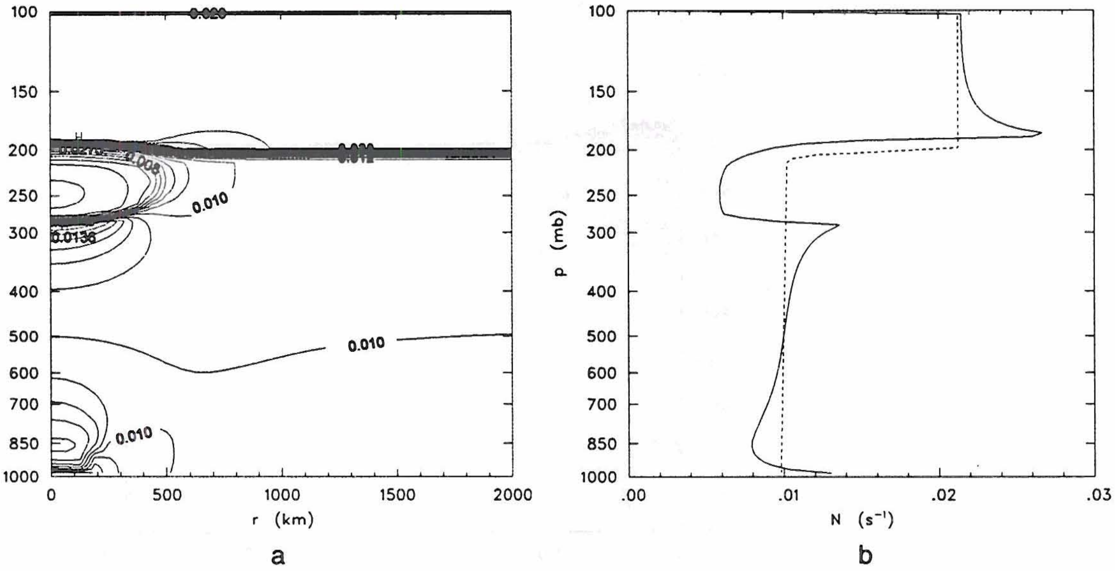

Figure 4.16: Same as Fig. 4.7 except that the 50 mb perturbation is located immediately beneath the tropopause.

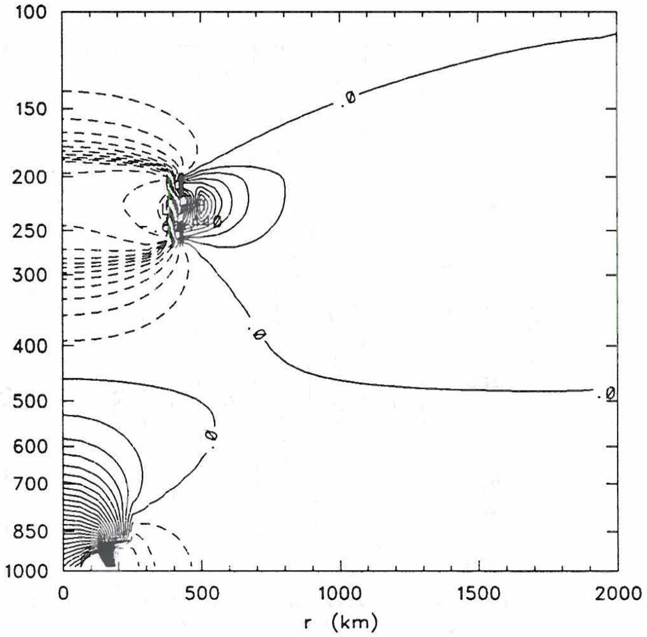

Figure 4.17: Same as Fig. 4.8 except that the 50 mb perturbation is located immediately beneath the tropopause.

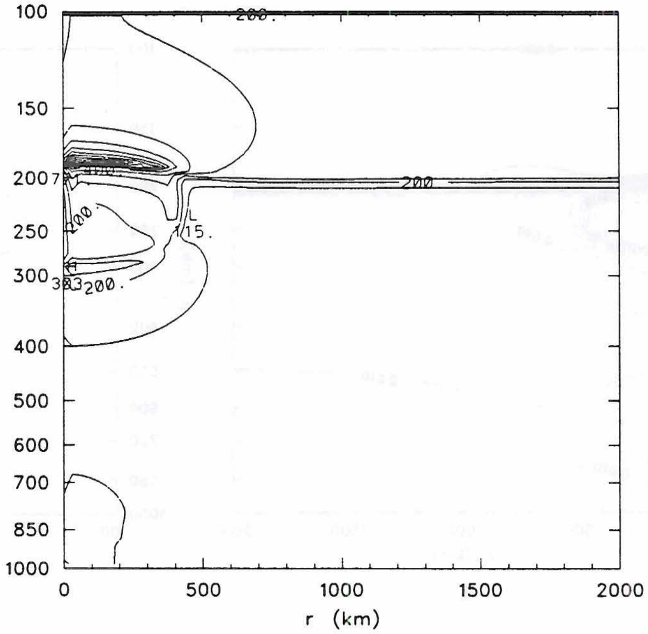

Figure 4.18: Same as Fig. 4.9 except that the 50 mb perturbation is located immediately beneath the tropopause.

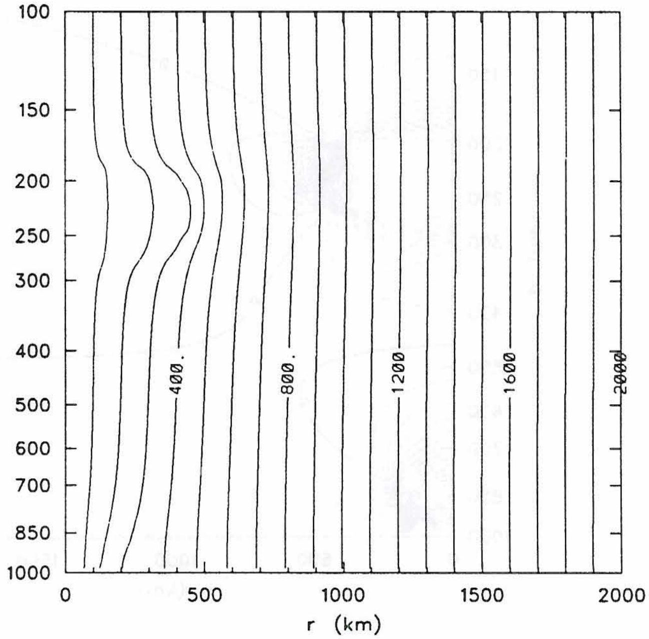

Figure 4.19: Same as Fig. 4.10 except that the 50 mb perturbation is located immediately beneath the tropopause.

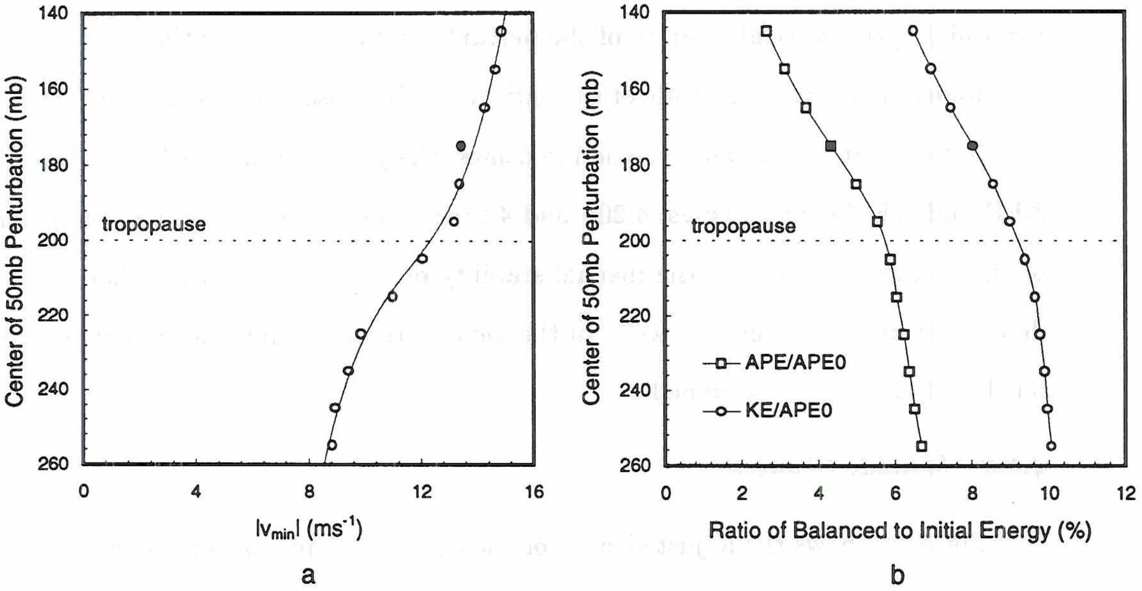

Figure 4.20: Variation of the (a) minimum velocity and the (b) percentage of APE_0 partitioned to the balanced APE and KE as a function of the perturbation's vertical placement. The blackened data points are the same as in Fig. 4.11.

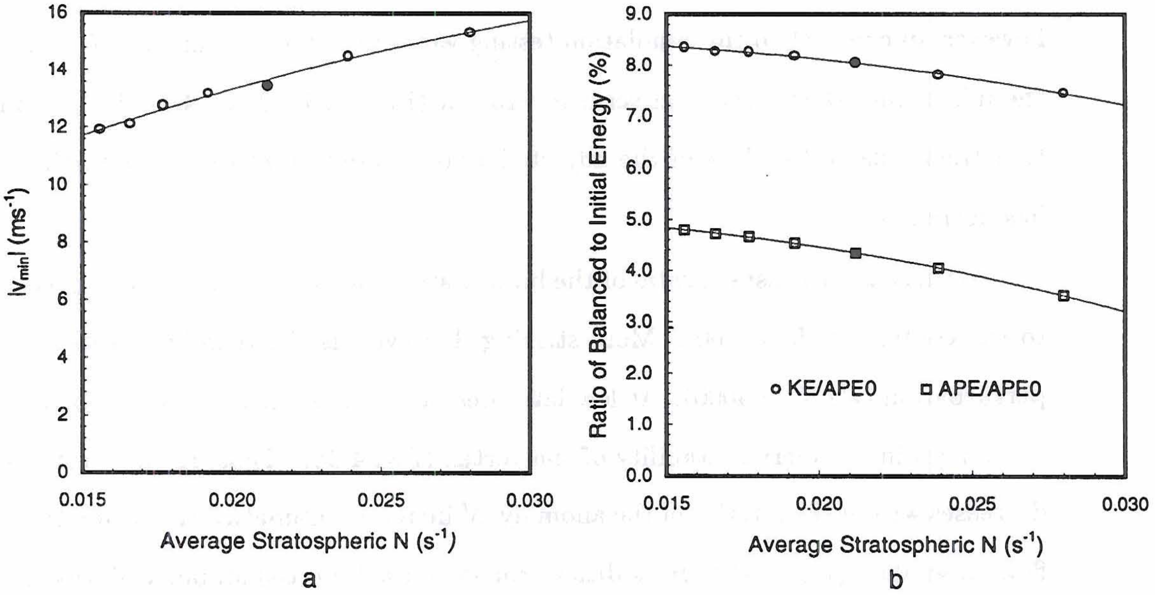

Figure 4.21: Variation of the (a) minimum velocity and the (b) percentage of APE_0 partitioned to the balanced APE and KE as a function of the average stratospheric static stability N. The blackened data points are the same as in Fig. 4.11.

and the tropopause, the magnitude of the anticyclone as a function of altitude becomes a constant. An alternate method to test the influence of N on the adjustment involves maintaining the vertical position of the perturbation while varying the basic state N. For a doubling of N, the magnitude of the anticyclone increases by about 4 ms^{-1} (Fig. 4.21a).

Notice that, as the anticyclone intensifies, the partitioning of APE_0 to the balanced APE and KE decreases (Figs. 4.20b and 4.21b). This again shows that the partitioning of the energy is related to the inertial stability of the system. Recall that λ is not only dependent on N but on f as well. In the next section, the influence of changing latitude on the adjustment is examined.

4.3.3 Latitude Changes

Fig. 4.22 shows the adjusted state of a simulation identical to the control except that the perturbation has been displaced south to 10°N. Again, as in the previous simulation, the adjusted state is weaker than the control. The cold and warm temperature anomalies have decreased by 5.5 and 3°C, respectively, but with the same overall vertical structure. In addition, the magnitude of the anticyclone has diminished by over a half to -6.63 ms^{-1}; however, in contrast to the simulation testing variability due to changing N, the radius of the minimum velocity has increased to 615 km (Fig. 4.26). Figs. 4.22–4.26 clearly show that the horizontal scale λ of the adjusted state has increased while the vertical scale H has decreased.

In this case, the aspect ratio of the basic state stratosphere has doubled in comparison to the control ($\lambda/H \approx 400$). More striking, however, is the tenfold increase within the perturbation ($\lambda'/H' \approx 4000$). At low latitudes, where f is small, λ' is extremely sensitive to changes in the inertial stability of the vortex (Fig. 4.24). Thus, as the inertial stability decreases within the interior of the anomaly, λ' increases dramatically causing the adjusted flow to weaken (Fig. 4.22). In addition, the decreased inertial stability allows for greater horizontal displacements of adjusting parcels (Fig. 4.26).

Several sensitivity simulations have been conducted to study the impact of changing f on the kinematics and energetics of the system. Fig. 4.27a shows that the influence of f is greatest where $\beta = \partial f/\partial \phi$ is large. A 20° change in latitude within the subtropics results

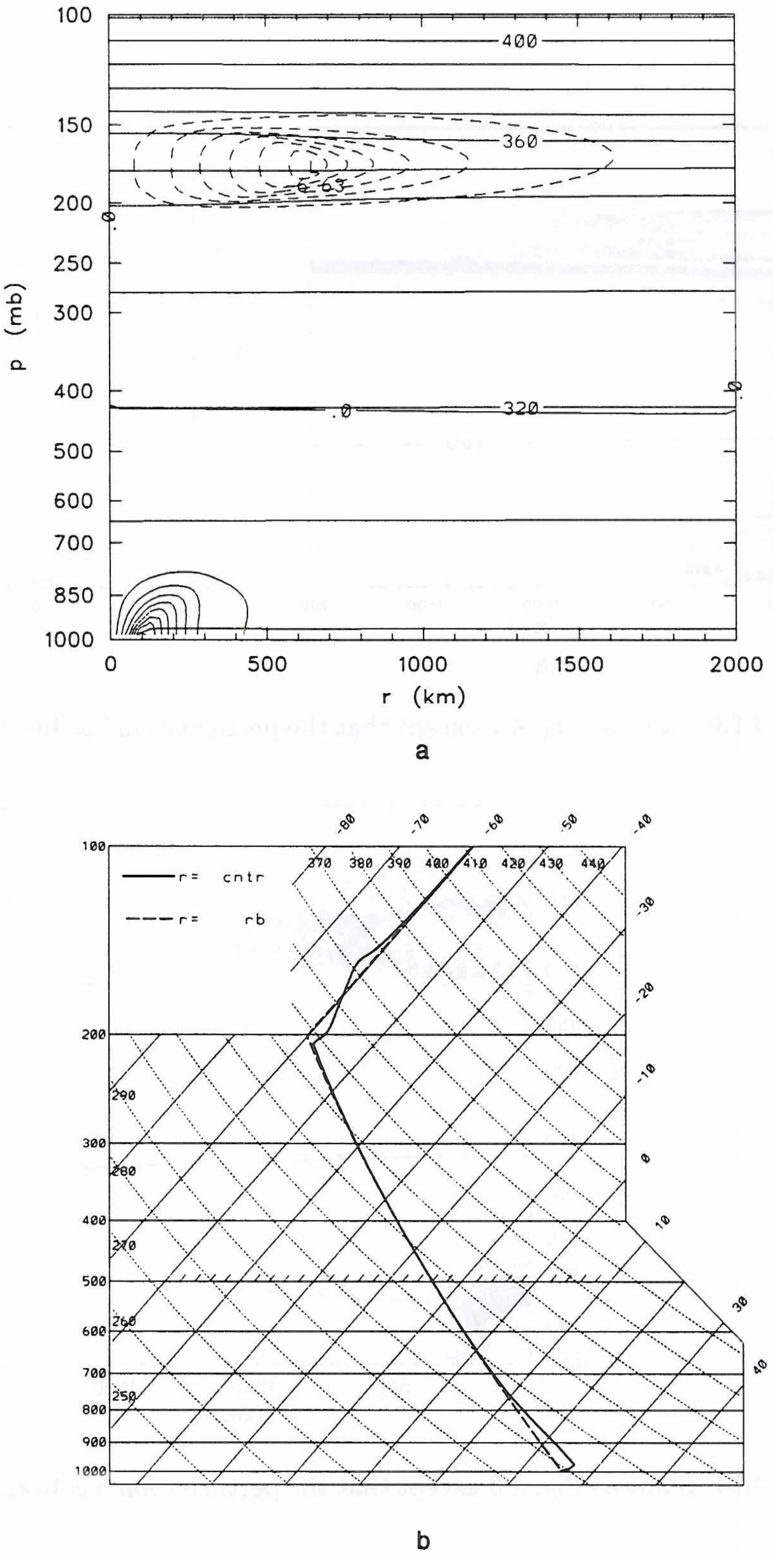

Figure 4.22: Same as Fig. 4.6 except that the perturbation has been moved south to 10°N.

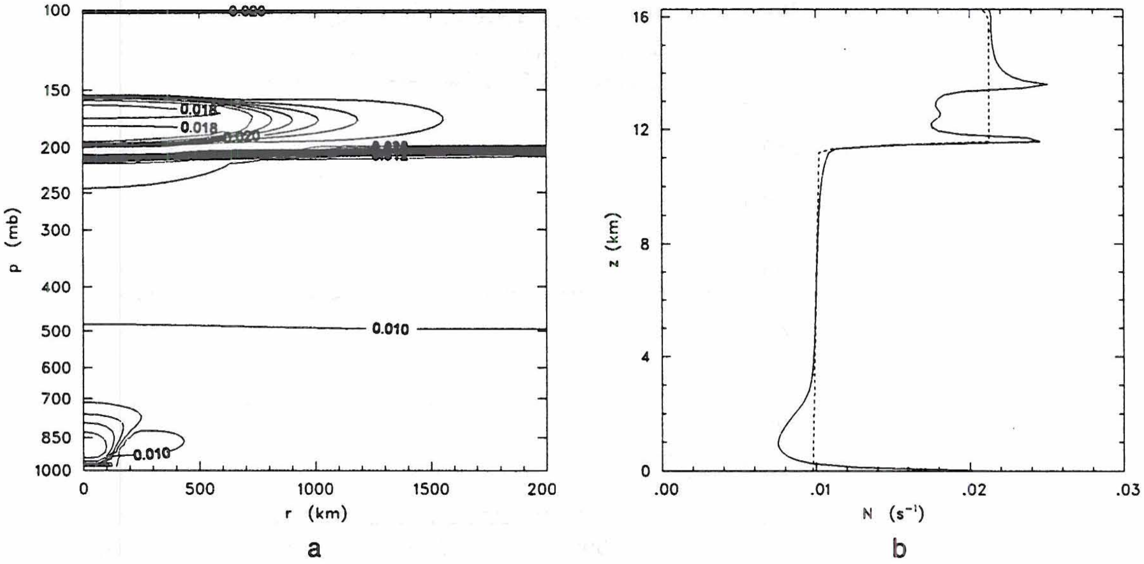

Figure 4.23: Same as Fig. 4.7 except that the perturbation has been moved south to 10°N.

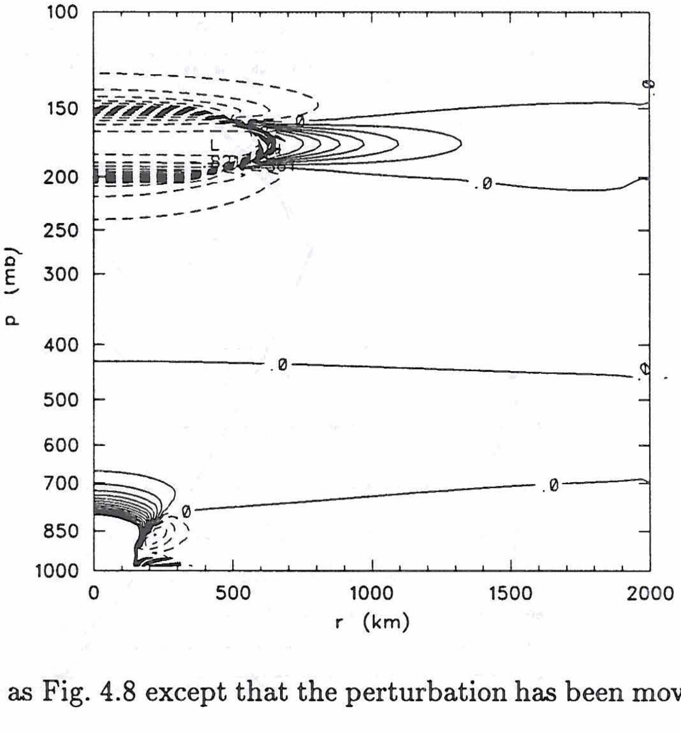

Figure 4.24: Same as Fig. 4.8 except that the perturbation has been moved south to 10°N.

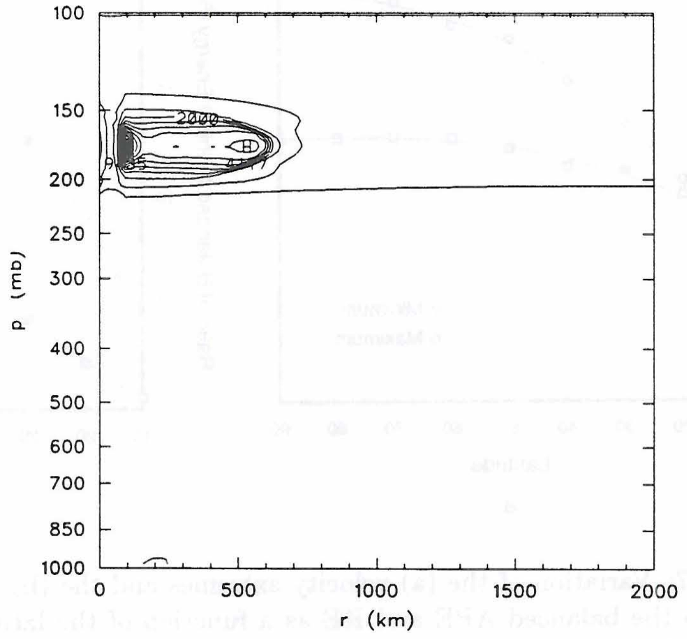

Figure 4.25: Same as Fig. 4.9 except that the perturbation has been moved south to 10°N (contour interval is 500).

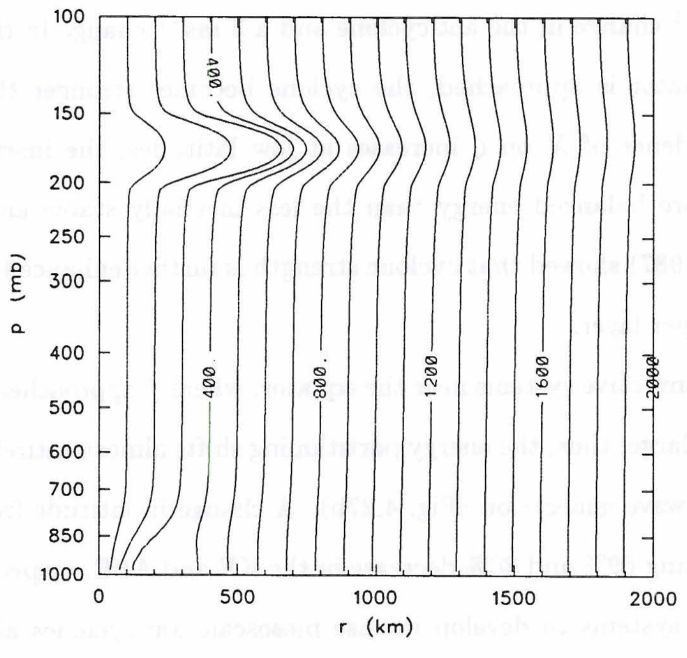

Figure 4.26: Same as Fig. 4.10 except that the perturbation has been moved south to 10°N.

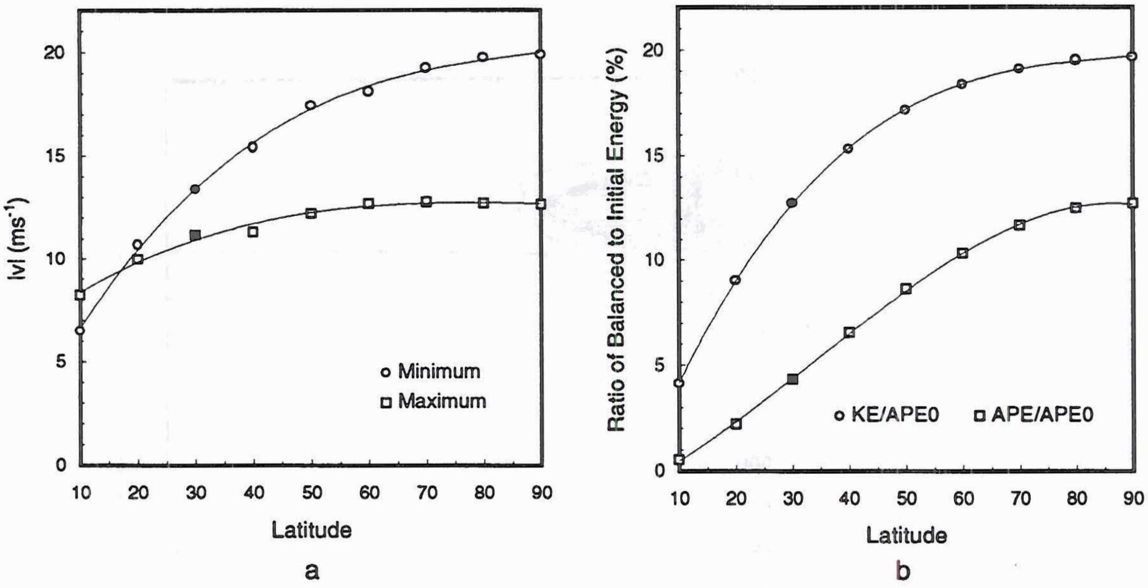

Figure 4.27: Variation of the (a) velocity extremes and the (b) percentage of APE_0 partitioned to the balanced APE and KE as a function of the latitude. The curves do not extend to the equator due to the limitations of the f-plane approximation. Note that APE_0 is not a function of latitude, but has a constant value 1.23×10^{17}J. The blackened data points are the same as in Fig. 4.11.

in a 7 ms^{-1} change in the anticyclone and a 3 ms^{-1} change in the cyclone. Interestingly, as the equator is approached, the cyclone becomes stronger than the anticyclone. As the dependence of λ' on ζ increases at low latitudes, the inertially stable cyclone will receive more balanced energy than the less inertially stable anticyclone. Schubert and Alworth (1987) showed that cyclone strength is further enhanced if the mass source occurs over a deeper layer.

For convective systems near the equator, where f approaches zero, values of λ become extremely large; thus, the energy partitioning shifts almost entirely from the balanced flow to gravity wave generation (Fig. 4.27b). A change in latitude from 30°N to 10°N results in an amazing 69% and 80% decrease in the KE and APE, respectively. Thus, for tropical convective systems to develop intense mesoscale anticyclones aloft, they must be much larger than their mid-latitude counterparts. Earlier in the chapter, it was pointed out that the cold anomaly is much too weak. We return to this subject and consider the moderating effects of entrainment and radiation.

4.4 Considering the Effects of Entrainment and Radiation

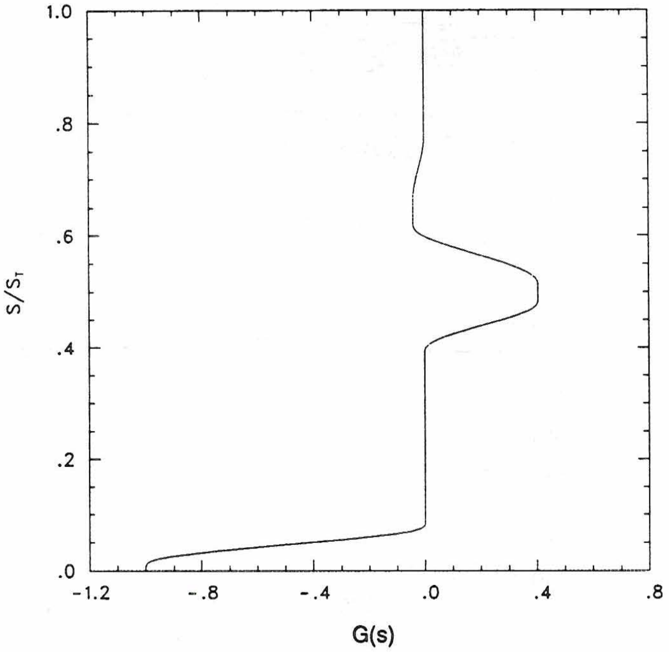

Figure 4.28: Profile of $G(s)$ including an additional mass sink along the top of the outflow.

Probably the most significant discrepancy between the model results and the observational data is the large difference in the magnitude of the cold anomaly. It appears that one or more additional diabatic processes are affecting the cloud–top temperature. The most likely candidate would be longwave radiative cooling; however, as pointed out in Chapter 2, the downward flux of heat from the stratosphere by entrainment is also important. For example, Shutts and Gray's (1994) plume model produces a small region of cloud–top cooling in the absence of radiative cooling. They suggest that the "existence of such a cool layer is consistent with a small net mass sink created by the entrainment of air into the convective plume during its overshoot phase." Recall from the model formulation that provisions were made in the vertical perturbation profile $G(s)$ to add an additional mass sink at the top of the injection.

Such a sink will, in a manner similar to the method used by Fritsch and Brown (1982), reproduce the diabatic cooling that occurs at cloud top. By choosing $\epsilon \neq 0$, a small amount of mass is removed from the layer above and drawn down into the injection. Choosing $\epsilon = 0.1$ produces the maximum possible perturbation. A perturbation top of $s_5 = 0.64$

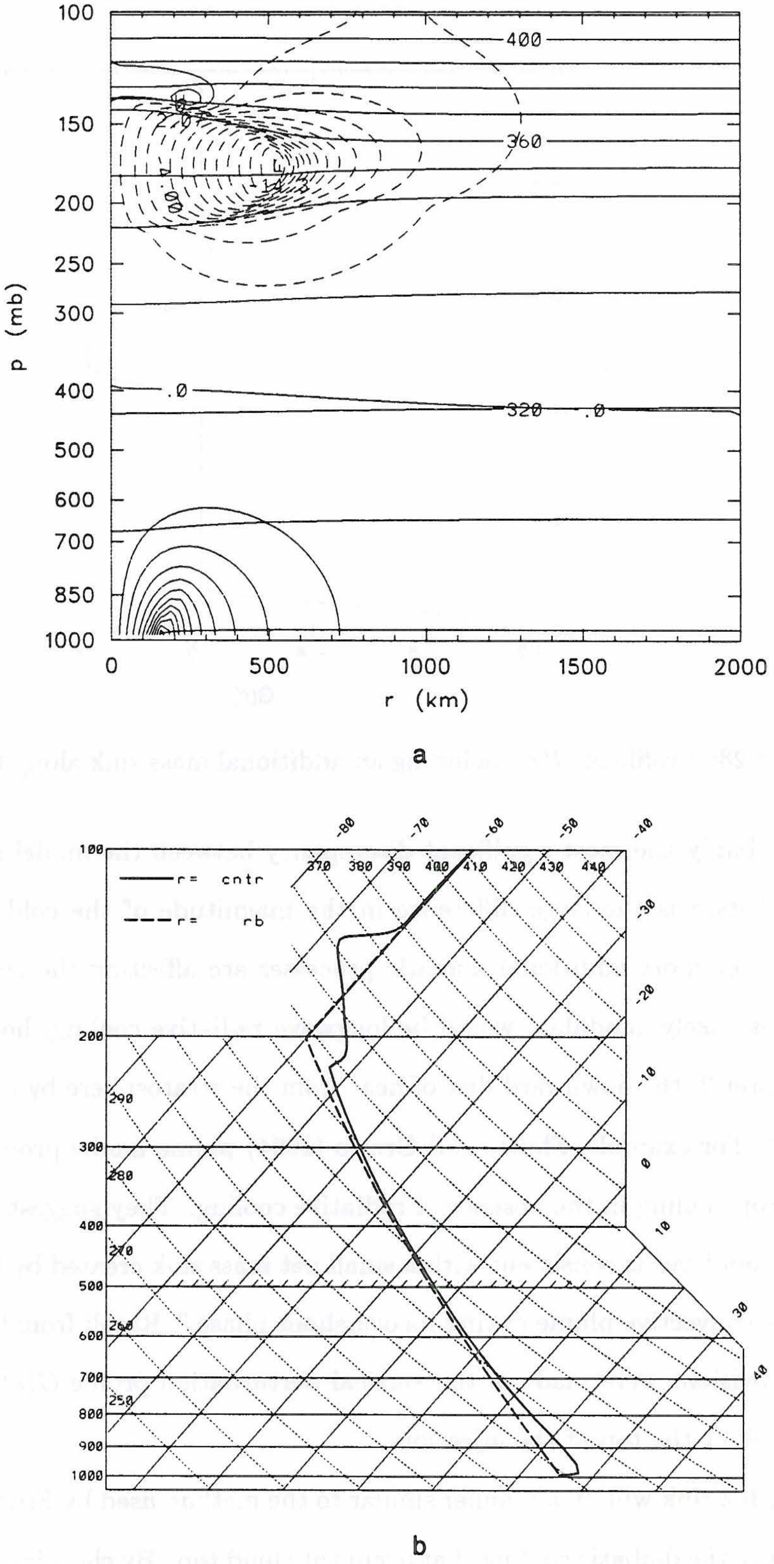

Figure 4.29: Same as Fig. 4.6 except that a mass sink immediately above the injection has been introduced to simulate the effects of entrainment and radiational cooling.

(125 mb) yields an entrainment depth of 1.4 km which is consistent with the penetration depth of an entraining, overshooting cloud–top. The modified perturbation profile is shown in Fig. 4.28.

Keep in mind that the perturbation depth is decreased in comparison to the control profile, causing the mass forcing to increase from 67% to 85%. Thus, cloud–top diabatic effects not only affect the cold anomaly but the gradient adjustment process as well. The adjusted state of this simulation is shown in Fig. 4.29.

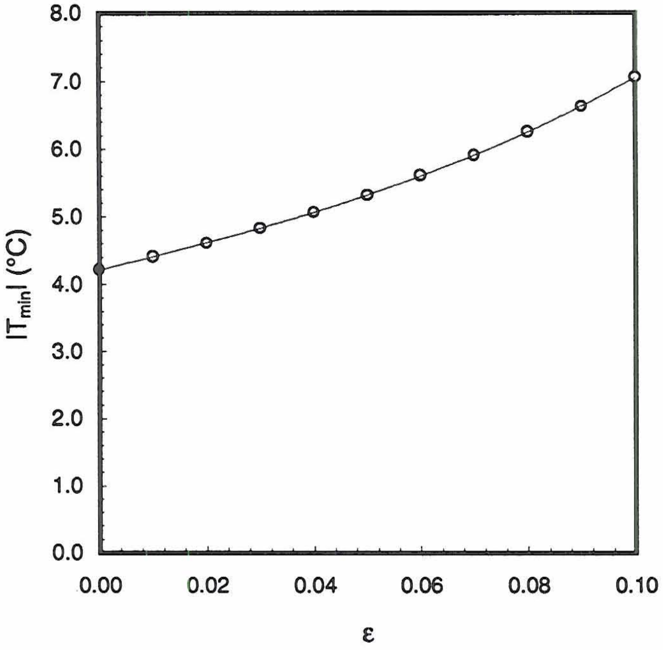

Figure 4.30: Variation of the cold pool temperature as the magnitude of the cloud–top mass sink ϵ is increased. The blackened data point are the same as in Fig. 4.11.

The decreased depth of the perturbation along with the increased mass forcing has strengthened the anticyclone, in comparison to the control, by 0.8 ms^{-1}. Note also that a shallow cyclonic lens, with a magnitude less than 2 ms^{-1}, forms above the anticyclone. Shutts and Gray's (1994) plume simulations produce a similar vortex. Cyclonic motion, associated with the vertical advection of cyclonic momentum, is observed near the center of hurricane outflow; however, similar features have not been observed in the outflow of MCSs. This simulation suggests that cyclonic vorticity may be generated within the outflow through diabatic cooling and gradient adjustment. Keep in mind that the forcing used to simulate the cooling is extremely simplified. In reality, the radius of the entraining updraft is much less than r_2 while the radiative cooling occurs over a depth much shallower than $s_5 - s_4$.

Fig. 4.30 shows the magnitude of the cold pool as a function of ϵ. The cold pool temperature does decrease by an additional 2.5°C; however, the resulting temperature anomaly remains much less than that observed by BN, suggesting that even stronger forcing is present. No change is observed in the magnitude of the warm anomaly.

Chapter 5

SUMMARY AND CONCLUSIONS

5.1 Summary

After examining the observational data of mesoscale convection presented in Chapter 2, the assertion was made that the anticyclonic outflow within the upper–troposphere and lower–stratosphere can be partially explained by the gradient adjustment of the disturbed mass field. To verify this hypothesis, a nonlinear balanced model was developed in Chapter 3 from the axisymmetric, quasi–static primitive equations to examine the gradient balanced state of a hypothetical convective system. Specifically, we idealized the convection as an impulsive transfer of mass from the lower-troposphere to a layer near the tropopause within a continuously stratified environment. Using isentropic and transformed radius (Schubert and Hack, 1983) coordinates, we obtained an analytic solution similar to the classic Rossby invertibility problem. Numerical simulations were conducted in Chapter 4 to verify the model's physics and to test the model's sensitivity to the mass forcing, static stability, latitude, and cloud–top diabatic forcing. Several conclusions can be drawn from the results of the numerical simulations.

5.2 Conclusions

1) In general, the results of the control simulation suggest that the formation of the observed anticyclone can be explained by the gradient adjustment of the convectively disturbed mass field. The model produces an anticyclone with accompanying thermal structure that is similar in magnitude and form to that observed by FM and BN.

2) Other diabatic effects alter the adjustment. When cloud–top cooling (i.e., entrainment, radiation, etc.) is included, the magnitudes of both the anticyclone and cold

temperature anomaly are increased. In addition, a weak cyclone forms in the region of cooling. Although this feature has not yet been observed it does appear in more complex numerical simulations (Shutts and Gray, 1994).

3) Lower–stratospheric injections produce a kinematic and thermodynamic structure that agrees with theory (Danielsen, 1982) and is similar to that observed (FM; Danielsen, 1982; and BN). In contrast, when the injection level is within the upper–troposphere, the magnitudes of the anticyclone and temperature anomalies are much weaker. In addition, no secondary temperature minimum is produced at the base of the outflow. Previous models have neglected the impact of the stratosphere resulting in the formation of anticyclones that are weaker and have less horizontal extent (Shutts et al. 1988; Shutts and Gray, 1994). The simulations presented here clearly show the importance of including a stratosphere in any study of deep, penetrative convection.

4) Large increases of static stability along the boundaries of the outflow may result in gravity wave ducting. Numerical simulations of a two–dimensional squall line conducted by Tripoli and Cotton (1989a, b) show that gravity wave trapping along the base of the outflow was enhanced when surface long–wave heating was included. It's possible that the heating enhances the inversion at the base of the outflow and increases the static stability.

5) Most of the initial available potential energy is partitioned to gravity–inertia oscillations. Only a fraction is partitioned to the balanced KE of the adjusted state. Schubert et al. (1980) demonstrated that the energy efficiency is dependent on λ, showing that "for small–scale initial disturbances in the pressure field most of the initial energy ends up in gravity–inertia waves." The amount of partitioning is still a matter of contention. Schubert et al.'s (1980) results show that it is less than 10% while Shutts and Gray (1994) have obtained values greater than 30%. The results of this study show that it is close to 8%. Future research is needed in this area to determine what individual factors influence the partitioning.

6) The efficiency of balanced energy generation decreases as the anticyclone intensifies. Using an Eliassen balanced vortex model to study tropical cyclones, Hack and Schubert (1986) found that the generation of balanced KE is a function of the inertial

stability of the vortex. Intensification of the anticyclone leads to reduced inertial stability and decreased balanced energy generation. Increased forcing would eventually cause the cyclone magnitude to surpass that of the anticyclone, resulting in the increased inertial stability of the system and greater efficiency of balanced energy generation.

5.3 Future Research

It is important to point out that this model represents a first approximation to the dynamic processes occurring within mesoscale convective outflows. Many important physical processes have been neglected in this formulation, not because they are unimportant, but because they limit our ability to find analytic solutions to the adjustment. Advancements in our understanding of the adjustment problem will come from increasingly more complex models which include the effects neglected here.

For instance, a clear limitation of this model is its lack of moisture. Moist processes must be included in future models to account for changes in the static stability (Lalas, D. P., and F. Einaudi, 1974; Durran and Klemp, 1982) and the temperature distribution within the outflow. The temperature profile is also affected by cloud–top entrainment and turbulent mixing within the layer. Furthermore, turbulence results in eddy diffusion which affects the shape of the perturbation lens (Gill et al.'s, 1979; Hedstrom and Armi, 1988). To simulate the turbulence, future models must be three-dimensional and nonhydrostatic. Differential radiative heating across the cloud layer further enhances turbulent mixing, requiring a radiative transfer model with accurate representations of cloud liquid and ice water contents (Starr and Cox, 1985a and b; Ackerman et al. 1988). Increased understanding of the energy partitioning dictates that future models account for the downscale cascade of energy and the transition to quasi-two dimensional turbulence (Lilly, 1988). To understand the instabilities present in these flows, asymmetries (Hedstrom and Armi, 1988) and vertical shear must be added (Shutts, 1987, 1994). Not only can an increased understanding of the adjustment process be gained from improved numerical models but from more detailed observational studies as well.

Doppler radar, wind profilers, and improved satellite imagery lend themselves to modern studies of the anticyclonic anomaly. This should include analysis similar to FM's to see what impact mesoscale convection has on current large–scale NWP models. Recall that in the introduction we asked the question: What errors do mesoscale convective outflows in the upper–troposphere and lower–stratosphere introduce into our large–scale NWP model forecasts?

Certainly, as this study shows, increasing the magnitude of the system will increase the error. However, for systems of similar size, the error introduced by the anticyclonic anomaly will be greatest at higher latitudes for those systems strong enough to inject mass into the stable layers of the lower stratosphere. Clearly the results of this and past studies indicate the need to increase our understanding of this process in order to improve future convective parameterization schemes.

REFERENCES

Ackerman T. P., K.-N. Liou, F. P. J. Valero and L. Pfister, 1988: Heating rates in tropical anvils. *J. Atmos. Sci.*, **45**, 1606–1623.

Adler, R. F., and D. D. Fenn, 1979: Thunderstorm vertical velocities estimated from satellite data. *J. Atmos. Sci.*, **36**, 1747–1754.

———, and R. A. Mack, 1986: Thunderstorm cloud top dynamics as inferred from satellite observations and a cloud top parcel model. *J. Atmos. Sci.*, **43**, 1945–1960.

———, M. J. Markus, A. J. Negri and G. P. Byrd, 1982: Estimating the temperature and height of overshooting thunderstorm tops from geostationary satellite infrared data. *Conf. on Cloud Phys.*, Chicago, Amer. Meteor. Soc., 500–503.

Armi, L. and W. Zenk, 1984: Large lenses of highly saline Mediterranean water. *J. Phys. Oceanogr.*, **14**, 1560–1576.

Ball, F. K., 1960: Control of inversion height by surface heating. *Quart. J. Roy. Meteor. Soc.*, **86**, 483–494.

Barnier, B., M. Crépon and C. Le Provost, 1989: Horizontal ocean circulation forced by deep–water formation. Part II: A quasi–geostrophic simulation. *J. Phys. Oceanogr.*, **19**, 1794–1808.

Biggerstaff, M. I., and R. A. Houze, Jr., 1991: Kinematic and precipitation structure of the 10–11 June 1985 squall line. *Mon. Wea. Rev.*, **119**, 3034–3065.

Bjerknes, V., 1898: Über die bildung von circulationsbewegungen and wirbeln in reibunglosen flüssigkeiten. *Skr. Nor. Vidensk.-Akad. [Kl.] 1: Mat.-Naturvidensk. Kl.*, **5**, 1–29.

Bosart, L. F., and J. W. Nielsen, 1993: Radiosonde penetration of an undilute cumulonimbus anvil. *Mon. Wea. Rev.*, **121**, 1688–1702.

Chen, S. S., 1990: A numerical study of the genesis of extratropical convective mesovortices. Ph.D. dissertation, Pennsylvania State University, University Park, 178 pp.

Chen, S., and W. R. Cotton, 1988: The sensitivity of a simulated extratropical mesoscale convective system to longwave radiation and ice–phase microphysics. *J. Atmos. Sci.*, **45**, 3897–3910.

Clark, T. L., P. K. Smolarkiewicz and W. D. Hall, 1988: Three-dimensional cumulus entrainment studies. *Preprints, 10th Intl. Cloud Phys. Conf.*, Bad Homburg (FRG), German Weather Service, 88–90.

Cotton, W. R., M.–S. Lin, R. L. McAnelly and C. J. Tremback, 1989: A composite model of Mesoscale Convective Complexes. *Mon. Wea. Rev.*, **117**, 765–783.

Crépon, M., M. Bouthir, B. Barnier and F. Aikman, 1989: Horizontal circulation forced by bottom water formation part I: An analytical study. *J. Phys. Oceanogr.*, **19**, 1781–1792.

Danielsen, E. F., 1968: Stratosphere-troposphere exchange based on radio activity, ozone, and potential vorticity. *J. Atmos. Sci.*, **25**, 502–518.

——–, 1982: A dehydration mechanism for the stratosphere. *Geo. Res. Let.*, **9**, 605–608.

——–, 1990: In defense of Ertel's potential vorticity and its general applicability as a meteorological tracer. *J. Atmos. Sci.*, **47**, 2013–2020.

——–, 1993: In situ evidence of rapid, vertical, irreversible transport of lower tropospheric air into the lower tropical stratosphere by convective cloud turrets and by larger–scale upwelling in tropical cyclones. *J. of Geophys. Res.*, **98**, 8665–8681.

Davis, C. A., and M. L. Weisman, 1994: Balanced dynamics of mesoscale vortices produced in simulated convective systems. *J. Atmos. Sci.*, **51**, 2005–2030.

Dugan, J. P., R. P. Mied, P. C. Mignerey and A. F. Schuetz, 1982: Compact intrathermocline eddies in the Sargasso Sea. *J. Geophys. Res.*, **87**, 385–393.

Durran, D. R., and J. B. Klemp, 1982: The effects of moisture on trapped mountain lee waves. *J. Atmos. Sci.*, **39**, 2490–2506.

Ebert, E. E., and G. J. Holland, 1992: Observations of record cold cloud-top temperatures in tropical cyclone Hilda (1990). *Mon. Wea. Rev.*, **120**, 2240–2251.

Ertel, H., 1942: Ein neuer hydrodynamischer Wirbelsatz. *Meteorol. Z.*, **59**, 271–281.

Fankhauser, J. C., 1974: The derivation of consistent fields of wind and geopotential height from mesoscale rawinsonde data. *J. Appl. Meteor.*, **13**, 637–646.

Friday, E. W., Jr., 1967: Thermal convection from maintained and instantaneous point sources of buoyancy in a rotating field. Masters thesis. University of Oklahoma, 67 pp.

———, 1969: Behavior of discrete convective elements in a rotating fluid. Ph.D. dissertation, University of Oklahoma, 134 pp.

Fritsch, J. M., and C. F. Chappell, 1980: Numerical prediction of convectively driven mesoscale pressure systems. Part II: Mesoscale model. *J. Atmos. Sci.*, **35**, 1734–1762.

———, and J. M. Brown, 1982: On the generation of convectively driven mesohighs aloft. *Mon. Wea. Rev.*, **110**, 1554–1563.

———, and R. A. Maddox, 1981a: Convectively-driven mesoscale weather systems aloft. Part I: Observations. *J. Appl. Meteor.*, **20**, 9–19.

———, and ———, 1981b: Convectively driven mesoscale weather systems aloft. Part II: Numerical simulations. *J. Appl. Meteor.*, **20**, 20–26.

Fujita, T. T., 1982: Principle of stereoscopic height computations and their application to stratospheric cirrus over severe thunderstorms. *J. Meteor. Soc. Japan*, **60**, 355–368.

Fulton, S. R., 1989: Multigrid solution of the semi–geostrophic invertibility relation. *Mon. Wea. Rev.*, **117**, 2059–2066.

———, and W. H. Schubert, 1980: Geostrophic adjustment in a stratified atmosphere. Masters thesis, Colorado State University, 97 pp.

Gascard, J.–C., 1978: Mediterranean deep water formation–baroclinic instability and oceanic eddies. *Oceanol. Acta*, **1**, 315–330.

Gill, A. E., 1981: Homogeneous intrusions in a rotating stratified fluid. *J. Fluid Mech.*, **103**, 275–295.

———, J. M. Smith, R. P. Cleaver, R. Hide and R. Jonas, 1979: The vortex created by mass transfer between layers of a rotating fluid. *Geophys. Astrophys. Fluid Dyn.*, **12**, 195–220.

Grabowski, W. W., 1989: Numerical experiments on the dynamics of the cloud-environment interface: Small cumulus in a shear-free environment. *J. Atmos. Sci.*, **46**, 3513–3541.

———, and T. L. Clark, 1991: Cloud–environment interface instability: Rising thermal calculations in two spatial dimensions. *J. Atmos. Sci.*, **48**, 527–546.

———, and ———, 1993: Cloud–environment interface instability. Part II: Extension to three spatial dimensions. *J. Atmos. Sci.*, **50**, 555–573.

Hack, J. J., and W. H. Schubert, 1986: Nonlinear response of atmospheric vortices to heating by organized cumulus convection. *J. Atmos. Sci.*, **43**, 1559–1573.

Haynes, P. H., and M. E. McIntyre, 1987: On the evolution of vorticity and potential vorticity in the presence of diabatic heating and frictional or other forces. *J. Atmos. Sci.*, **44**, 828–840.

———, and ———, 1990: On the conservation and impermeability theorems of potential vorticity. *J. Atmos. Sci.*, **47**, 2021–2031.

Hedstrom, K., and L. Armi, 1988: An experimental study of homogeneous lenses in a rotating, stratified fluid. *J. Fluid Mech.*, **191**, 535–556.

Helfrich, K. R., 1994: Thermals with background rotation and stratification. *J. Fluid Mech.*, **259**, 265–280.

Helmholtz, 1958: Über integrale der hydrodynamischen gleichungen welche den wirbelbewegungen entsprechen. *J. Reine Angew. Math.*, **55**, 25–55. [Also in *Wiss. Abh.*, **1**, 101–134 (1882).][English transl. in *Phil. Mag.*, **23**, 485–510 (1867) and in Abbe (1893, pp. 31–57).]

Heymsfield, G. M., and R. H. Blackmer, Jr., 1988: Satellite-observed characteristics of Midwest severe thunderstorm anvils. *Mon. Wea. Rev.*, **116**, 2200–2224.

Hoskins, B. J., M. E. McIntyre and A. W. Robertson, 1985: On the use and significance of isentropic potential vorticity maps. *Quart. J. Roy. Meteor.*, **111**, 877–946.

Inman, R. I., 1966: The evolution of convective motions in a rotating fluid: A numerical calculation. Ph.D. dissertation, Texas A&M University, 90 pp.

Johnson, R. H., W. A. Gallus, Jr. and M. D. Vescio, 1990: Near–tropopause vertical motion within the trailing stratiform region of a midlatitude squall line. *J. Atmos. Sci.*, **47**, 2200–2210.

Jiang, H., and D. J. Raymond, 1995: Simulation of a mature mesoscale convective system using a nonlinear balance model. *J. Atmos. Sci.*, **52**, 161–175.

Killworth, P. D., 1976: The mixing and spreading phases of MEDOC 1. *Prog. Oceanog.*, **7**, 59–90.

———, 1983: Deep convection in the world ocean. *Rev. Geophys. Space Phys.*, **21**, 1–26.

Klaassen, G. P., and T. L. Clark, 1985: Dynamics of the cloud–environment interface and entrainment in small cumuli: Two–dimensional simulations in the absence of ambient shear. *J. Atmos. Sci.*, **42**, 2621–2642.

Lalas, D. P., and F. Einaudi, 1974: On the correct use of the wet adiabatic lapse rate in stability criteria of a saturated atmosphere. *J. Appl. Meteor.*, **13**, 318–324.

Leary, C. A., 1979: Behavior of the wind field in the vicinity of a cloud cluster in the Intertropical Convergence Zone. *J. Atmos. Sci.*, **36**, 631–639.

Lilly, D. K., 1975: Severe storms and storm systems: Scientific background, methods, and critical questions. *Pure Appl. Geophys.*, **113**, 713–734.

———, 1988: Cirrus outflow dynamics. *J. Atmos. Sci.*, **45**, 1594–1605.

Lorenz, E. N., 1955: Available potential energy and the maintenance of the general circulation. *Tellus*, **2**, 157–167.

Maddox, R. A., 1980a: Mesoscale convective complexes. *Bull. Amer. Meteor. Soc.*, **61**, 1374–1387.

Maddox, R. A., 1980a: Mesoscale convective complexes. *Bull. Amer. Meteor. Soc.*, **61**, 1374–1387.

———, 1980b: An objective technique for separating macroscale and mesoscale features in meteorological data. *Mon. Wea. Rev.*, **108**, 1108–1121.

———, 1983: Large-scale meteorological conditions associated with midlatitude, mesoscale convective complexes. *Mon. Wea. Rev.*, **11**, 1475–1493.

———, D. J. Perkey, and J. M. Fritsch, 1981: Evolution of upper tropospheric features during the development of a mesoscale convective complex. *J. Atmos. Sci.*, **38**, 1664–1674.

Manley, T. O., and K. Hunkins, 1985: Mesoscale eddies of the Arctic Ocean. *J. Geophys. Res.*, **90**, 4911–4930.

McDonald, R. N., 1990: Far-field flow forced by the entrainment of a convective plane plume in a rotating stratified fluid. *J. Phys. Oceanogr.*, **20**, 1791–1798.

———, 1992: Flows caused by mass forcing in a stratified ocean. *Deep Sea Res.*, **39**, 1767–1790.

McIntyre, J. R., 1967: An experimental study of adiabatic thermals rising in a rotating field. Masters thesis. University of Oklahoma, 45 pp.

Ninomiya, K., 1971a: Dynamical analysis of outflow from tornado-producing thunderstorms as revealed by ATS III pictures. *J. Appl. Meteor.*, **10**, 275–294.

———, 1971b: Mesoscale modification of synoptic situations from thunderstorm development as revealed by ATS III and aerological data. *J. Appl. Meteor.*, **10**, 1103–1121.

Olsson, P. Q., 1994: Evolution of balanced flow in a simulated mesoscale convective complex. Ph.D. dissertation, Colorado State University, 177 pp.

Pedlosky, J., 1979: Potential vorticity. *Geophysical Fluid Dynamics*, Springer-Verlag, NY, pp. 38–41.

Poulida, O., R. R. Dickerson and A. Heymsfield, 1995: Troposphere–stratosphere exchange in a mid latitude mesoscale convective complex: Part 1, Observations, submitted to *J. Geophys. Res.*

Rasmussen, E., 1985: A case study of a polar low development over the Barents Sea. *Tellus*, **37A**, 407–418.

Raymond, D. J., 1983: Wave-CISK in mass flux form. *J. Atmos. Sci.*, **40**, 2561–2572.

——, and H. Jiang, 1990: A theory for long–lived mesoscale convective systems. *J. Atmos. Sci.*, **47**, 3067–3077.

——, 1992: Nonlinear balance and potential–vorticity thinking at large Rossby number. *Quart. J. Roy. Meteor. Soc.*, **118**, 987–1015.

Rossby, C. G. 1938: On the mutual adjustment of pressure and velocity distributions in certain simple current systems. *J. Mar. Res.*, **1**, 15-28.

———, 1940: Planetary flow patterns in the atmosphere. *Quart. J. Roy. Meteor. Soc.*, **66**, Suppl., 68–87.

Sasaki, Y., and E. W. Friday, Jr., 1967: Thermal convection from maintained and instantaneous point sources of buoyancy in a rotating field. Univ. of Oklahoma Atmos. Res. Lab., Report ARL–1515–1, 67 pp.

Saunders, P. M., 1962: Penetrative convection in stably stratified fluids. *Tellus*, **2**, 177–194.

Schlesinger, R. E., 1990: Overshooting thunderstorm cloud top dynamics as approximated by a linear Lagrangian parcel model with analytic exact solutions. *J. Atmos. Sci.*, **47**, 988–998.

Schubert, W. H., and B. T. Alworth, 1987: Evolution of potential vorticity in tropical cyclones. *Quart. J. Roy. Meteor. Soc.*, **113**, 147–162.

——, S. R. Fulton and R. F. A. Hertenstein, 1989: Balanced atmospheric response to squall lines. *J. Atmos. Sci.*, **46**, 2478–2483.

——, and J. J. Hack, 1983: Transformed Eliassen balanced vortex model. *J. Atmos. Sci.*, **40**, 1571–1583.

———, ——, P. L. S. Silva Dias and S. R. Fulton, 1980: Geostrophic adjustment in an axisymmetric vortex. *J. Atmos. Sci.*, **37**, 1464–1484.

Shapiro, M. A., L S. Fedor and T. Hampel, 1987: Research aircraft measurements of a polar low over the Norwegian Sea. *Tellus*, **39A**, 272–306.

Shea, D. J., and W. M. Gray, 1973: The hurricane's inner core region: I. Symmetric and asymmetric structure. *J. Atmos. Sci.*, **30**, 1544–1564.

Shutts, G. J., 1987: Balanced flow states resulting from penetrative, slantwise convection. *J. Atmos. Sci.*, **44**, 3363–3376.

———, 1994: The adjustment of a rotating, stratified fluid subject to localized sources of mass. *Quart. J. Roy. Meteor. Soc.*, **120**, 361–386.

———, M. Booth and J. Norbury, 1988: A geometric model of balanced, axisymmetric flows with embedded penetrative convection. *J. Atmos. Sci.*, **45**, 2609–2621.

———, and M. J. P. Cullen, 1987: Parcel stability and its relation to semi–geostrophic theory. *J. Atmos. Sci.*, **44**, 1318–1330.

———, and M. E. B. Gray, 1994: A numerical modeling study of the geostrophic adjustment process following deep convection. *Quart. J. Roy. Meteor. Soc.*, **120**, 1145–1178.

Speer, K. G., 1989: A forced baroclinic vortex around a hydrothermal plume. *Geo. Res. Let.*, **16**, 461–464.

Spinhirne, J. D., M. Z. Hansen and J. Simpson, 1983: The structure and phase of cloud tops as observed by polarization lidar. *J. Climate Appl. Meteor.*, **22**, 1319–1331.

Starr, D. O., and S. K. Cox, 1985a: Cirrus clouds. Part I: A cirrus cloud model. *J. Atmos. Sci.*, **42**, 2663–2681.

———, and ———, 1985b: Cirrus clouds. Part II: Numerical experiments on the formation and maintenance of cirrus. *J. Atmos. Sci.*, **42**, 2682–2694

Stenchikov, G., R. Dickerson, K. Pickering, W. Ellis, B. Doddridge, S. Kondragunta, O. Poulida, J. Scala and W.–K. Tao, 1995: Troposphere–stratosphere exchange in a mid latitude mesoscale convective complex: Part 2, Numerical Simulations, submitted to *J. Geophys. Res.*

Tao, W.–K., J. Simpson, C.–H. Sui, B. Ferrier, S. Lang, J. Scala, M.–D. Chou and K. Pickering, 1993: Heating, moisture and water budgets of tropical and midlatitude squall lines: Comparisons and sensitivity to longwave radiation. *J. Atmos. Sci.*, **50**, 673–690.

Thompson, W. (Lord Kelvin) 1869: On vortex motion. *Trans. R. Soc. Edinburgh*, **25**, 217–260. [Also in *Math. Phys. Pap.*, **4**, 13–66 (1910).]

——, 1879: On gravitational oscillations of rotating water. *Proc. Roy. Soc. Edinburgh*, **10**, 92–100. [Reprinted in *Philos. Mag.*, **10**, 109–116 (1880); *Math. Phys. Pap.*, **4**, 141–148 (1910).]

Thorpe, A. J., 1985: Diagnosis of balanced vortex structure using potential vorticity. *J. Atmos. Sci.*, **42**, 397–406.

——, 1986: Synoptic scale disturbances with circular symmetry. *Mon. Wea. Rev.*, **114**, 1384–1389.

Tripoli, G. J., and W. R. Cotton, 1989a: Numerical study of an observed orogenic mesoscale convective system. Part 1: Simulated genesis and comparison with observations. *Mon. Wea. Rev.*, **117**, 274–304.

——, and ——, 1989b: Numerical study of an observed orogenic mesoscale convective system. Part 2: Analysis of governing dynamics. *Mon. Wea. Rev.*, **117**, 305–328.

Vallis, G. K., 1992: Mechanisms and parameterizations of geostrophic adjustment and a variational approach to balanced flow. *J. Atmos. Sci.*, **49**, 1144–1160.

Webster, P. J., and G. L. Stephens, 1980: Tropical upper-tropospheric extended clouds: Inferences from Winter MONEX. *J. Atmos. Sci.*, **37**, 1521–1541.

Wetzel, P. J., W. R. Cotton and R. L. McAnelly, 1983: A long–lived mesoscale convective complex. Part II: Evolution and structure of the mature complex. *Mon. Wea. Rev.*, **111**, 1919–1937.

Wilkins, E. M., Y. Sasaki, E. W. Friday, Jr. and J. McCarthy, 1969: Properties of simulated thermals in a rotating fluid. *J. Geophys. Res.*, **74**, 4472–4486.

Wirth, V., 1995: Diabatic heating in an axisymmetric cut–off cyclone and related stratosphere–troposphere exchange. *Quart. J. Roy. Met. Soc.*, **121**, 127–147.

Wong, T., G. L. Stephens, P. W. Stackhouse, Jr. and F. P. J. Valero, 1993: The radiative budgets of a tropical mesoscale convective system during the EMEX–STEP–AMEX experiment: 1. Observations. *J. Geophys. Res.*, **98**, 8683–8693.

——, ——, —— and ——, 1993: The radiative budgets of a tropical mesoscale convective system during the EMEX–STEP–AMEX experiment: 2. Model Results. *J. Geophys. Res.*, **98**, 8695–8711.

Zhang, D.–L., 1992: The formation of a cooling–induced mesovortex in the trailing stratiform region of a midlatitude squall line. *Mon. Wea. Rev.*, **120**, 2763–2785.

——, and J. M. Fritsch, 1986: Numerical simulation of the meso–β scale structure and evolution of the 1977 Johnstown flood. Part I: Model description and verification. *J. Atmos. Sci.*, **43**, 1913–1943.

——, and K. Gao, 1989: Numerical simulation of intense squall line during 10–11 June 1985 PRE–STORM. Part II: Rear inflow, surface pressure perturbations and stratiform precipitation. *Mon. Wea. Rev.*, **117**, 2067–2094.